The Static and Dynamic Compaction Characteristics of Porous Silica Powder: An Experimental and Numerical Approach

By

Andrew N. Lloyd, B.S.

A Thesis submitted to the Faculty of the Graduate School,
Marquette University, in Partial Fulfillment of
the Requirements for the Degree of
Master of Science

Milwaukee, Wisconsin

December 2006

I. Preface

The goal of this thesis is to investigate the dynamic and static compaction characteristics of porous silica powder. This goal is accomplished by experimentally evaluating and comparing the static compaction characteristics, and numerically evaluating and comparing a variety of equations of state governing dynamic compaction of porous materials. The static results showed that the silica powder has an internal porosity that is unaffected by the static compaction process of making a porous silica wafer. The dynamic results show that the previously unverified KO for the relatively low shock velocity – particle velocity region and highly distended powders predicted the experimental results as well as CTH. Neither the P-α compaction model nor the Mie-Grüneisen model was able to accurately predict the dynamic compaction characteristics of porous silica powder.

II. Acknowledgements

I would like to thank first my parents for all their love, support, and encouragement throughout my life; without them this research would never have been possible. Thank you to my friends and family for always being there for me in times of need. I would like to thank my advisor Dr. Borg for always having an open door and helpful comments to keep this research moving forward. Thank you to Dr. Fournelle for helping me with the SEM photos, allowing me access to his lab, and always being available for questions and comments as well as reviewing my thesis on my committee. I would like to thank Dr. Brower for his allowing me to use his lab and for his help with the BET machine. Thank you to Dr. Nigro for helping me with my scholarship, giving me helpful words of encouragement, and for being a reviewer on my committee.

I would also like to thank Marquette University for my scholarship in the graduate program as well as my sponsors through this research such as the Missile Defense Agency, the Wisconsin Space Grant Consortium, and the Hyper Viscosity Impact Symposium. A special thanks to Donald Weirick and Tara Hughes from the Quantachrome Instruments for their kind generosity with the BET results.

III. *Table of Contents*

IV. List of Tables

V. *List of Illustrations*

1. Introduction

The purpose of this research is to understand the static and dynamic compaction characteristics of a granular porous material. This goal is accomplished by numerically evaluating and comparing a variety of equations of state governing dynamic compaction of porous materials. These numerical simulations are assessed by comparing their output to experimental and analytical results, where available. Specifically this study intends to computationally explore low particle speed – high porosity silica, implementing two specific equations of state for direct comparison. The first equation of state is based on curve fitting existing data for porous silica, while the second approximates the porous equation of state; both are to be used in a hydrocode. A hydrocode is defined as a numerical scheme for simulating 1, 2 or 3 dimensional fluid or solid dynamic experiments. An unverified hydrocode found in Wilkins[1] will be directly compared to a highly regarded hydrocode from Sandia National Laboratories using the above two equations of state. Validation of the lesser known hydrocode will require each equation of state to attempt to simulate data from experiments conducted at Cambridge University. The distinguishing characteristic of the work undertaken in this thesis is that compaction takes place as a rapid or shock process. This rapid compaction can be approximated as an irreversible adiabatic process. Since the material is initially distended, the inter-granular dynamics, such as grain-on-grain frictional heating as a result of compaction, can be a play a significant role in the overall bulk thermodynamic behavior of the material. Thus initial porosity becomes a parameter which can cause deviations from the solid material compaction dynamics. As a result, the equations of state governing a shock compacted porous material must be modified relative to the solid material equation of state and include, at a minimum, an initial porosity functionality.

1.1. Relevance

The dynamic compaction of granular porous materials is of fundamental interest within a variety of scientific disciplines, examples include geo- and astro- physics processes, energetic material dynamics, high energy density physics, etc. For example, the rapid compaction of astrophysical processes, such as impact cratering, can be significantly effected by the dynamic characteristics of shock compaction.[2,3] Understanding the compaction dynamics allows scientists to assess not only the mass and velocity of interstellar or planetary colliding bodies, but also the geological material composition of the bodies and even have implications with regards to astrobiology.

The compaction of porous energetic materials can help scientists understand how explosive powders react under various conditions. For example, porous high melting point explosives (HMX) used by the military for warhead and solid propellant applications has had its dynamic compaction characteristics widely analyzed.[4,5] Another example occurred as a tragedy on the USS Iowa in 1989, where granular material behavior and the associated internal heating resulted in the accidental detonation of explosive materials that cost the lives of 47 sailors.

There are several advantages that can be harnessed from analyzing high energy density dynamic shocks in porous media and the computational models that predict shocks through a porous material. Meyers[6] notes that, “porous materials can achieve very high internal energy states at relatively low pressures”. Figure 1 (a) shows that for nickel based Inco IN 718 powder as the theoretical density (TD) is reduced at constant pressure the energy that the shock can attain increases significantly.

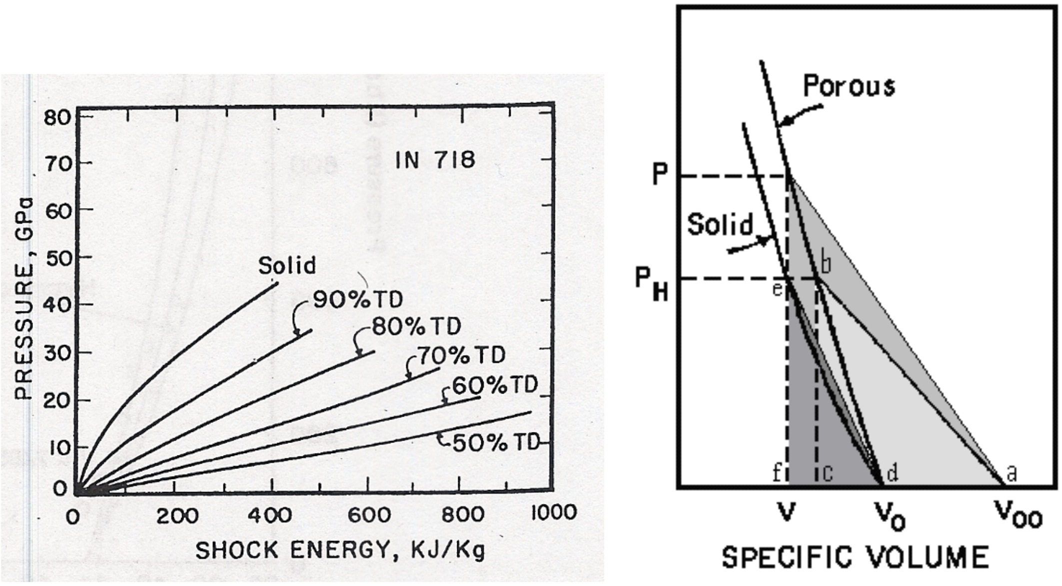

(a) (b)

Figure 1. (a) Calculated pressure-shock energy for IN 718 powder at various distensions (b) Schematic of $P - v$ diagram for a solid and porous material. [6].

This can also be seen in Figure 1 (b) where in Pressure vs. specific volume space, P- v, at a constant pressure P_H, the energy for porous compaction is the area under the triangle formed by points a, b, and c. This area is much larger than the energy for solid compaction i.e. the area under the triangle formed by points d, e, and f.

Meyers [6] also states that high amplitude shock waves in powders tend to be dampened as they pass through the material. This is due to the compaction process that must occur before the material can begin to crush; deformation after solid density is achieved. The energy required to crush a material can be illustrated by any one of the three shaded triangles in Figure 1a, for example the triangle formed by points a, b, & c. This is also the energy the shock wave loses as it passes through the material and is thus attenuated. In order to achieve the same peak pressure in a powder as a solid can produce more energy needs to be put into the system in order for the attenuation effects of the powder to be overcome. Therefore Meyers [6] states that scientists can use this knowledge to achieve “high energy states” readily.

1.2. Experimental Apparatus and Process

The material of interest for this research is Degussa Sipernat 50 µm granular amorphous silica powder. An example experimental setup is shown in Figure 2 (a). The test cell is a circular cylinder with the center axis running horizontally. A photograph of the same test cell is shown in Figure 2 (b) with the dimensions from 2 (a) applying to 2 (b).

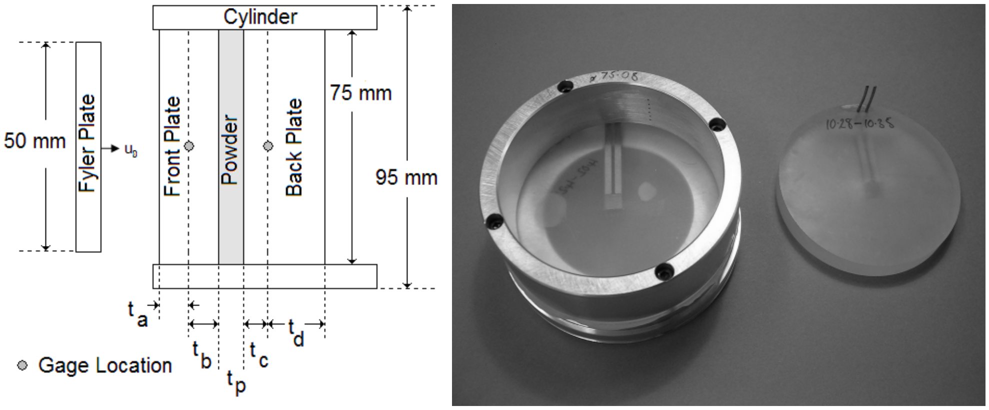

(a) (b)

Figure 2. (a) Schematic of a test cell and (b) photograph of same test cell.

Figure 2 (b) shows the front plate on the left and the target before any powder has been inserted shown on the right. The target has an aluminum annulus that holds the powder in place with the front and back plates. The “flyer plate” is moving at an initial velocity and strikes the initially stationary “front plate”. A shock then traverses the target through the front plate and backwards through the flyer plate. This initial shock signature is captured by the first strain gage. Once the shock reaches the powder, the impedance difference between the materials increases or decreases the magnitude of the shock as it continues on through the powder. The impedance difference also causes a reflected shock that is sent back into the front plate at the same lower or higher magnitude as the transmitted shock. The shock wave compacts the powder and then passes on to the back plate. The shock goes through another impedance attenuation as it enters the back plate sending a reflected wave back through the powder and a transmitted wave into the backplate. The transmitted wave reaches the back strain gage, and then continues on to the free surface. The shock is reflected back into the back plate as a "rarefaction" wave. This wave travels significantly faster than the initial wave, and if the experiment is setup properly, the reflected and rarefaction waves do not pass through the gages. Otherwise, they can attenuate the relevant data, and the experiment will give false results. Assuming the experiment is setup properly the one-dimensional longitudinal stress time histories are recorded for each gage. From the gage date, the shock velocity U_s and particle velocity u_p are determined using an impedance matching technique.

Results of experiments conducted on silica powder with various forms and densities are shown in Figure 3. The results were compiled from several sources.[7]

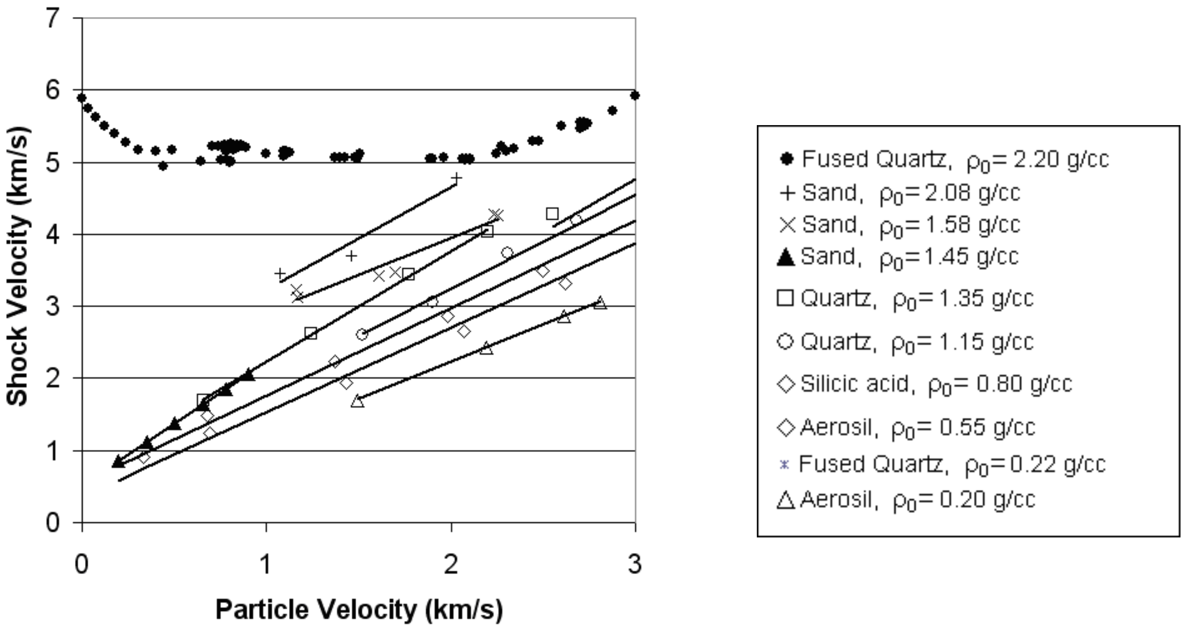

Figure 3. Collection of U_s-u_p Hugoniot data for porous silica.

The data shown in Figure 3 with particle velocities below 1 km/s were obtained from experiments conducted more recently, and the older data fit the more current data points fairly accurately. At fully consolidated density, fused quartz, changes slope to a negative direction as the particle velocity decreases below 500 km/s. This means that the shock velocity increases as the particle velocity decreases. This phenomenon is counterintuitive, and is due to the fact that at the lower impact velocities the elastic wave ‘outruns’ the plastic wave, thus the change in slope at 2 km/s is where the elastic-plastic transition occurs.

A variety of computational hydrocodes and equations of state have been developed to model the compaction of porous materials. These hydrocodes have been successful at modeling relatively low porous metals & nonmetals at particle velocities greater than 1 km/s. However, in order to understand the material characteristics of porous materials, one has to first develop the material characteristics of its solid form.

2. Literature Review

2.1. Mie-Grüneisen Equation of State

A Hugoniot is defined as the loci of states that can be achieved across a single shock traveling into a material at rest. A Hugoniot line is illustrated in Figure 4 as the curved line labeled "shock Hugoniot".

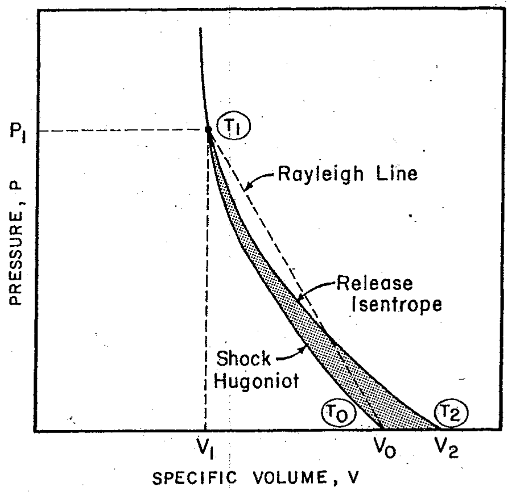

Figure 4. Shock Hugoniot, Rayleigh line, and release isentrope in $P - v$ space [1].

When a material is shock loaded, the material state, for example specific volume v, jumps from the initial state, v_0, to somewhere along the Hugoniot, state v_1 as seen in Figure 4. A shocked material follows the Raleigh line which is a straight line from state 0 to state 1 in a particular space i.e. P-v space as seen in Figure 4. The material does not follow along the Hugoniot. As the material is shocked, the temperature begins to rise from point 0 to point 1. When the material is unloaded it follows along the release isentrope to the material state 2, which has a higher specific volume than state 0 due to irreversible compression as seen in Figure 4. The work compression of the material increases the temperature so that $T_2 > T_0$. The grey area bound by the shock Hugoniot and the release isentrope shown in Figure 4 represents the irreversible work.

The Rankine-Hugoniot relations (Equations 1-3), sometimes called the “jump equations” are used to manipulate the solid Hugoniot derived from the conservation equations of mass, momentum, and energy. The derivation is given by Meyers [6].

$$\frac{v_0}{v}=\frac{U_s}{U_s-u_p} \tag{1}$$

$$P-P_0=\frac{U_s u_p}{v_0} \tag{2}$$

$$E-E_0=\frac{1}{2}\left(P+P_0\right)\left(v_0-v\right) \tag{3}$$

U_s is the shock velocity, u_p is the particle velocity, v is the specific volume, P is the pressure, and E is the energy. The subscript *0* refers to the initial state.

There are 5 assumptions involved in Equations 1-3. The first assumption, is that the there is no apparent thickness to a discontinuous shock surface. Second, there are no body forces or conduction acting at the shock surface. Third, the shear modulus of the material is *0*, and acts the material like a fluid as the shock passes through it. Fourth, there is no elastic-plastic behavior and therefore the material reacts instantaneously to a shock. Last, the material does not change its phase.

Equations 1-3 have four unknowns and therefore one additional constitutive relation is required for closure to the system. The fourth equation is an empirical relationship, also known as a Hugoniot relationship, which relates U_s, the shock speed in a material, and u_p, the particle velocity in a material. This U_s-u_p relationship is shown in Figure 3, and approximated by the polynomial in Equation 4.

$$U_s = c_0 + s_1 u_p + s_2 u_p^2 + \ldots \tag{4}$$

In Equation 4, c_0 is the sound speed at 0 pressure, and s_1 and s_2 are polynomial coefficients. Figure 5 shows the linear U_s-u_p relationship for aluminum, Polymethylmethacrylate (PMMA), and fused quartz.

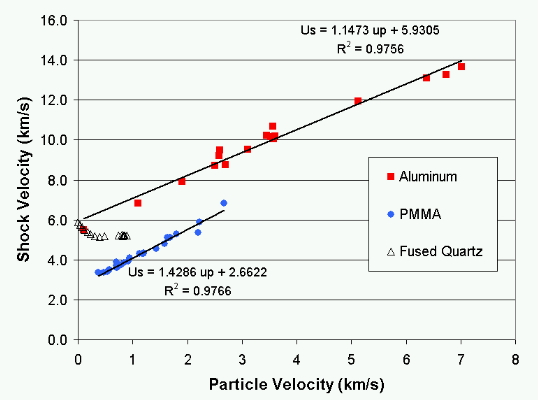

Figure 5. Collection of U_s-u_p Hugoniot data for various materials.

Equation 4 can be reduced to a linear relationship for most materials as seen in Equation 5.

$$U_s = c_0 + s_1 u_p \tag{5}$$

Although equation 5 represents an assumption as to the Us-up behavior, it can be used in conjunction with equations 1-3 to produce many other expressions relating the state variables. Any relation derived in this fashion is also called a Hugoniot. Combining equations 1-3, and 5 leads to the relation for the solid Hugoniot pressure given in Equation 6.

$$P = \frac{c_0^{\,2}\left(v_0 - v\right)}{\left[v_0 - s_1\left(v_0 - v\right)\right]^2} \tag{6}$$

The total energy E for the Mie-Grüneisen (MG) equation of state (EOS) is composed of the thermal and cold energy reference functions, i.e. the solid Hugoniot curve in Figure 1 (b). The cold compression curve at 0K is associated with the compression of the material intermolecular/atomic compression. The thermal compression curve is associated with the material intermolecular/atomic vibration. As a material's porosity changes the cold compression 0K curve does not change, since the material does not change. It is simply the cold curve for the underlying solid material. However, since the internal friction associated with the granular motion involves heating in porous materials, the thermal portion will increase. The result is seen in Figure 1 (b); the porous Hugoniot has a steeper slope, and thus lies above the solid Hugoniot.

Materials are governed at the microscopic level by statistical mechanics and at the macroscopic level by classic continuum thermodynamics. Therefore a bridge between the two worlds called the Grüneisen coefficient, Γ; see Zeldovich et al.[8] for derivation. The Grüneisen coefficient is only a function of v as seen in Equation 7.

$$\Gamma = -\left(\frac{\partial \ln v_f}{\partial \ln V}\right) \tag{7}$$

v_f is the vibrational frequency of an atom, and V is the volume. Meyers [6] suggested that Equation 8 can be used as a simplified approximation for the Grüneisen coefficient. The following expression is an approximation.

$$\Gamma_0 \cong 2s_1 - 1 \tag{8}$$

The subscript *0* refers to the zero pressure state.

The Mie-Grüneisen equation of state can be written as Equation 9 from Zeldovich et al [9].

$$P - P_H = \frac{\Gamma}{V}\left(E - E_H\right) \tag{9}$$

P_H and E_H are the Hugoniot pressure and Hugoniot internal energy reference functions from Figure 1 (b), respectively.

These above equations are only valid for a shock profile that is steady state and in a coordinate system where the material is not moving in front of the shock. This equation of state is the most common starting point for porous compaction models, because the pressure and internal energy at a point off the Hugoniot curve are directly related to the pressure and internal energy in the Hugoniot curve by Equation 9 along an isochore.

2.1.1. Anomalous Hugoniot

For most materials, the *P-v* Hugoniot is a monotonically increasing function with a negative slope, as illustrated in Figure 4. It is possible that the highly distended powders, the theoretical compacted Hugoniot has a positive slope in *P-v* space as seen in Figure 6. If this occurs, the *P-v* Hugoniot is known as an anomalous Hugoniot[9]. This behavior is counter intuitive since an anomalous Hugoniot implies that as the material volume is increased, its pressure also is increased.

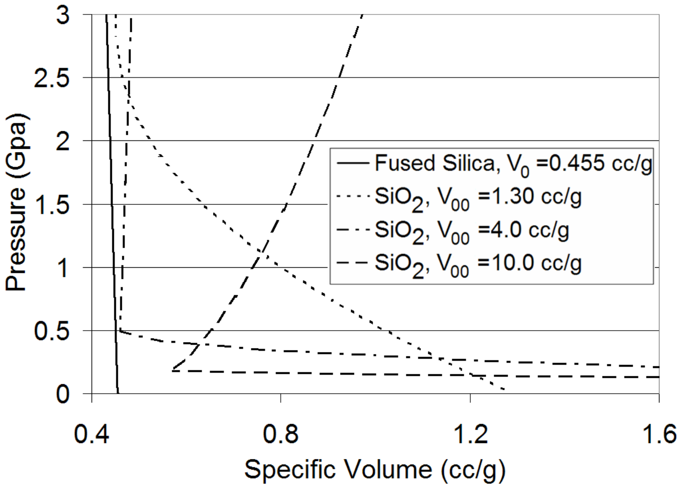

Figure. 6. *P-v* Hugoniot data for un-compacted and fully compacted porous silica

As the initial porous material density approaches the fully consolidated density its Hugoniot behavior will gradually start to resemble the solid material Hugoniot, in this case fused silica. For this thesis research the anomalous Hugoniot is not implemented into any of the models of interest. It is not clear from the experimental data obtained whether the silica of interest possesses anomalous material behavior. However there has been a novel attempt to model this phenomenon to be discussed in section 3.5 and 3.9.

2.2. Snow Plow Compaction Model

The simplest equation of state for modeling the dynamic compaction of a porous medium is the snow plow model. This model assumes a path where the pressure during compaction is 0 i.e. v_{00} to v_0, until complete compaction, i.e. $v \leq v_0$, where the pressure curve in *P-v* space follows smoothly to the solid state Hugoniot as seen in Figure 7.

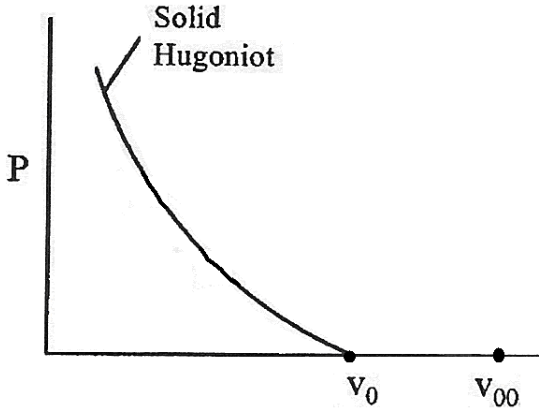

Figure. 7 Solid Hugoniot curve in *P-v* space for the snow plow model.

This model will not be used in this research, because the model isn't readily available in CTH, one of the export controlled programs of interest. However, Borg et al.[10] used this model in depth in another program and found some success modeling the silica of interest.

2.3. P-α Compaction Model

One of the earliest computational models to incorporate dynamic compaction was suggested by Herrmann[11] and was based on a simple plastic model that takes a more complex path through compaction as compared to the snow plow model. The P-α model utilizes a piecewise continuous three part Hugoniot representing the fully compacted, un-compacted, and elastic regions, respectively. A new parameter, called the porosity α, is defined as the ratio of the porous specific volume to the solid specific volume, or, $\alpha = v / v_0$. Thus α is always greater than one and when α equals one the material is fully consolidated. The porous material is initially at a specific volume, v_{00}, as indicated in Figure 8.

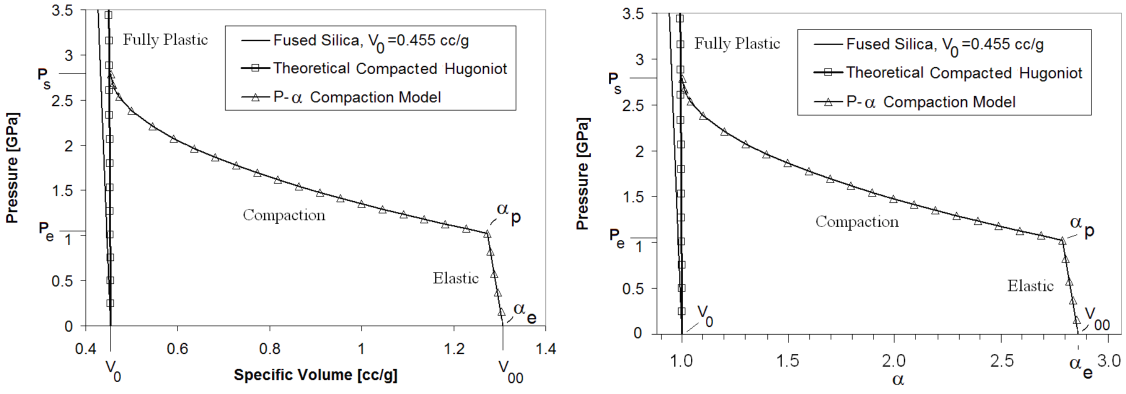

(a) (b)

Figure 8. (a) P-v and (b) P-α space illustrating P-α model

The material starts at α_e, and then elastically compacts until the maximum elastic pressure P_e is achieved at α_p, the porosity at which the material exhibits an elastic-plastic transition. The elastic region is governed by Equation 10,

$$\alpha = \frac{P(\alpha_p - \alpha_e)}{P_e} + \alpha_e \tag{10}$$

In the regime of plastic deformation i.e. the un-compacted regime, the material crushes as a parabolic function with respect to pressure as Equation 11.

$$\alpha = (\alpha_p - 1)\left[\frac{p_s - p}{p_s - p_e}\right]^2 + 1 \tag{11}$$

P_s is defined as the plastic-compaction transition to the solid Hugoniot curve. These quantities are illustrated in Figure 8. Equation 11 is a second order simplified relation found to work well with porous iron from experimental data by Butcher et al.[12] Higher order approximations for this model are available in Herrmann [10].

Once the material is fully compacted at P_s, the material smoothly follows the theoretically compacted Hugoniot to the Mie-Grüneisen equation of state for a solid given by Equation 9.

2.4. Meyers Porous Compaction Model

Substituting the reference states and the compacted internal energy Equation 3 into Equation 9 leads to the theoretical *P-v* Hugoniot for the fully compacted porous material shown in Equation 12,

$$P = \frac{\left[2v - \Gamma\left(v_0 - v\right)\right] c_0^2 \left(v_0 - v\right)}{\left[2v - \Gamma\left(v_{00} - v\right)\right]\left[v_0 - s_1\left(v_0 - v\right)\right]^2} \tag{12}$$

If the material dopes not reach complete compaction after plastically deforming, the pressure releases along an isentrope as seen in Figure 4. This equation has found success in modeling Inconel 718 powders that are greater than 60% of the initial density, as seen in Figure 8.

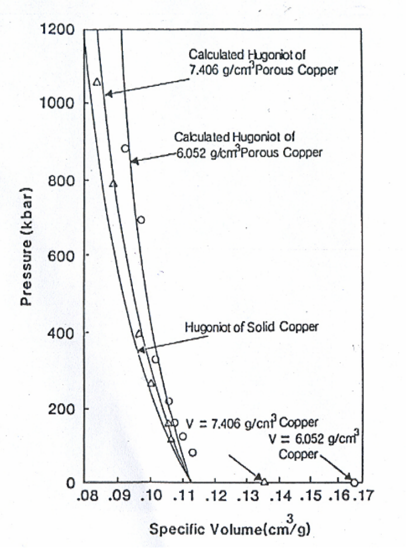

Figure 9. Measured and calculated Hugoniots for Cu with two initial densities: 6.052 and 7.406 g/cm^3 [6].

An additional thermodynamic relation will be derived here for later use in section 5.2.3 namely: particle velocity – specific volume, u_p-v. Combining Equations 1 and 2, but substituting v_0 with v_{00}, setting $P_0 = 0$, and solving for P results in Equation 13.

$$P = \frac{u_p^2}{\left(v_{00} - v\right)} \tag{13}$$

Combining Equations 12 and 13 and solving for u_p results in Equation 14.

$$u_p = \sqrt{\frac{c_0^2\left[2v - \Gamma\left(v_0 - v\right)\right]\left(v_0 - v\right)\left(v_{00} - v\right)}{\left[2v - \Gamma\left(v_{00} - v\right)\right]\left[v_0 - s_1\left(v_0 - v\right)\right]^2}} \tag{14}$$

3. Additional Porosity models

There have been many other novel attempts to model porous compaction of materials. The following sections 3.1-3.9 discuss improvements to the *P-α* model as well as additional models with limitations for each.

3.1. Dijken and De Hosson Compaction Model

Djiken and De Hosson[13] suggest, as an improvement to the *P-α* model, that any material with a porosity $\alpha < 2.5$ should have an additional error term applied according to the below formulation due to non-linearity from the U_s-u_p curve. The relation is derived from the Rankine-Hugoniot relations of Equations 1-3 using the above nomenclature and adding a fixed error term inserted into the volume as Equations 15-17:

$$U_s^p = \frac{v_{00}u_p}{v_{00}-v_0} = \frac{u_p}{1-D} \tag{15}$$

$$err = 1-\frac{D^p}{D} = 1-\frac{P^p}{P} \tag{16}$$

$$D = \frac{v_0}{v_{00}} = \frac{\Gamma(v_0)}{2+\Gamma(v_0)} \tag{17}$$

p refers to the powder. In terms of U_s-u_p space Equation 15 can be rewritten assuming that the specific volume behind the shock wave equals the solid specific volume at 0 pressure as in Equation 18.

$$U_s^p = \frac{v_{00}u_p}{v_{00}-v_0} = \frac{u_p}{1-D} \tag{18}$$

Therefore the pressure in the powder P^p can be written after combining Equations 15-18 as Equation 19 where the density initially is ρ_0.

$$P^p = \frac{U_s^p u_p}{v_{00}} = \frac{u_p^2}{v_{00} - v_0} = \frac{u_p^2 \rho_0 D}{1 - D} \tag{19}$$

The results and limitations of this model and next 4 sections 3.2-3.5 will be discussed in section 3.5.1.

3.2. Simons and Legner Compaction Model

Simons and Legner[14] propose that the success of MG equation of state is merely due to the fact that the thermal energy, E_T, and pressure, P_T, dominate cold energy, E_C, and compression P_C, at high pressures. The equation of a shock Hugoniot for a porous material in P-E space can be seen in Equation 3. The energy and pressure are the sum of the thermal, $_T$, and compressive, $_C$, parts, respectively as seen in Equation 20 and 21. Also the thermal pressure and energy have the constitutive relation in Equation 22.

$$E = E_C + E_T \tag{20}$$

$$P = P_C + P_T \tag{21}$$

$$E_T = \frac{P_T}{\rho \Gamma} \tag{22}$$

Combining Equations 3 and 20-22 gives the result of Equation 23.

$$P = \frac{\frac{2}{\Gamma} P_c - 2\rho E_c}{\frac{2}{\Gamma} + 1 - \frac{\rho}{\rho_{00}}} \tag{23}$$

The situation here is analogous to that of a shock wave in a perfect gas. The elastic terms are insignificant with respect to the inelastic terms and thus a first order model will give accurate Hugoniots at high pressures. A higher ordered elastic model for low pressures can be used in conjunction with Equation 23, while still predicting the Hugoniots accurately over all pressures. Therefore by expanding the pressure due to cold compression for volume at v_0 gives the result in Equation 24.

$$P_C = -\frac{v - v_0}{v_0 K_0} = \frac{\rho - \rho_0}{\rho_0 K_0} \tag{24}$$

K_0 is the cold compression coefficient and is related to the sound of speed in a solid by Equation 25.

$$c_0 = \frac{1}{\sqrt{\rho_0 K_0}} \tag{25}$$

The work done against P_C in compressing the material from the rest state v_0 is E_C for ρ near ρ_0 is given in Equation 26. The elastic energy is 0 at v_0.

$$E_C = \frac{\left(\rho - \rho_0\right)^2}{2K_0 \rho_0^3} \tag{26}$$

Dropping the second order terms in (ρ- ρ_0), ρ E_C is no longer dependent on P_C, which is consistent with the requirement that P_C and E_C only be accurate in the limit of low pressure. Thus substituting Equations 24 and 25 into Equation 23 the equation for the Hugoniot of a porous material is Equation 27.

$$P = -\frac{2\alpha\left(\rho-\rho_0\right)}{K_0\left(\Gamma\rho-2\alpha\rho_0-\alpha\rho_0\Gamma\right)} \tag{27}$$

3.3. Oh and Persson Compaction Model

Starting with the Rankine-Hugoniot Equations 1-3 and the linear relationship between shockwave velocity U_s and particle velocity u_p, Oh and Persson[15] derived Equation 28 as a new equation of state where $_H$ is the Hugoniot state.

$$\left(\frac{\partial E}{\partial v}\right)_P \approx -\left(\frac{\partial E}{\partial v}\right)_H \tag{28}$$

This new equation of state can be applied to predictions of solid and porous Hugoniots as seen in Figure 10.

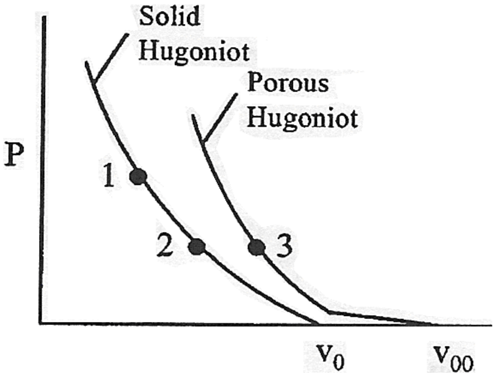

Figure 10. Solid and porous Hugoniot curves for Oh and Persson [19]

The effectiveness of Equation 28 stems from the fact that volume is the least dependent thermodynamic variable in high pressure and temperature states, and thus is assumed to be negligible. The following nomenclature will be used in this derivation according to Figure 10, and seen in Equations 29-31.

$$v_3 - v_2 \approx v_2 - v_1 \tag{29}$$

$$E_3 = E_1 \tag{30}$$

$$P_2 = P_3 \tag{31}$$

Forcing the pressure at states 2 and 3, the energy at states 1 and 3, as well as the difference in volume from state 3 to state 2 and state 2 to state 1 approximately equal, respectively from Figure 10. Then the solid Hugoniot relations from Equations 1 and 3 and the above relations in Equations 29-31 yield Equations 32-36.

$$P_1 = \frac{c_0^2 \left(v_0 - v_1\right)}{\left[v_0 - s_1 \left(v_0 - v_1\right)\right]^2} \tag{32}$$

$$P_2 = \frac{c_0^2 \left(v_0 - v_2\right)}{\left[v_0 - s_1 \left(v_0 - v_2\right)\right]^2} \tag{33}$$

$$E_1 = \frac{1}{2} P_1 \left(v_0 - v_1\right) \tag{34}$$

$$E_2 = \frac{1}{2} P_2 \left(v_0 - v_2\right) \tag{35}$$

$$E_3 = \frac{1}{2} P_3 \left(v_{00} - v_3\right) \tag{36}$$

There are nine unknowns between the eight equations (Equations 29-36), with two initial conditions (v_{00} and v_0), and two constants (bulk sound speed c_0 and slope s_1). Therefore Hugoniot relations can be explicitly solved for in terms of any combination of two thermodynamic variables between v_3, E_3, and P_3.

3.4. Wu and Jing Compaction Model

One important progression was developed by Wu and Jing[16] from a common drawback to the Oh and Persson as well as the Dijken and De Hosson compaction models; that the model was dependent upon the pressure region. The high pressure region is defined as the pressure region significant enough for complete void collapse i.e. complete compaction, and the low pressure region is defined as having incomplete compaction and requiring an isobaric path to relate the solid or reference material to its respective porous state. Figure 11 demonstrates the porous and solid Hugoniot (zero-Kelvin isotherm) curves in P-v space with isochoric and isobaric paths indicated.

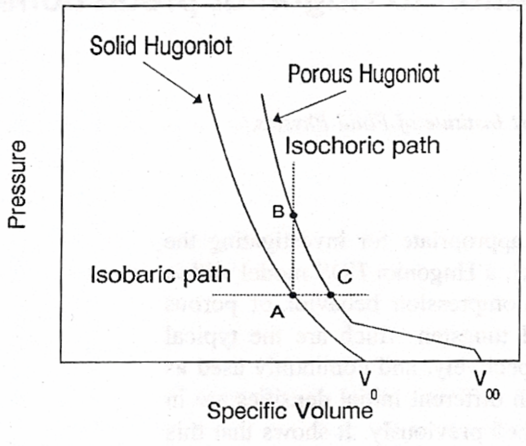

Fig 11. Solid and porous Hugoniot curves for Wu and Jing [16]

Starting with a variation of Equation 9 and applying the notation from Figure 11 gives the Equations 37 and 38: the ′ refers to the porous state and $_H$ refers to the Hugoniot state.

$$v_H - v_C = \frac{R}{P}\left(H - H_C\right) \quad \text{for the solid material} \tag{37}$$

$$v'_H - v'_C = \frac{R}{P}\left(H' - H'_C\right) \quad \text{for the porous material} \tag{38}$$

R is the effective gas constant to be defined later. Equations 39 and 40 come from the Rankine-Hugoniot relations and the definition of specific enthalpy for the porous material where $_1$ refers to the Hugoniot elastic limit (HEL) to be discussed later.

$$H'_C = Pv'_C + E'_C \tag{39}$$

$$H' = E_{00} + \frac{1}{2}P_1\left(v_{00} - v_1\right) + \frac{1}{2}P\left(v_1 + v'_H\right) \tag{40}$$

The solid material relations are derived the same way as the porous equation with the above nomenclature as Equations 41 and 42.

$$H_C = Pv_C + E_C \tag{41}$$

$$H = E_0 + \frac{1}{2}P\left(v_0 + v_H\right) \tag{42}$$

Combining Equations 37 thru 42 yields the result in Equation 43, which is the equation of state for a shocked porous material for the prediction of the full range of pressures, also shown is the solid Hugoniot in *P* vs v_H space as Equation 44.

$$P = \frac{RP_1\left(v_{00} - V'_H\right)}{v'_H\left(2 - R\right) + v_H\left(R - 2\right) + R\left(v_0 - v_1\right) + 2v_C\left(1 - R\right) + 2v'_C\left(R - 1\right)} \tag{43}$$

$$P = \frac{C_0^2\left(v_0 - v_H\right)}{\left[v_0 - s\left(v_0 - v_H\right)\right]^2} \tag{44}$$

This equation of state is only valid if the zero-Kelvin isotherms are known for the porous and solid Hugoniot states, the HEL parameters of the porous material, and the effective R value.

To determine the cold compression 0K isotherm curve a new variable α_c is introduced in Equation 45 thru 47 with use of the Carrol-Holt Model.[17]

$$\alpha_C = \frac{v'_C}{v_C} \text{ where} \tag{45}$$

$$\alpha_C \approx \begin{Bmatrix} \alpha_0 = \dfrac{\mathrm{v}_{00}}{\mathrm{v}_0} & 0 < P < P_{crit} \\ \dfrac{1}{1 - e^{-\frac{3P}{2Y}}} & P_{crit} < P < \infty \end{Bmatrix} \tag{46}$$

$$P_{crit} = \frac{2}{3} Y \ln \frac{\alpha_0}{\alpha_0 - 1} \tag{47}$$

The yield strength of the matrix material is Y and the elastic critical pressure of the porous material is P_{crit} at ambient conditions. It can be noted that the porous material is not completely compacted even after the yield strength Y has been reached as seen in the domain for α_c in Equation 46. As the pressure in the exponential increases by a factor of 2 greater than the yield strength, α_c approaches 1 i.e. compaction.

The HEL parameters P_1 and v_1, when not experimentally available, can be assumed to be for the porous material approximately equal to P_{crit} and v_{00}, respectively.

The effective R value can be obtained from the assumptions that: (1) when R is a function only of P, C_p must be a function of P and the temperature, T or remains constant, and (2) that it C_p remains constant, R is independent of T. This is shown in Equations 48 and 49.

$$R = \frac{P}{C_P}\left(\frac{\partial V}{\partial T}\right)_P \tag{48}$$

$$\left(\frac{\partial C_P}{\partial P}\right)_T = -T\left(\frac{\partial^2 C_P}{\partial T^2}\right)_P = -\frac{T}{P}\left[R\left(\frac{\partial C_P}{\partial P}\right)_P + C_P\left(\frac{\partial R}{\partial T}\right)_P\right] \tag{49}$$

From fluid mechanics the following Equations 50 and 51 are valid, where K_s, K_T, ρ, and c_0 are the isentropic bulk modulus, isothermal bulk modulus, density, and bulk sound velocity, respectively.

$$K_S = \frac{\partial C_P}{\partial C_v} K_T = \rho c_0^2 \tag{50}$$

$$\gamma = \frac{K_T}{C_v}\left(\frac{\partial V}{\partial T}\right)_P \tag{51}$$

Wu and Jing [16] also show R as a function of P and Γ, which leads to Equation 52.

$$R = \frac{P\Gamma}{K_S} = \frac{P\Gamma}{\rho c_0^2} \tag{52}$$

Γ is the Grüneisen parameter and is described using the Dugdale-MacDonald[18] formula in Equation 53 valid for most metallic materials derived from the Born-Mayer potential, which is has been found valid for use with alloys, ionic crystals, and rocks given in Equations 54 and 55.

$$\Gamma = -\frac{v_C}{2}\frac{\frac{\partial^2\left(P v_C^{\frac{2}{3}}\right)}{\partial {v_C}^2}}{\frac{\partial\left(P v_C^{\frac{2}{3}}\right)}{\partial v_C}} - \frac{1}{3} \tag{53}$$

$$P = \delta^{\frac{2}{3}} \left\{ e^{\left[a\ (1-\delta)^{-\ \frac{1}{3}} \right]} - \delta^{\frac{2}{3}} \right\} A \tag{54}$$

$$\delta = \frac{v_{0K}}{v_C} \tag{55}$$

A and *a* are two material constants formed from the solid Hugoniot, *δ* is the compressibility and v_{0K} is the specific volume of the material at the zero isotherm. Substitution of Equations 54 and 55 into 53 gives a useful expression for *Γ* as seen in Equation 56.

$$\Gamma = \frac{1}{6}\ \frac{e^{\frac{a\ (\delta^{1/3}\text{-}1)}{\delta^{1/3}}} \left(a^2 v_0^2 - 2v_0^2 \delta^{\frac{2}{3}} + 2v_C^2 \delta^{\frac{8}{3}} \right) - 4v_0^2\ \delta^{\frac{4}{3}} - 2v_C^2 \delta^{\frac{10}{3}}}{\delta^{\frac{4}{3}} \left[e^{\frac{a\ (\delta^{1/3}\text{-}1)}{\delta^{1/3}}} \left(2v_0 \delta^{\frac{1}{3}} v_C + v_0 a v_C - 2v_C^2 \delta^{\frac{4}{3}} \right) - 2v_0^2 \right]} \tag{56}$$

Finally, a more useful equation for K_s is given by Equation 57.

$$K_s = \frac{P\Gamma}{2} - \frac{dP}{dv_H} \left(v_H - \frac{\Gamma}{2} \left(v_0 - v_H \right) \right) \tag{57}$$

This effective *R* value is suitable for both the solid and porous materials; in this model the solid *R* is assumed to be equivalent to the effective *R* to predict the Hugoniot. The *dP* / dv_H term can be found from Equation 44, and thus this method requires only HEL state parameters, v_{0K}, *a*, *A*, c_0, s_1, and *Y*.

3.5. Method of Boshoff-Mostert and Viljoen

Boshoff-Mostert & Viljoen[19] simplify Wu and Jing's [16] compaction model by reducing the number of parameters required to use the model. This new model incorporates the anomalous regime to be defined in a later section, and only requires K_T, $(\partial K_T / \partial P)_T$, and v_{00} to be known. The effective R is obtained from the solid material Hugoniot and the 0K isotherm, which will be used for the porous material. Figure 12 shows the solid and porous Hugoniot curves as well as the anomalous case.

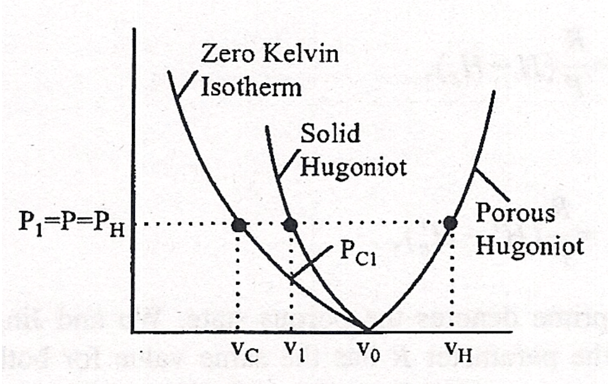

Figure 12. Porous and solid Hugoniot curves for Viljoen [18].

Setting (v_1, P_1) as a point on the solid Hugoniot from Figure 12, with Equation 37, gives rise to Equation 58.

$$v_1 - v_C = \frac{R}{P}\left(H_1 - H_C\right) \tag{58}$$

From the definition of enthalpy and Equation 3, yields Equation 59 and 60.

$$H_C = E_C + Pv_C \tag{59}$$

$$H_1 = \frac{1}{2}P_1\left(v_0 - v_1\right) \tag{60}$$

Combining Equations 58 thru 60 yields Equation 61.

$$v_1 - v_C = \frac{R}{P_1}\left(\frac{1}{2}P_1\left(v_0 - v_1\right) - E_C - P_1 v_C\right) \tag{61}$$

From Figure 12, v_1 is chosen and P_1 is determined along an isobaric path from the solid state to state 1, where the cold compression specific volume is found on the 0K isotherm. Equation 61 can now be used to calculate P_1 with the help of the Schetinin's[20] equation to describe the cold compression pressure P_{C1} found in Equation 62.

$$P_{C1} = \frac{K_{T0}}{\chi}\left[e^{\chi\left(1-\frac{v}{v_0}\right)} - 1\right] \tag{62}$$

$$K_{T0} = v\left(\frac{\partial P}{\partial v}\right)_T \tag{63}$$

$$\chi = 1 + \frac{\partial K_T}{\partial P} \tag{64}$$

K_{T0} is the isothermal bulk modulus defined in Equation 63, and χ is a dimensionless parameter defined in Equation 64, both at ambient conditions. Slater[21] develops a Grüneisen equation in terms of v similar to the Dugdale-MacDonald in Equation 53 as seen in Equation 65.

$$\gamma = -\frac{v}{2}\frac{\frac{d^2 P_C}{dv^2}}{\frac{dP_C}{dv}} - \frac{2}{3} \tag{65}$$

All that is left unknown at this point is the cold elastic energy and specific volume E_C and v_C. Along an isobaric path from (v_1, $P1$) to the 0K isotherm on Figure 12 implies that $P_1 = P_C$, and thus Equation 66 from the Mie-Grüneisen EOS can be used to calculate the cold elastic energy with Equation 62.

$$E_c = -\int_{v_0}^{v_C} P_c dv = -\frac{K_T\left(v_0\,\mathrm{e}^{\left(-\frac{\chi(-v_0+v_C)}{v_0}\right)} + \chi\left(v_c - v_0\right) - v_0\right)}{\chi^2} \tag{66}$$

Equation 62 can be written as Equation 67 as:

$$v_c = \frac{v_0}{\chi}\left[\chi - \ln\left(1 + \frac{P_c\chi}{K_{T0}}\right)\right] \tag{67}$$

Rearrangement of Equation 61 yields a value for the effective *R* as a function of only P_1 shown in Equation 68.

$$R = \frac{P_1\left(v_1 - v_c\right)}{\frac{1}{2}P_1\left(v_0 + v_1\right) - E_c - P_1 v_c} \tag{68}$$

Therefore this EOS does not rely on the parameters required for the HEL that Wu and Jing require. Instead, an isobaric path from the 0K isotherm to the porous Hugoniot i.e. $P_1 = P_c = P_H$ as seen in Figure 12, where P_H is the porous Hugoniot pressure. Equation 68 can be rewritten to take into account the porous Hugoniot as seen in Equation 69, where v_H is the porous specific volume.

$$P = -\frac{\frac{\left(v_H - v_C\right)P_H}{R} + E_C}{\frac{1}{2}v_C P_H\left(v_{00} - v_H\right)} \tag{69}$$

3.5.1. Comparison of Models 3.1 - 3.5

Figure 13 shows the results from the compaction models from subsections 3.1 – 3.5 for copper in U_s vs u_p space.

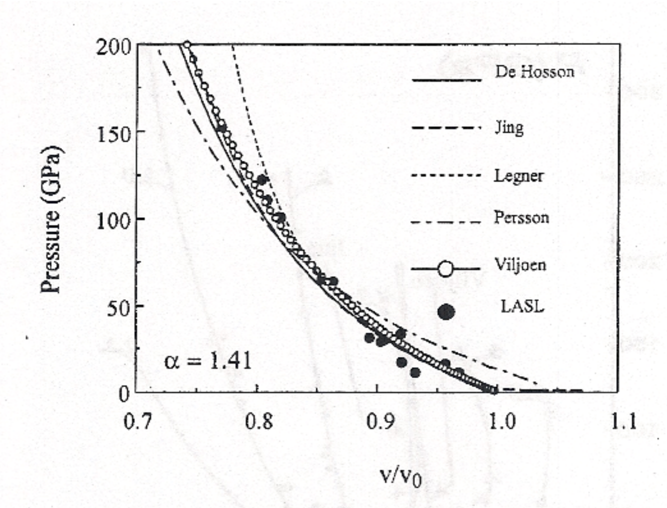

Figure 13. Copper Hugoniot curves for the normal porous case [19].

Jing and Viljoen models predict the results which are in good agreement with the Los Alamos Scientific Data (LASL)^{22} data for the normal porous Hugoniot case with $\alpha = 1.41$, where Legner and Persson over and under predict, respectively, the LASL data for $v / v_0 < 0.85$, and Persson over predicts the data over $v / v_0 = 0.88$ as seen in Figure 13.

Figure 14 shows the 5 models from sections 3.1 – 3.5 for $\alpha > 2$ i.e. the anomalous case where the final density is less than the initial density.

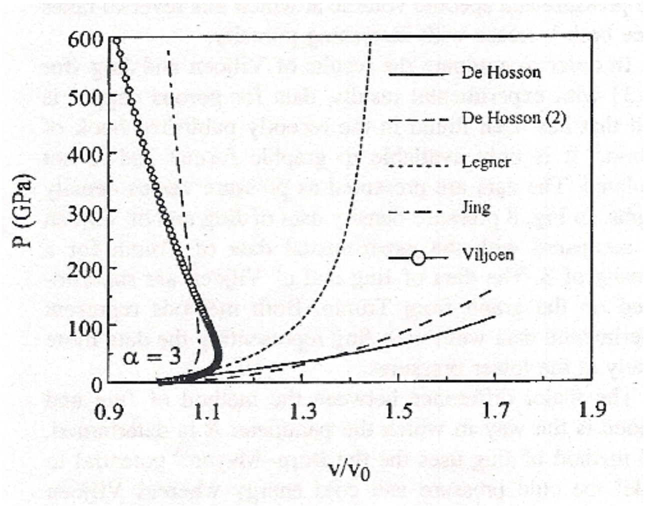

Figure 14. Copper Hugoniot curves for the anomalous case. [19]

Jing and Viljoen models are able to predict anomalous behavior without comparative experimental data, because the other models make assumptions that are violated for anomalous behavior. The slope reversal of Jing and Viljoen is a result of thermal expansion and compression alternating as dominant effects, and as porosity increases initially the magnitude of reversal increases as well.

The major difference between Jing and Viljoen is in the way that the effective *R* is determined. Viljoen uses a Shchetinin equation where Jing uses a Born-Mayer Potential. Figure 15 shows how the Jing and Viljoen models compare to experimental data taken by Trunin.

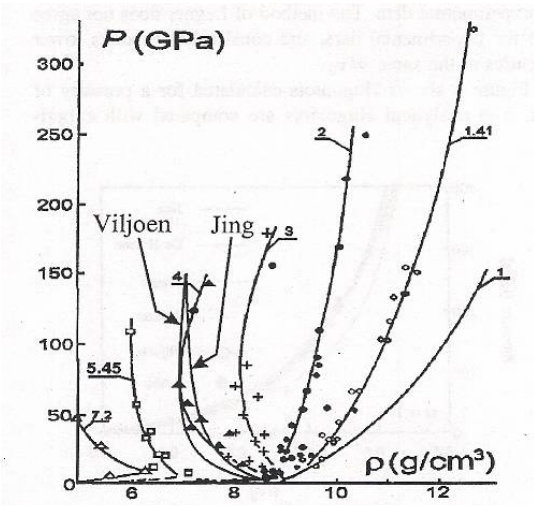

Figure 15. *P vs ρ* data for copper by Jing and Viljoen compared to experimental data of Trunin [19].

Both models reproduce the data well, but the Viljoen model predicts the data better at lower pressures for an $\alpha = 4$.

3.6. Resnyansky and Bourne Compaction Model

Resnyansky and Bourne[23] develop a porous compaction model in an attempt to explain abnormal behavior seen in experimental shock tests i.e. anomalous behavior. One explanation for this abnormal behavior can be found in trying to apply conventional shock physics with respect to porous sand. The constitutive matrix of porous sand is made up of air and sand particles. Experiments embed manganin gauges into the sand to measure the stresses that the sand sees as it is being compressed and released by shock waves. However, this signal is hard to capture because of the sand's inhomogeneous nature. Therefore an experimental setup for controlling the non-equilibrium nature of porous sand and a model to describe the process is shown by Resnyansky and Bourne. The present model is a two-phase model derived with a homogenization approach which is used in the theory of mixtures, and reduces the two systems interacting through the exchange terms to one which is suitable for hydrocode use.

A set of constitutive parameters are used to describe the mass and volume concentrations. Mass entropy is used to describe energy exchange, and special constitutive equations from specific experiments are required to close the model. The model is a two-phase matrix gas and solid, with separate mechanical properties and compressibility. The parameters are density, specific entropy, pressure, temperature, and velocity. Mass exchange is possible due to diffusion, but the phase velocities are in equilibrium.

The equation of state for the gaseous phase and the solid phase in internal energy – density space is in Equation 70 and 71, respectively.

$$e^{(1)}(\rho,s)=\frac{S_0}{\rho_{0a}(\gamma-1)}e^{\frac{s}{c_{va}}}\left(\frac{\rho}{\rho_{0a}}\right)^{\gamma-1} \tag{70}$$

$$e^{(2)}(\rho,s)=\frac{c_0^2}{2\alpha_0^2}\left[\left(\frac{\rho}{\rho_{0s}}\right)^{\alpha_0}-1\right]^2-\frac{p_0}{\rho}+c_{vs}T_0\left(\frac{\rho}{\rho_{0s}}\right)^{\beta}\left(e^{\frac{s}{c_{vs}}}-1\right)+e_{j0} \tag{71}$$

c_0, c_v, S_0, subscripts $_0$, $_a$, and $_s$ are the sound speed, specific heat, entropy, solid phase at ambient conditions, air, and solid, respectively. β, α_0, γ, are material constants determined from experiment, and e_{j0} is an energy adjustment for the phases under normal conditions. With a uniform hydrostatic assumption the strain equation can be reduced to those found in Equations 72.

$$\begin{gathered}\frac{d\ln\rho}{dt}=-\varepsilon,\quad \frac{d\alpha}{dt}=-\varphi,\quad \frac{d\theta}{dt}=-\psi\\ \frac{d\chi}{dt}=-\omega,\quad \frac{ds}{dt}=\frac{e_\alpha\varphi+e_\theta\psi+e_\chi\omega}{\rho T}\end{gathered} \tag{72}$$

The model also has a non-equilibrium variable θ which acts as a resistance equalizer, when the resistance is high in a compaction zone, $\theta < \theta_C$ (compaction concentration), and when the resistance is low in the low compaction zone $\theta_C < \theta < \theta_i$ (initial concentration).

The two-phase model described here works well for porous materials and has the added advantage of a non-convex constitutive equation of state that is easily programmable into common hydrocodes. The model has been adapted to fit non-ductile materials such as sand through critical crushing pressure assumptions. One major drawback is that independent experiments are needed for designing constitutive equations, and this model hasn't been tested on the low particle and shock velocity regime.

3.7. P-λ Compaction Model

The model suggested by Grady & Winfree[24] is called the *P-λ* model. This is a computational model for compacting heterogeneous geological materials with an emphasis on gas filled voids within the constitutive model. There are two physical states: uncompacted or fully compacted. Partially compacted is a mixture of uncompacted and fully compacted material. In the uncompacted state, the stiffer material will support the material until yielding. In the fully compacted state the components are considered to be at local pressure equilibrium and thus both yield equally as a fusion of the components. Figure 16 shows how a material transitions from uncompacted to fully compact as λ evolves over the 0 to 1 interval in P-v space. The constant strain response of the material occurs with increasing pressure, and the iso-pressure response occurs if the material never fully compacts. Unlike the P-α curve where the pore collapse is uniform throughout the material, the *P-λ* curve assumes pores will collapse within the mixture and eventually form a conglomerate of all the components heterogeneously.

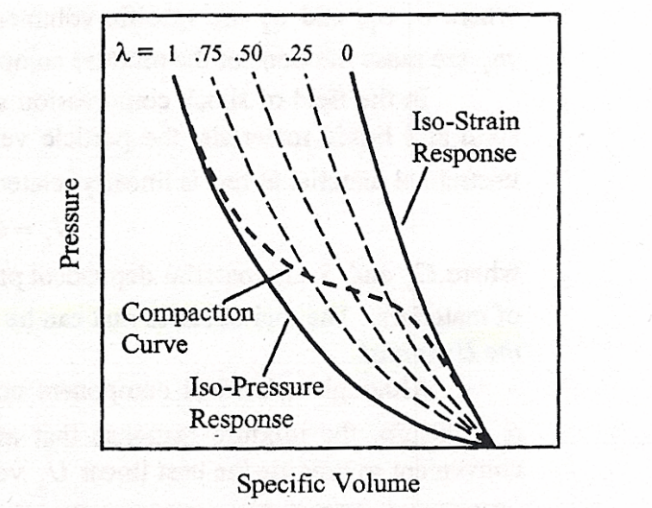

Figure 16. Pressure-volume space illustrating the *P-λ* curve [24].

In order to fully describe the compaction process the elastic properties of both the fully crushed and uncrushed materials are required. The compaction mass fraction only advances if the $P > 0$ and $P = P_{max}$. The mass fraction of crushed material is defined in Equation 73,

$$\lambda = 1 - e^{-\left(\frac{p}{p_c}\right)^n} \tag{73}$$

P_c represents the cellular strength of the material based on component materials and cellular construction as seen in Equation 74 for polyurethane foam; n represents a material constant dependent upon solid and porous densities and is determined empirically from experimental data as seen in Equation 75.

$$p_c = (15MPa)\left(1 + \frac{\rho_0}{\rho_s}\right)^{\frac{3}{2}} \tag{74}$$

$$n = \frac{1}{2} + 5.6\left(\frac{\rho_0}{\rho_s}\right) \tag{75}$$

The *0* refers to porous material, and *s* refers to the solid material. For polyurethane foam, the above equations are valid for a specific range of densities 10-50 lb/ft^3.

Figure 17 shows how the *P-λ* model predicts the mean stress compaction seen as a dotted line up to complete compaction when the density of the foam reaches its solid density. The foam is initially uncrushed until it begins to partially crush and release the air out of the voids, and then the material reaches the mean stress compaction curve where it then rides along until complete compaction.

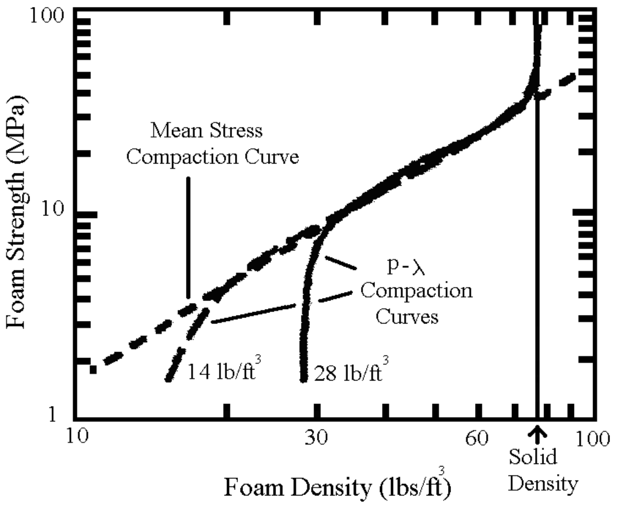

Figure. 17. Compaction curves with *P-λ* model for 14 & 28 lb/ft^3 [24].

This model has been studied at by Borg et al. [10]; however, for the purposes of this research, this model will not be used.

3.8. Wunnemann, Collins, and Melosh Compaction model

Wunnemann, et. al.[25] discuss a new EOS called the *ε-α* model, which requires only four input parameters each with physical meaning. The model can handle static testing to highly dynamic impact experiments. The model accounts for pore collapse like the *P-λ* model; however the collapse is a function of volumetric strain rather than pressure. The porous material model contains a solid and void-space component with porosity φ defined by Equation 75.

$$\phi = \frac{V - V_S}{V} = \frac{V_V}{V} \tag{76}$$

V is volume, V_S is the solid component volume, and V_V is the volume of void space. A porosity of 0 represents no void space and a porosity of 1 represents no solid component as seen in Equation 76.

$$\rho = \rho_S \left(1 - \phi\right) \tag{77}$$

ρ is the bulk density and ρ_S is the density of the solid component. For this model the term α will determine the distension of the powder as defined in Equation 77.

$$\alpha = \frac{1}{1 - \phi} = \frac{V}{V_S} = \frac{\rho_S}{\rho} \tag{78}$$

The advantage to using this scheme is that a basic equation of state can be used without any modification, but when used in a numerical scheme the forward time distension α_{t+1}

must be known in order to determine P_{t+1}. One solution is to iterate in a subroutine, but a better solution is to calculate pressure from a state variable that is known at this step i.e. volumetric strain ε_V in Equation 79.

$$\varepsilon_V = \int_{V_0}^{V'} \frac{dV}{V} = \ln\left(\frac{V'}{V_0}\right) \tag{79}$$

V' is the updated volume and V_0 is the initial volume, and compression is this case is considered to be negative in this formulation. If all the voids in the powder approach 0, then the distention and volumetric strain can be related as in Equation 80.

$$\begin{aligned} \varepsilon_V &= \ln\left(\frac{V'}{V_0}\right) = \ln\left(\frac{V'V_S}{V_S V_0}\right) = \ln\left(\frac{\alpha}{\alpha_0}\right) \\ \alpha &= \alpha_0 e^{\varepsilon_V} \end{aligned} \tag{80}$$

α_0 is the initial distension before compaction. However, compressing a porous material results in simultaneous compaction of pore space and compression of the matrix, which will be accounted for using a compaction rate parameter $\kappa \leq 1$. There are three compaction regimes to be accounted for: elastic, exponential, and power-law as seen in Figure 18.

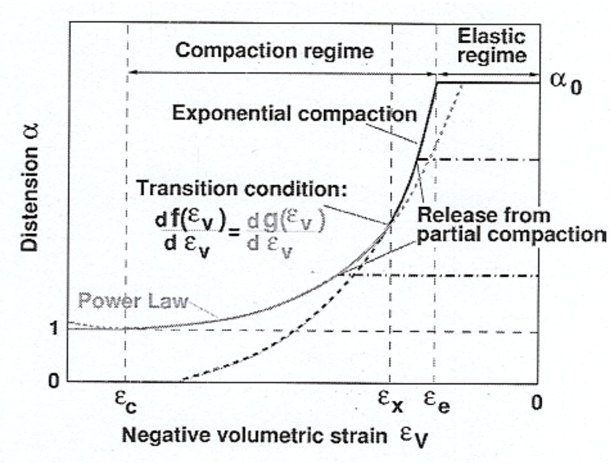

Figure 18. Schematic illustration of the ε-alpha porous compaction model showing distension α as a function of the volumetric strain εV. Three compaction regimes are shown: elastic, exponential, and power-law. [25]

The elastic regime is defined by the solid line in Figure 18, and smoothly transitions to the exponential regime in ε_V until ε_e (elastic-plastic transition) is achieved. At this point the material as begun to crush out the voids in an exponential fashion until ε_x (the threshold strain), where the material may either follow the power law or the exponential law depending on the following. Firstly, for the power law to become a reasonable assumption the slope of the compaction curve should be less steep than for the exponential compaction regime, and therefore be harder to crush out pores, secondly, the transition from one regime to the next should be smooth and continuous, and finally the compaction curve should smoothly approach the distension line α =1. The elastic regime and exponential regime are defined in Equation 81.

$$\alpha = f\left(\varepsilon_V\right) = \left\{\begin{array}{ll} \alpha_0 & \varepsilon_{\mathrm{V}} > \varepsilon_{\mathrm{e}} \\ \alpha_0 e^{\kappa\left(\varepsilon_V - \varepsilon_e\right)} & \kappa \leq 1 \\ & \varepsilon_{\mathrm{e}} > \varepsilon_{\mathrm{V}} > \varepsilon_{\mathrm{x}} \end{array}\right\} \tag{81}$$

The power law is defined in Equation 82 where ε_c is the volumetric strain at which all pore space is crushed out.

$$\alpha = g\left(\varepsilon_V\right) = \left\{\begin{array}{ll} 1 + \left(\alpha_0 e^{\kappa\left(\varepsilon_X - \varepsilon_e\right)} - 1\right)\left(\dfrac{\varepsilon_c - \varepsilon_V}{\varepsilon_c - \varepsilon_X}\right)^2 & \varepsilon_X > \varepsilon_V > \varepsilon_c \\ 1 & \varepsilon_V < \varepsilon_c \end{array}\right\} \tag{82}$$

In order for the power function regime to smoothly meet the exponential function regime the derivatives must be equal. Therefore setting $f'(\varepsilon_V) = g'(\varepsilon_V)$ gives Equation 83.

$$\varepsilon_c = 2\frac{1-\alpha_0 e^{\kappa(\varepsilon_X-\varepsilon_e)}}{\kappa\alpha_0 e^{\kappa(\varepsilon_X-\varepsilon_e)}} + \varepsilon_X \tag{83}$$

If the material never completely crushes before the plastic strain is achieved then the material relaxes back to α_0, however this usually isn't the case for large scale dynamic shock tests. In this case the irreversible compression doesn't release back to α_0, but on a horizontal line back to 0 strain as seen in Figure 18 under partial release from compaction. This model therefore has 1 initial state variable and 3 material parameters: α_0, ε_e, ε_X, and κ. However, one major drawback to this model is that these parameters have to be fitted to the data for accuracy as seen in Figure 19.

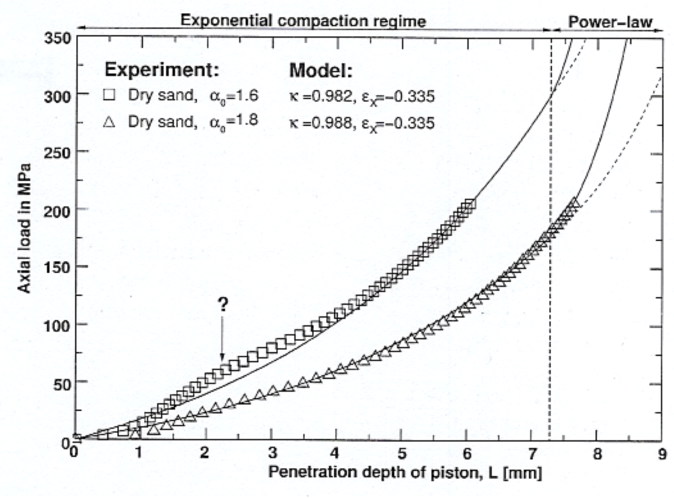

Figure 19. Axial load versus penetration depth for a static compaction test for porous silica. [25]

The vertical dashed line represents the best fit for the ε_X value, i.e. the exponential to power law transition. The dry sand appears to be well modeled using this approach except for the experimental data where the "?" occurs. This slight rise in the curve may be a result of friction with the casing during compaction, which was not considered in the model.

The model also holds up well against more dynamic experiments as seen in Figure 20. The parameters for ε_X, and κ were interpolated until the best result between the 5 data points could be reached for the porous sample. The non-porous sample fits the data extremely well and seems have a smooth curvature.

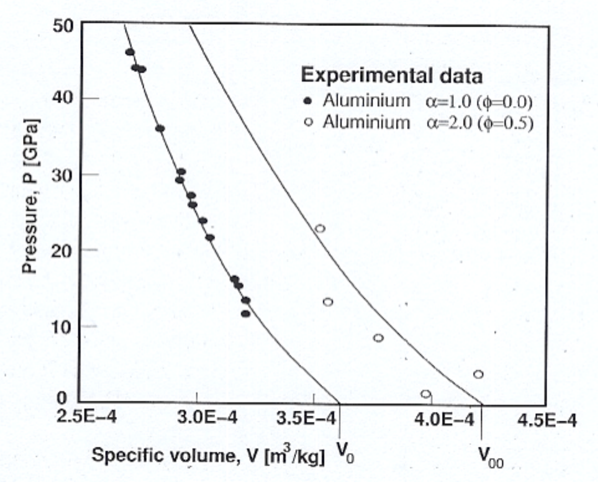

Figure 20. Calculated Hugoniot curves for porous and nonporous aluminum in comparison to experimental results [25].

This model further takes on crater growth and gravitational terms that are irrelevant to the realm of small scale porous dynamic shock impact tests. This model would be a good choice for future research into porous compaction of silica, but is not going to be used in this research.

3.9. Computational Alpha Pressure (CAP) Compaction Model

The CAP model was originally formulated by Drucker and Prager[26] for geological compaction, and has recently been adopted by Chtourou et al[27] to simulate the cold die compaction of tungsten carbide powder. There are four assumptions this model implements. Firstly, the powder is not treated microscopically as spheres or irregular shapes interacting with their surroundings but rather as a continuum that undergoes large elastic-plastic deformations. Thus the part is treated macroscopically. This is justified by the fact that the volume of the interstitial voids is much smaller than the volume of the total part. Secondly, the compaction tools are moving so slowly that the process is deemed isothermal and inviscid. The third assumption is that globally the part compacts isotropically, i.e. physical properties are independent of direction. Lastly, the compaction occurs everywhere uniformly, meaning there is no shock regime causing any jump conditions.

This model could be used as an initial starting point for the simulation of dynamic tests to see how well the static assumptions here hold in the world of dynamic events. For this research this model will not be pursued.

3.10. Summary

There are two equations of state of interest in this research: the Mie-Grüneisen and the Mie-Grüneisen with a P-α modification. The P-α has the ability to model the porous material, but ties smoothly and continuously into the Mie-Grüneisen equation of state. There have been numerous attempts to model the dynamic compaction of porous media, and these models have been shown to work well for a variety of specific materials with specific initial densities. Future work can implement these models, or form new models from the limitations of any these models presented in the previous subsections.

The dynamic experiments on porous amorphous Degussa Sipernat 50 µm silica powder will be used to verify the results of the two hydrocodes of interest to be discussed in the next section. The use of the Mie-Grüneisen and P-α equations of state along side the respective experimental data for three initial specific densities and various particle velocities will determine whether or not the unverified hydrocode found in Wilkins [1] can replicate to close agreement the highly regarded hydrocode from Sandia National Laboratories.

4. Numerical Hydrocode Schemes for KO and CTH

The two codes of interest are KO and CTH. Each code has the capability to implement the various equations of state presented in sections 2 and 3. These codes are finite volume fundamental physics codes commonly referred to as hydrocodes in that they conserve mass, momentum and energy. They can resolve multi-material, large plastic deformation processes in a ballistic strain regime. CTH, which was developed and is maintained by Sandia National Laboratory, is classified *export controlled* which means it can not be distributed to foreign nationals and some aspects of the codes inter-workings are subject to DOD review before release. CTH evolved from a one dimensional shock physics code named CHART-D (Combined Hydro and Radiation Transport Diffusion) written in the 1960s. As such CTH is now over 1 million lines of code and is difficult to modify and compile. However CTH is recognized within the shock physics community as the standard hydrocode by which all others are compared. Because of the export control classification issues and difficulties with making modifications, a new hydrocode named KO, which was written into the F77 Fortran compiler and based on the numerical scheme presented in Wilkins [1], was developed at Marquette University. Two equations of state have been programmed into KO in order to directly compare the two programs against experimental data and ultimately determine if KO performs as well as CTH. Below is a brief overview of the numerical scheme for KO and CTH.

4.1. One Dimensional LaGrangian Hydrocode [KO]

KO is a one dimensional LaGrangian hydrocode, meaning that the frame of reference is on and moving with the flow. The code follows a scheme that simultaneously solves the equations of mass, momentum, and energy (Equations 84-86) with a LaGrangian reference point.

$$\frac{D\rho}{Dt} = \overset{\text{Convection}}{-\rho\left(\nabla \bullet U\right)} \qquad \text{Conservation of Mass} \tag{84}$$

$$\rho\frac{DU}{Dt} = \overset{\text{Convection}}{-\left[\nabla \bullet \rho U U\right]} \overset{\text{Body Forces}}{-\nabla P - \left[\nabla \bullet s\right]} \overset{\text{PE}}{+\rho g} \qquad \text{Conservation of Momentum} \tag{85}$$

$$\rho\frac{DE}{Dt} = \overset{\text{KE}}{-\rho U\frac{\partial}{\partial t}U} + \overset{\text{PE}}{\rho g U} + \overset{\text{Work}}{\frac{DW}{Dt}} + \overset{\text{Thermal Diffusion}}{\frac{D\Phi}{Dt}} \qquad \text{Conservation of Energy} \tag{86}$$

U is the velocity vector, s is the stress tensor, g is gravity, W is the work, and Φ is the thermal diffusion. D / Dt is the total derivative, meaning that the time rate of change is reported as one moves *with* the substance defined as $\partial / \partial t + \nabla \bullet U$. In order to solve these equations there is a requirement of a stress-strain relationship and an equation of state to relate two thermodynamic properties together.

4.1.1. Von Neumann finite difference scheme

KO is numerically a Von Neumann[28] finite difference scheme in which, a material is divided into a LaGrangian grid that moves with the flow. The mesh is a staggered in position and in time. The space between consecutive grid lines is referred to as a zone, and this is where the thermodynamic parameters are evaluated. Position and its respective derivatives are evaluated at the grid intersections called node points. A cell is defined by two consecutive zones and the node between them as seen in Figure 21.

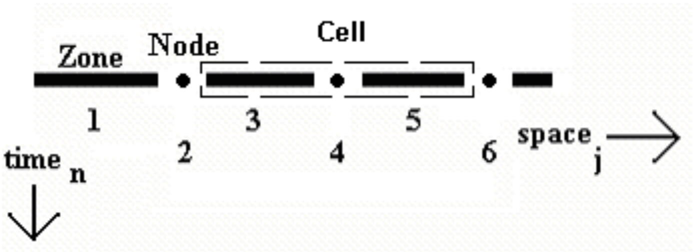

Figure 21. Discritization Schematic of Time-Space for La Grangian Node Grid

Space is denoted with a subscript *j*, and time is denoted with a superscript *n*. The zones are located at the odd whole numbers, and the nodes are located at the even whole numbers in the numerical scheme. For example, P_{j+1}^{n} would be the local pressure at the current time and at the forward zone. The mesh is closed by the boundary conditions that are applied through the use of ghost cells located at each end.

The Von Neumann finite difference equations are second order in terms of the Taylor series expansion as seen in Equations 87-89.

$$f^{n+1} = f^{n} + \frac{\Delta t}{2} f' + \frac{1}{2}\left(\frac{\Delta t}{2}\right)^{2} f'' + \frac{1}{6}\left(\frac{\Delta t}{2}\right)^{3} f''' + \ldots \tag{87}$$

$$f^{n-1} = f^{n} - \frac{\Delta t}{2} f' + \frac{1}{2}\left(\frac{\Delta t}{2}\right)^{2} f'' - \frac{1}{6}\left(\frac{\Delta t}{2}\right)^{3} f''' + \ldots \tag{88}$$

$$f^{n+1} - f^{n-1} = \Delta t f' + \text{third and fourth order terms} \tag{89}$$

4.1.2. Time centering

From Figure 21 the nodes and the zones have separate counting schemes. The zones which carry the thermodynamic properties advance in time from t^{n} to t^{n+2} with $\Delta t^{n+1} = (t^{n+2} - t^{n})$, and the nodes which carry the velocity and position advance in time from t^{n-1} to t^{n+1} with $\Delta t^{n} = (t^{n+1} - t^{n-1})$. Stability conditions determine Δt^{n+1} in advance from

$\Delta t^n = ½ (\Delta t^{n+1} - \Delta t^{n-1})$. The next section will show how to circumvent this time centering if it is disrupted or increased too much due to instability

4.1.3. *Artificial viscosity*

A finite difference scheme is inherently unstable to a certain extent due to the fact that the equations are truncated to a second order as seen in Equations 87-89. This leaves numerical round off error that can crash a program. A Von Neumann scheme therefore, utilizes an artificial viscosity term, q as derived by Wilkins et al[29] and given in Equation 90.

$$q = c_0^2 \rho L^2 \left(\frac{ds}{dt} \right)^2 + c_L^2 a \rho L \left| \frac{ds}{dt} \right| \tag{90}$$

Here ρ is the local density, ds / dt is the strain rate in the direction of acceleration, $q = 0$ when $ds / dt \geq 0$, a is the local sound speed given by $\sqrt{\frac{P}{\rho}}$ where P is the local pressure, L is a characteristic length, $C_0 \sim 2$ and $C_L \sim 1$, which determine the number of grid spacings over which the shock will spread. The artificial viscosity, q, is designed to avoid geometric convergence effects or places where the program can not distinguish where the shock is between consecutive nodes (large changes in Δt^{n+1}). This artificial viscosity is not to be confused with Newtonian fluid viscosity. The purpose of q is to numerically spread the shock front over the minimum number of grid spacings while damping the oscillations behind the shock front caused by the numerical method itself. The C_0 & C_L are listed with a value assigned for each; however for a particular application these values can be tuned for ideal damping and numerical stability.

4.1.4. Stress-Strain relationship

The objective of material models is to apply theory to practical problems with idealized simplifications to real observations. The simplest model is to assume perfectly elastic-perfectly plastic. Where the elastic regime is governed by Hooke's Law in incremental terms as seen in Equation 91

$$\sigma = \varepsilon E \tag{91}$$

Here the incremental stress equals the incremental strain multiplied by Young's Modulus. This is done so that current stress is not dependant on original material configuration. The stress in a material consists of two components: a uniform hydrostatic pressure plus a resistance to shear distortion. The elastic and plastic transition is governed by a Von Mises Yield condition.

4.1.5. Thermodynamic pressure relationship

The general form of the thermodynamic pressure relationship can be seen in Equation 92, where the pressure is the sum of the hydrostatic and thermal pressures.

$$P = A(\eta) + B(\eta)E \tag{92}$$

η is the ratio ρ / ρ_0, local density / initial solid density, $A(\eta)$ is the hydrostatic pressure component, and $B(\eta)$ is the thermal pressure component.

The pressure relationships in this research are the Mie-Grüneisen and P-α equations of state. The P-α is only needed for porous compaction. These were derived in sections 2.1 and 2.3, respectively. The finite difference numerical derivation for the Mie-Grüneisen equation of state can be found in Wilkins [1] with the algebraic form shown in Equation 93.

$$P = \rho_0 c^2 \left[x + \left(2s - \frac{\Gamma_0}{2} \right) x^2 + s\left(3s - \Gamma_0\right) x^3 \right] + \Gamma_0 \mathrm{E} = k_1 x + k_2 x^2 + k_3 x^3 + \Gamma_0 \mathrm{E} \tag{93}$$

x is a unitless number in terms of relative volume defined as $x = 1 - v / v_0$, ε and ε_0 are the specific internal energy, and initial specific internal energy, respectively, and E is the specific energy per original specific volume defined as ε / v_0. Each "*k*" parameter is defined in Equations 94-96.

$$k_1 = \rho_0 c^2 \tag{94}$$

$$k_2 = \rho_0 c^2 \left(2s - \frac{\Gamma_0}{2} \right) \tag{95}$$

$$k_3 = \rho_0 c^2 s\left(3s - \Gamma_0\right) \tag{96}$$

The *P-α* equation of state can be taken from section 2.3 for each of the three continuous Hugoniot curve regions. The pressure for elastic compaction can be obtained from Equation 10 with a smooth transition from the elastic line to the compaction curve with the following constraints can be seen in Equation 97.

$$\begin{gathered} if \quad \alpha_p < \alpha \le \alpha_e \quad then \\ P = \frac{P_e\left(\alpha - \alpha_e\right)}{\alpha_p - \alpha_e} \end{gathered} \tag{97}$$

The pressure for compaction region with the proper constraints obtained from Equation 11 is given in Equation 98.

$$\begin{aligned} &if \quad 1<\alpha\le\alpha_p \quad then \\ &P = P_s - \left(P_s - P_e\right)\sqrt{\frac{\alpha-1}{\alpha_p-1}} \end{aligned} \tag{98}$$

When α ≤ 1 the curve smoothly joins the Mie-Grüneisen curve with the governing pressure from Equation 6.

4.2. One - Three Dimensional Eulerian Hydrocode [CTH]

CTH also numerically solves the partial differential describing the conservation of mass, momentum, and energy from. These equations in an Eulerian reference frame are presented in Equations 99-101.

$$\frac{\partial\rho}{\partial t} = \overset{\text{Convection}}{-\rho\nabla\bullet U} \qquad\qquad \text{Conservation of Mass} \tag{99}$$

$$\rho\frac{\partial}{\partial t}U = \overset{\text{Body Forces}}{-\nabla\bullet\left(s+q\right)}\overset{\text{PE}}{-\nabla P} \qquad\qquad \text{Conservation of Momentum} \tag{100}$$

$$\frac{\partial\varepsilon}{\partial t} = \overset{\text{Mechanical Work}}{-\left(P+q\right)\frac{\partial}{\partial t}\left(\frac{1}{\rho}\right)} \quad \overset{\text{Viscous work}}{-\quad \frac{1}{\rho}\nabla\bullet F} \quad \overset{\text{Energy Source}}{+ \quad T} \qquad\qquad \text{Conservation of Energy} \tag{101}$$

ρ is the mass density, U is the velocity vector, s is the stress tensor, q is the artificial viscosity, P is the cell pressure, ε is the specific energy, F is the applied body force, and T is the energy source term. It solves these equations in a structured Eulerian mesh fixed in space and uses constitutive relations and equations of state to close the coupled system of equations.

4.2.1. Solution sequence

CTH uses a four step, Eulerian-LaGrangian, explicit solution scheme in order to accommodate large material deformation. The first step, referred to as the LaGrangian step, advances the momentum and energy in the mesh through a single time step assuming that the mesh moves with the materials. The second step, referred to as the re-map or Eulerian step, re-maps the distorted cell values back onto the original Eulerian mesh. The third step is the half index shifted momenta step where the thermodynamic properties are stored in an imaginary staggered mesh while the second step is finishing. The final step is the data modification step where the user can discard any material that for example may be too small for significance in a fragmentation analysis. A more detailed look into this procedure can be found in the CTH manual[30].

5. Static Compaction Experiment

In order to understand the dynamics of a material, the static properties must be addressed first. When a powder crushes in a dynamic experiment, there are shocks that traverse the powder and cause compaction and crushing. In a static compaction experiment, the powder compacts and crushes due to a monotonically increased loading under an isothermal condition. Compaction in this case is defined as removing the air that is surrounding the powder matrix. Crushing is defined as fracturing the individual grains within the matrix. Degussa Sipernat 50 µm powder will first be analyzed as uncompacted, and then compacted wafers will be made from a static compaction experiment. The question in a static compaction experiment is whether or not the grains fracture after the sample wafer is made.

5.1. Degussa Sipernat 50 µm Powder

Light microscopy and SEM were used to determine the particle size distribution of the uncrushed silica powder. Specimens were prepared by distributing some powder on a piece of double sided conductive tape attached to a glass slide and then shaking off the excess. This powder sample was then examined using an Olympus PME3 metallograph. Figure 22 (a) shows the powder at X100 under both light and scanning electron microscopy (SEM).

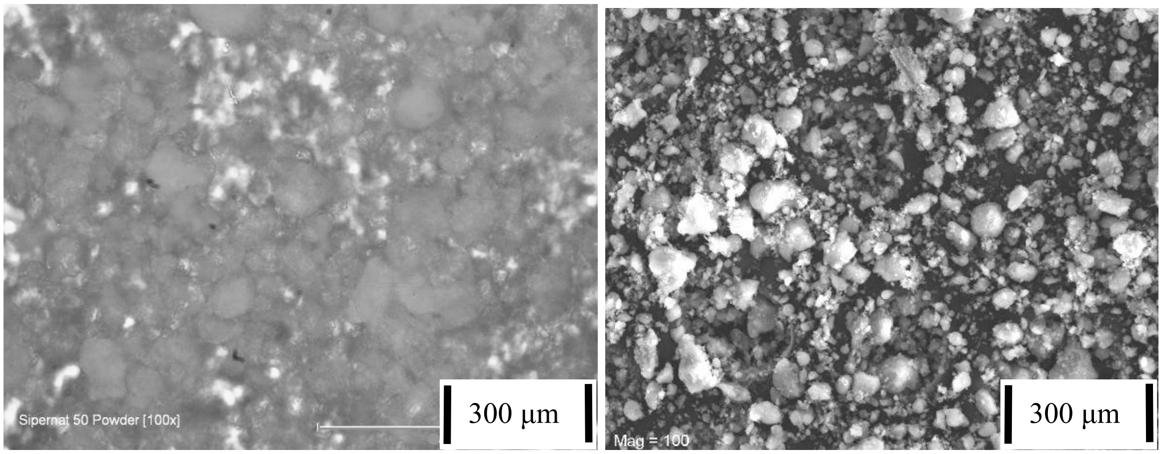

(a) (b)

Figure 22. (a) Light microscope and (b) SEM photos for the uncrushed powder at X 100.

The lightest white spots on the figure are the tape behind the powder on the glass slide and the blurry gray circles are the powder particles. The sample was then examined with a JEOL JSM35 scanning electron microscope operated at 25 kV. Figure 22 (b) is the same picture scanned with the SEM at X100. Clearly the SEM has a much higher depth of field, and shows the powder sizes to a greater clarity than the light microscope. Therefore, it was clear that SEM pictures were going to be required in order to capture all of the details of the powder. Figure 23 (a, b, c, and d) shows the SEM photos of the silica powder at various magnifications.

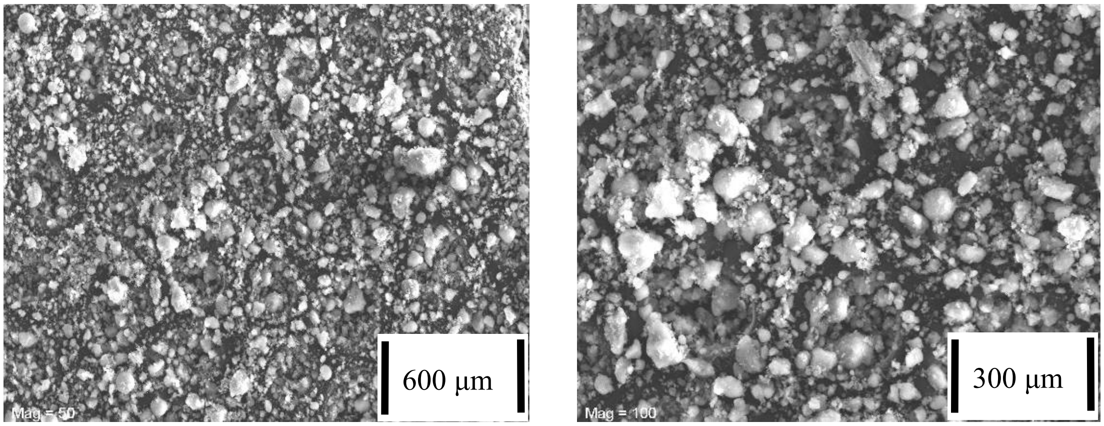

(a) (b)

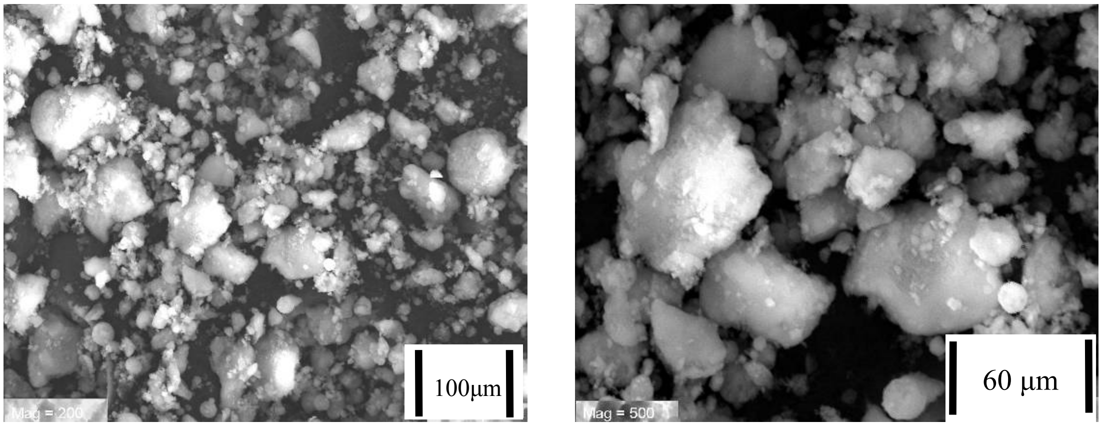

(c) (d)

Figure 23. SEM photo of uncrushed silica Powder at (a) 50 x, (b) 100 x, (c) 200 x, (d) 500 x

With respect to the individual grains, the powder grains of Figure 23 (a, b, c, and d) show the expected particle size distribution of about 4 – 150 μm for the Degussa manufacturer. Figure 23 (a) shows from a visual inspection with an incremented ruler that the average particle size is around 60 μm.

5.2. Experimental Procedure for Making Wafers

Each wafer was formed by compacting the powder in a Buehler hydraulic press, which has a maximum pressure ~ 15,500 psi, in a 1 in diameter cylinder. A schematic diagram of the cylindrical die is presented in Figure 24.

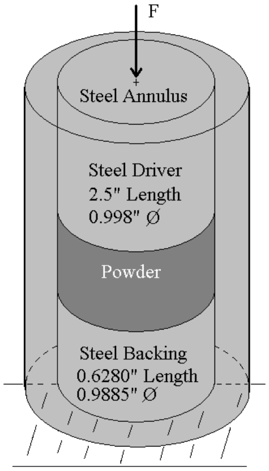

Figure 24. Schematic of cylindrical die used for static compaction

The steel cylinders (driver and backing) were polished only on the face where the powder would come into contact. First the cylinders were ground down using a LECO BG-32 Grinder with an 80 grit silicon carbide belt and then a 120 grit silicon carbide belt. Then using a Buehler Handimet Grinder with a 240 grit pad, the cylinders were hand ground turning 90° on every stroke. Each was then moved to a 320 grit pad and the process was repeated. Finally, each cylinder was polished with 1 μm Al_2O_3 and then with 0.05 μm Al_2O_3 until mirror like finish using Buehler polishing wheel.

The silica powder was weighed using a Mettler Toledo AG204 digital readout scale with 210 g maximum weight and 0.1 mg accuracy. After placing a known amount of silica into the steel annulus and assembling as shown in the schematic in Figure 24, the assembly was placed in the hydraulic press and loaded. The first sample was created by crushing the powder to the highest pressure that could be achieved, which was 11,000 psi. After removing the sample from the apparatus the height of the wafer was measured using a caliper. The density is determined using Equation 102.

$$\rho = \frac{m}{h\pi r^2} = \frac{1.55g}{0.437cm\left(1.27cm\right)^2 \pi} = 0.700\frac{g}{cm^3} \tag{102}$$

The rest of the samples were prepared by estimating the pressure which was required to compress the samples to the approximate height with respect to the first sample to achieve 0.412 g/cc and 0.375 g/cc sample wafers. The wafers were then fractured in half perpendicular to the axial axis of symmetry, and one side was sputter coated to make it conductive for scanning electron microscopy (SEM). These sputter coated surfaces are shown as the darker surface of each of Figures 25 (a, b, and c) discussed in the next section.

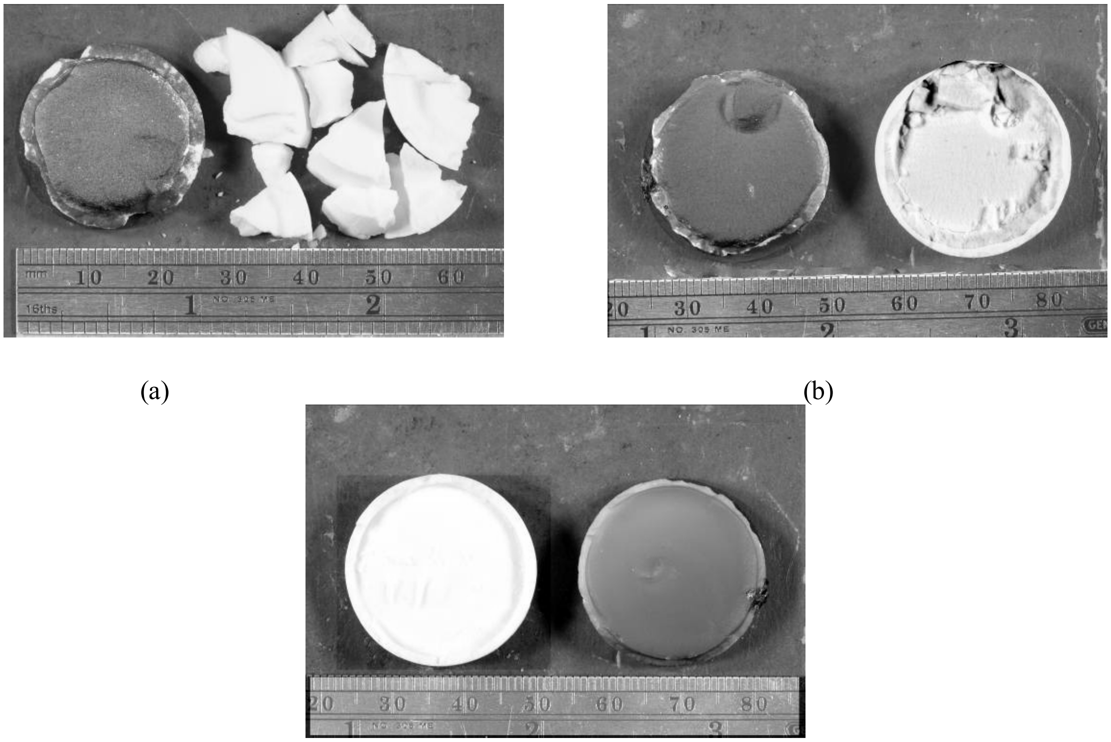

(a) (b)

(c)

Figure 25. Macroscopic views of fractured sputter coated and non-sputter coated halves of sample surfaces with top/bottom ruler reading in [mm]/[in]: (a) 0.375 g/cc (b) 0.412 g/cc (c) 0.700 g/cc

5.3. Digital Macroscopic, Light Microscopic, and SEM Photos

For SEM the fracture surfaces of the non-conductive silica wafers were sputter coated using a Technix Hummer I sputter coater operated at 80 millitor with a Au-Pd target. The samples were placed into the vacuum chamber of the coater, which was then evacuated. Once 50 millitor or less is reached, sputtering was started at 900 volts and 80 millitor. This puts about 150 µm coating of Au-Pd in two minutes. After all the samples were coated, they were placed on a carbon disc and then electrically connected to it with carbon paint and conductive double sided tape to complete the circuit. Each sample was analyzed at 50, 100, 200, and 500 x, respectively, as seen Figures 26-28.

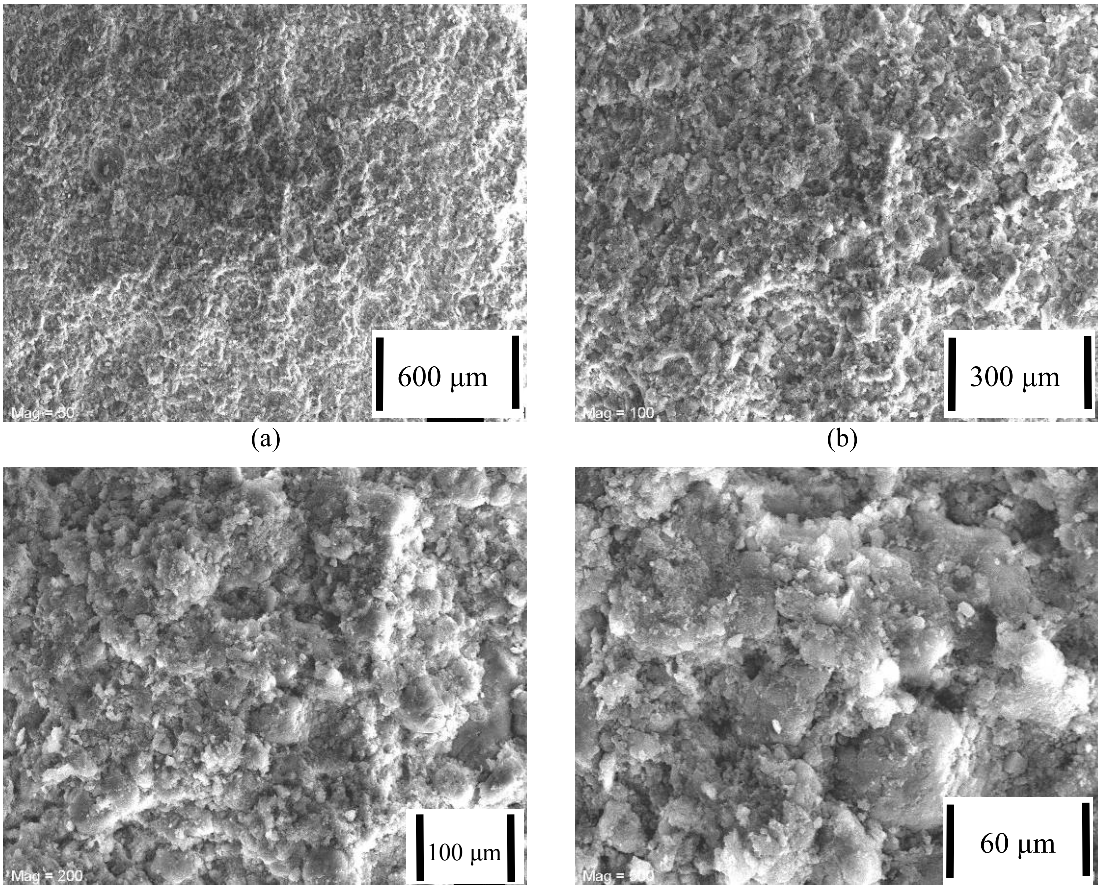

(a) (b)

(c) (d)

Figure 26. SEM photo of 0.375 g/cc wafer at (a) 50 x, (b) 100 x, (c) 200 x, (d) 500 x

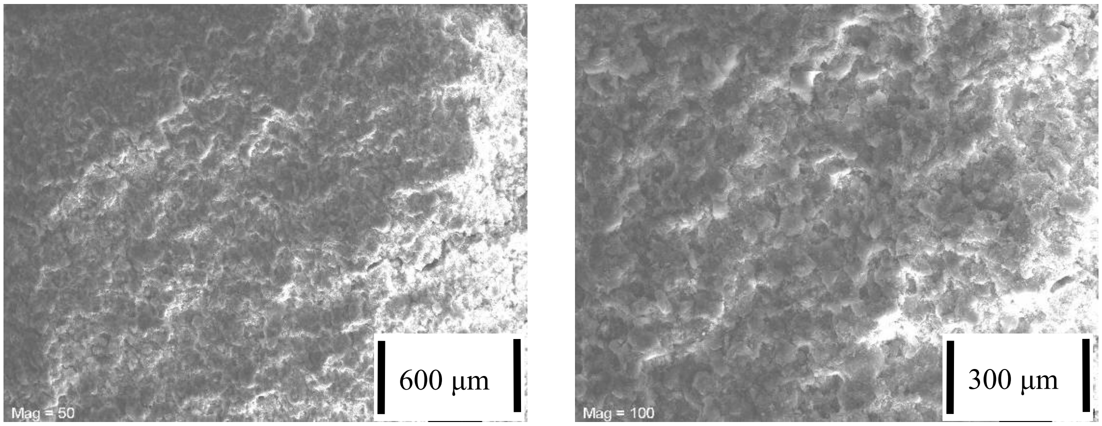

(a) (b)

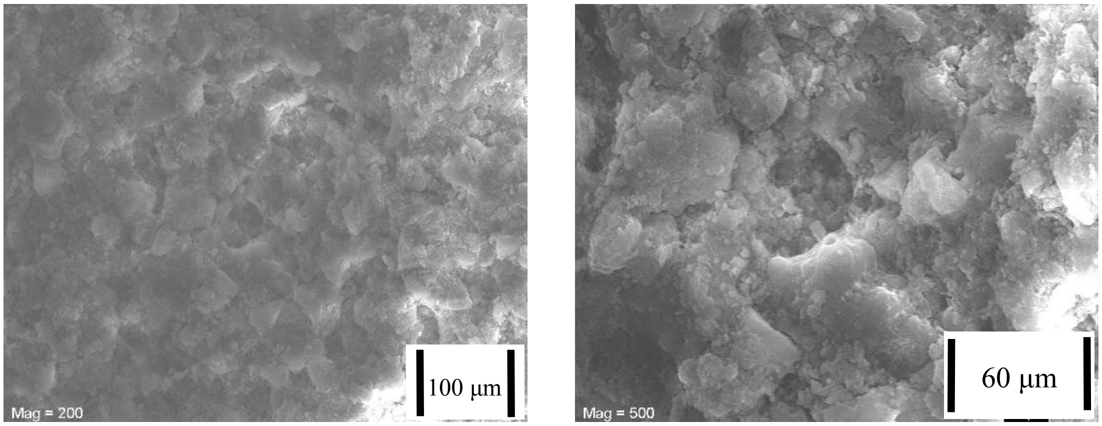

(c) (d)

Figure 27. SEM photo of 0.412 g/cc wafer at (a) 50 x, (b) 100 x, (c) 200 x, (d) 500 x

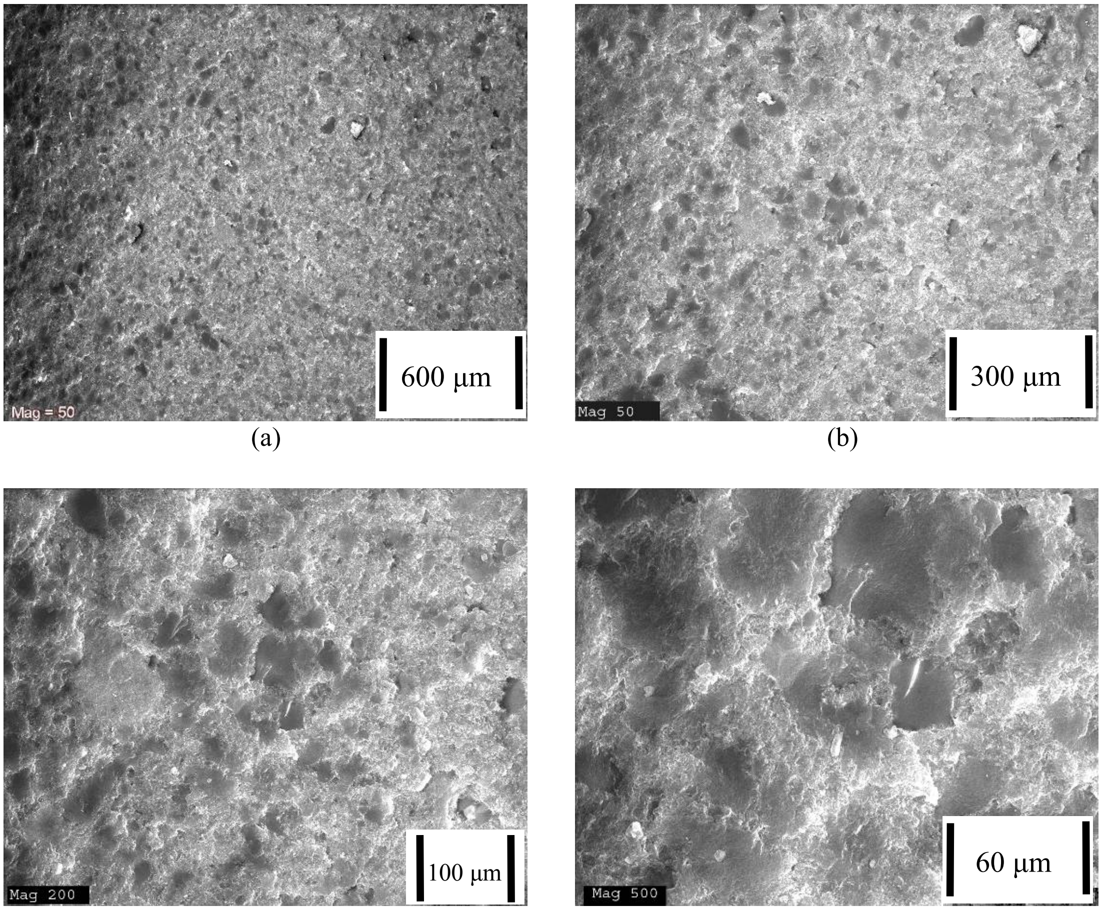

(a) (b)

(c) (d)

Figure 28. SEM photo of 0.700 g/cc wafer at (a) 50 x, (b) 100 x, (c) 200 x, (d) 500 x

Any bright spots that appear in the photos are a result of a "charging effect," locally electrons are building up due to the high electrical resistance in the localized material. These spots were avoided as much as possible. Before taking any pictures the microstructure of the sample was found by briefly scanning surface using the SEM to determine if the surface was free of the "charging effect" as much as possible. Consistency between the samples was validated by picking a low charging surface on the cross-section near the center for all the samples.

Each wafer was made from a powder sample taken from near the top of the container. Larger particles tend to settle at the top and smaller particles tend to settle at the bottom of a pile that has been handled and shaken vigorously. Without the use of a sieve, the particle size distribution can not be controlled. Therefore the SEM pictures above show a wide particle size distribution.

From Figures 26, 27, and 28 one can conclude, when comparing the wafers of different densities to each other at the same magnification, that the surfaces have about the same roughness, and that the particle sizes remained about the same. This would indicate that the samples compacted together as much as possible to relieve the air trapped between the particles. Some of the particles may have fractured by way of cleaving, especially for the 0.7 g/cc case. In that case the wafer was made with the intention of determining the maximum amount of pressure that the powder could withstand (11,000 psi on a 1" diameter cylinder). To further densify the wafer would require elevated temperatures and sintering. The particles would be limited by the constitutive matrix voids that each of the particles of various sizes could be arranged into, but by heating the particles and welding them together eventually it would become a solid. One way to determine if there is any internal porosity still remaining in between in the individual particles is to compare the surface area of the powder to the surface of the agglomerated particles within the wafer matrix. Any fusion of powder particles will lower the surface area of the agglomerated particle in the wafer matrix. This measurement can be accomplished by using a BET technique described by the procedure below.

5.4. Single Point BET Experimental Procedure and Results

BET stands for Brunauer, Emmitt, and Teller. These three scientists developed a way to calculate the surface area of a powder by “physisorption” of nitrogen to the powder surface. The assumption is that nitrogen will physisorb to the surface of the material of interest, forming a mono-layer of nitrogen which completely covers the surface area. By detecting the amount of nitrogen gained or lost to the physisorb process a measure of the material surface area can be obtained. The apparatus at Marquette University is a Quantachrome3000 BET. The following experimental procedure is for single point BET. The BET apparatus has to be calibrated to begin. A known powder sample called a “reference sample” of known surface area is weighed and put into a Pyrex u-shaped tube, which is then is properly attached to the BET apparatus. Non-reacting and reacting gases are then fed through the system at a known flow ratio. In this case, a He to N_2 gas flow ratio of 0.3 is fed through the system and outgases the sample and internal parts of the BET apparatus for a couple of days. The system reaches a steady-state when the counter, which integrates the loss or gain of nitrogen flowing in the stream to give a unitless count, on the front of the apparatus stops counting. Attenuation for the voltage on the bridge is picked in order to stay within the limit of counts that the machine can handle. A rule of thumb is about 32-64. The counter on the apparatus is reset, the adsorption button is pressed, and then voltage on the bridge is tuned to zero. Once the system is at steady-state the sample in the Pyrex tube is then submerged in liquid nitrogen. The liquid nitrogen freezes the gaseous nitrogen flowing through the tube and "adsorbs" to the entire surface of the powder. A detector, which is located down the line from the sample, constantly measures the amount of gaseous nitrogen flowing through the system. There is an integrating counter that starts counting when the difference in the voltage reaches an arbitrarily set threshold. When the counter stops counting, this number is recorded, the counter is reset, the "desorption" button is pressed, and then bridge is reset to zero. The liquid nitrogen is then removed, and the tube is submerged in room temperature water. The nitrogen gas that froze to the sample surface is then released back into the main stream and the detector beings the integration process. Once the counter stops, this number is recorded. This procedure is repeated until the attenuation is proper between the adsorption and desorption as to keep the experimental run time within the maximum counter limits and in a reasonable wall clock time of around 5-10 minutes if possible. To calibrate this sample, the counter is reset, the "desorption" button is pressed, the bridge is set to zero, and nitrogen gas is pulled form the system through a permeable setup with a gas syringe. The volume of the pulled nitrogen gas is recorded and then is fed back into the system with the syringe. The detector then integrates the known amount of nitrogen and the counter value is recorded. This procedure is repeated until the amount of gas pulled from the system gives a count close to the desorption count from the sample. Quantachrome provides software that requires the count inputs from the adsorption, desorption, and calibrant, as well as the mass of the sample and volume of the calibrant.

If the BET machine gives the desired results from the reference material, then the above procedure is repeated for the powder sample of interest. As an optional outgassing procedure, the sample can be baked at an elevated temperature for an extended period of time while being fed by the steady-state stream. This can be helpful if the sample is hydrophilic such as in this case with silica.

There are two sets of results for the same samples: one from the Marquette University and the other from samples sent to the Quantachrome Corporation. BET measurements on the Degussa 50 μm silica powder and the 3 wafers plus another wafer that was used in experiment during a dynamic test at Cambridge University labeled “0.7 EXP” can be seen in Table 1.

Table 1. BET surface area results for Quantachrome and Marquette University for the silica powder

	Specific Surface Area m^2/g						
	Quantachrome				Marquette University		Degussa
Outgassing Temp	**400 °C 3 hrs**		**25 °C 3 hrs**		**212 °C 3 hrs**	**25 °C 3 hrs**	ASTM
BET technique	*single*	*multi*	*single*	*multi*	*single*	*single*	
Powder	410	420	403	413	407	415	450
0.7 [g/cc]	417	429	392	402	431	443	-
0.7 EXP [g/cc]	439	452	428	440	456	409	-
0.412 [g/cc]	413	423	390	399	472	399	-
0.375 [g/cc]	412	424	403	412	484	445	-
Alumina Reference ** STANDARD*	-	-	265*	-	-	161	-

The Marquette University surface area measurement for the Alumina Reference was about 100 m^2/g lower than the reference standard. This was fairly consistent with the silica powder and wafers in comparison to the Degussa and Quantachrome surface area measurements. Therefore each of the Marquette University silica sample surface area measurements were averaged over three trials and then were adjusted by 100 m^2/g.

For the most part the dependency of density on the surface area of porous silica isn't widely analyzed. The results of Table 1 indicate that the surface area of the silica wafers and the uncrushed powder are unaffected by the outgassing temperature across all wafer densities. Furthermore, the surface area of the uncrushed powder is relatively the same as the surface area of the each compacted wafer. If the silica particles were welding together by atomically bonding, then the surface area would be decreasing per unit weight. Therefore, the results indicate that particles are not bonding together.

6. Dynamic Compaction Experiment

In order to computationally analyze the dynamic compaction characteristics of porous amorphous silica powder, the dynamics of the solid materials must be well understood. The objective of this chapter is to characterize the ability of hydrocodes to predict the dynamic compaction of porous powder. As a first step, experimental results are used to verify the equations of state utilized in the dynamic simulation of the materials of interest. The approach taken in this research is to first verify that both the CTH and KO hydrocodes yield accurate results for the dynamic behavior of a solid material impacting a solid material utilizing the Mie-Grüneisen equation of state for well characterized materials. Next the CTH and KO hydrocodes, utilizing the P-α porous equation of state, was used to simulate the Hugoniot state of a well characterized solid material impacting a well characterized porous material. Finally the hydrocodes were used to simulate the dynamic compaction of porous silica, which has not been well characterized, being impacted by PMMA, a well characterized solid material. By progressing toward the objective in this multi stepped approach, confidence is achieved in the computational codes and the methodology. As a starting point for solid on solid dynamics, a Cu on Cu flyer-plate experiment form Cambridge University was used to validate the Mie-Grüneisen equation of state in KO and CTH. Further validation for a solid on solid experiment, Cu on PMMA, was used to show the Mie-Grüneisen equation of state agreement with experimental data, and each was used to demonstrate material impedance mismatch and its role in experimental results.

In terms of solid on porous experiments, the first was used to re-examine Herrmann's seminal P-α paper on the dynamic compaction of a porous ductile material [11]. In this experiment Fe impacts porous Fe that is embedded in a solid Fe target, with each having the same bulk Fe properties. This section was used to demonstrate how well the P-α equation of state computationally simulates the experimental data between CTH and KO. This was accomplished by recreating the P-u_p figure from Herrmann's P-α paper using KO and CTH [11].

Finally after KO and CTH have been validated using the P-α model against a porous ductile material, each was then demonstrate how well the P-α model simulates the dynamic compaction of a porous brittle material. Published experiments from Cambridge University involving a PMMA flyer impacting a PMMA target with silica powder embedded between the PMMA plates at various initial flyer velocities was used to validate the simulations. The computational results are shown with experimental data in pressure-time traces, P-t. These figures make three comparisons to the respective experimental data. The P-α equation of state between KO and CTH, the Mie-Grüneisen equation of state between KO and CTH, and the P-α and Mie-Grüneisen equation of states against each other. Furthermore, a pressure-specific volume Hugoniot plot, P-v, for each initial compacted powder density was used to compare the experimental, analytical, and computational data.

6.1. Solid on Solid Compaction – Copper on Copper

The first comparison will implement the Mie-Grüneisen equation of state in a solid on solid copper experiment from Cambridge University with the setup shown in Figures 29 (a) and (b).

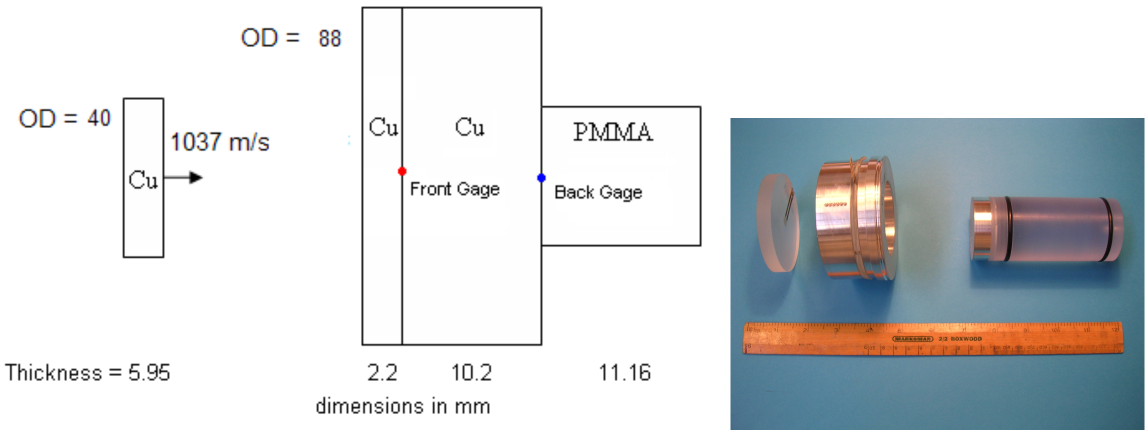

(a) (b)

Figure 29. (a) Schematic and (b) Photo of copper on copper flyer plate experimental setup from Cambridge University.

The copper flyer plate is initially moving at 1.037 km/s and strikes the copper target with the front gage sandwiched between two pieces of copper. The back gage is located between the back copper plate and the PMMA backing with all dimensions in millimeters. The gauges are held in place and the copper and PMMA are assembled with a thin layer of epoxy. Table 2 shows the Mie-Grüneisen constants used in order to simulate the experiment.

Table 2. Mie-Grüneisen constants for CTH and KO

KO and CTH input values		**PMMA**	**Cu**
Density, ρ_0	[g/cc]	1.182	8.93
Specific Density, v	[cc/g]	0.846	0.112
Slope, s		1.23	1.489
Bulk sound speed, c_0	[cm/µs]	0.273	0.394
Grüneisen parameter, Γ_0		0.85	1.99
$k_1 = \rho_0 c_0^2$	[Mbar]	8.809E-02	1.386257
$k_2 = k_1 (2s - \Gamma_0 / 2)$	[Mbar]	1.793E-01	2.748949
$k_3 = k_1 s (3s - \Gamma_0)$	[Mbar]	3.077E-01	5.112868
Poisson ratio, μ		0.3	0.343
Fracture Pressure, *Pfrac*	[Mbar]	1.00E-03	2.10E-03
Yield Strength, *Y*	[Mbar]	6.80E-05	3.33E-04
Shear Modulus, *G*	[Mbar]	2.50E-02	4.60E-01
Specific Heat, c_v	[ergs/g/eV]	1.00E+10	4.56E+10

The constants in Table 2 are written in separate input files so that each respective compiler can locate these constants and apply them accordingly. With these constants and the dimensions for the material thicknesses and gage locations from Figure 29 (a), all the information necessary to run a simulation is known for the Mie-Grüneisen equation of state. The results of this simulation can be seen in Figure 30 in pressure vs. time, *P-t*, space. The legend nomenclature indicates the hydrocode and the equation of state utilized in the numerical simulation. Thus CTH MG represents the results from the CTH hydrocode utilizing the Mie-Grüneisen equation of state.

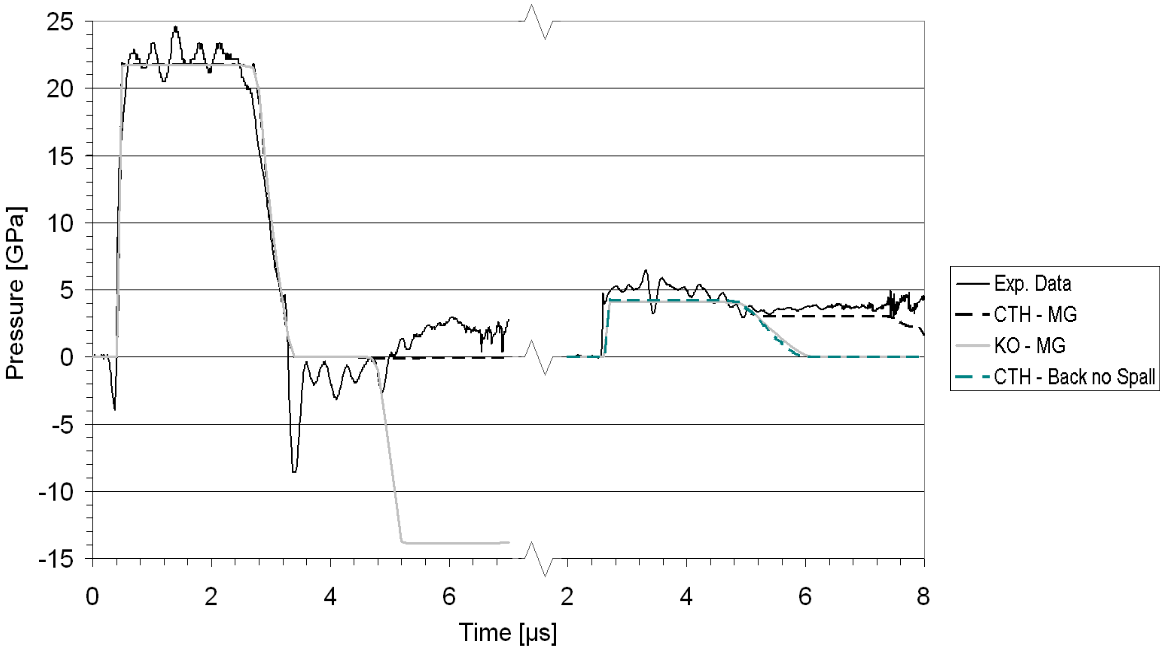

Figure 30. Cu on Cu *P-t* results for CTH and KO against experimental data.

Figure 30 shows the front gage and the back gage data simultaneously with the time frame adjusted so that the data appears in real time, i.e. the first square wave at ~0.4 μs is the front gage data, and the second wave located at ~2.5 μs is the back gage data. In a dynamic compaction experiment the flyer plate strikes the target at time zero. This initial impact launches a step wave pressure rise in both the target and flyer. When this step wave reaches the rear surface of the flyer the pressure is released back to zero. This release wave traverses back through the flyer and into the target. Thus a square wave is formed which traverses through the target. As the square wave passes by the front gauge a pressure versus time trace is recorded. The initial peak pressure and rise time for the shock traversing the front gage is about 22 GPa and 0.4 μs with fair agreement by both CTH and KO to experimental data. This square wave then passes through the remainder of the copper and is recorded by the back gauge. Due to the impedance mismatch between the copper and PMMA, PMMA having a lower impedance than copper, the peak pressure is reduced. The back gage shows a peak pressure around 5 GPa, and a rise time about 2.5 μs with fair agreement with CTH and KO. Also KO has a drop in pressure to 0 dropping gradually from 4.8 – 6 μs.

The fact that KO deviates from CTH on the back gage around 4.8 μs is not surprising, since CTH can account for spalling in a material where KO cannot. Spalling from Wilkins [1] is defined as "fracture that occurs at conditions of high hydrostatic tension without an initial crack." This can happen when two rarefaction waves, reflected waves from a free surface, hit each other and cause a local tension in the material. If this local tension exceeds the yield strength of the material, spalling will occur. This is also seen after the release wave on the front gage at 4.8 μs, where the pressure goes into tension for KO, but remains at 0 for CTH. KO has no fracture constitutive relations, and therefore the local tension can never yield to the point of fracture. However, CTH has fracture constitutive relations that can model the spalling with agreement to the experimental data for the front and back gages.

Spalling can be avoided at the gage locations in the time that is relevant to the experiment by lengthening the experimental setup. Figure 30 shows how CTH would calculate the pressure if spalling were taken out of the simulation marked as “CTH – Back no Spall.” For this case, KO and CTH predict the back gage pressure drop identically.

The experimental data shows how a signal can fluctuate when there is a high impedance mismatch between the manganin gages and the Cu. When the shock passes by two materials that have a high impendence mismatch, i.e. large differences in material properties, the shock will send out reflected waves that bounce back and forth in the thinner material and experimentally show a “ringing” effect. Since manganin is the most accepted material for strain gages as shown from Bourne and Rosenberg,[31, 32] the flyer plate and target must have approximately the same impedance as the manganin in order to avoid the “ringing” effect. One such material is PMMA, or Lucite, which is a clear plastic material much like Plexiglas. The ringing effect can be greatly reduced by equating the impedance of the embedding material with the gage material, as is seen in the next section.

6.2. Solid on Solid Compaction – Copper on PMMA

A variation of the previous experiment from Cambridge University is shown in Figure 31.

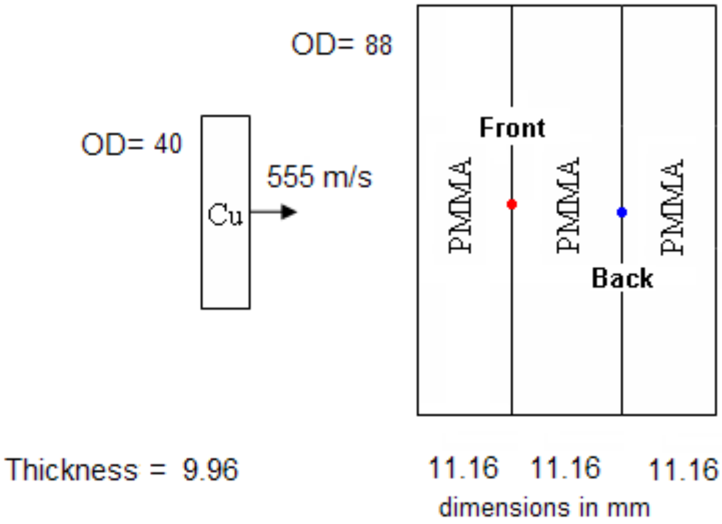

Figure 31. Copper on PMMA flyer plate experimental setup from Cambridge University.

In this experiment a Cu flyer plate impacts a PMMA target made up of 3 slabs of cylindrical PMMA with manganin gages sandwiched between them at 555 m/s. The same Mie-Grüneisen equation of state constants apply from Table 2.

The results can be seen in *P-t* space for CTH and KO against experimental data in Figure 32.

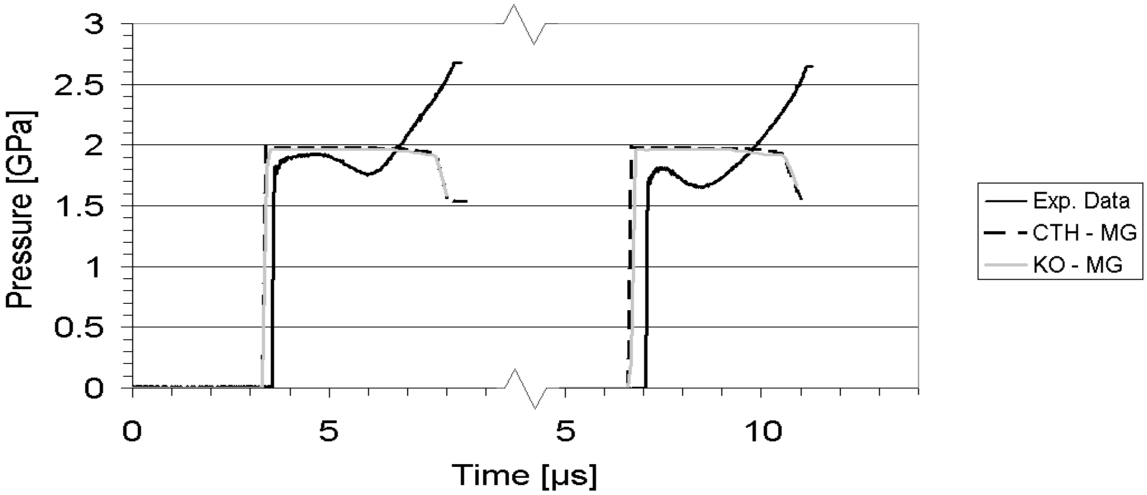

Figure 32. Cu on PMMA *P-t* results for CTH and KO against experimental data.

The peak pressure rise and rise time on the front and back gages is around 2 GPa and 3.4 μs & 2 GPa and 7 μs, respectively. CTH and KO agree with these data closely until 5 μs on the front gage, and 7 μs on the back gage. At this point the experimental data exhibits a drop in pressure followed by a rise. At this same point in CTH and KO the pressure remains constant until 8 μs on the front gage and 10 μs on the back gage, and then drops from 2 GPa to around 1.5 GPa for both the front and back gages. The back gage experimental data never reaches the peak pressure of 2 GPa, but still shows the same drop and rise phenomenon that the front gage exhibits.

The advantage of using PMMA is that the manganin gage package has about the same impedance as PMMA, and thus the ringing effect has been almost completely eliminated. The PMMA, as with many plastics, tends to flow along with the impact, thus the distinct square waves observed in the Cu impact are not evident with PMMA. Therefore the PMMA will not “flow” in the numerical scheme. A different yield strength model or constitutive relation might capture this phenomenon better. For example Menikoff[33] developed a constitutive elastic-plastic relation for PMMA, which is valid for shock pressures up to 10 GPa. For the purposes of this thesis, a better PMMA strength model will not be pursued.

Although neither of the above experiments was ideally suited as validations of the hydrocode due to either gage target impedance mismatch or plastic flow, they do allow a qualitative comparison between experiment and numerical simulation, especially between CTH and KO. The above two examples validate the approach in two ways. First, validation of the Mie-Grüneisen equation of state can be seen for Cu on Cu and Cu on PMMA, because the CTH and KO results follow relatively closely to the experimental data. Second, KO is validated by CTH because the data is identical for the Cu on PMMA and the Cu on Cu experiments. CTH, a highly evolved code, has been previously validated by Bell et al.[34].

6.3. Solid on Porous Compaction – Fe on Porous Fe

This experiment is designed to demonstrate how well the *P-α* equation of state, which has been implemented in CTH and KO, can replicate the dynamic behavior of a porous ductile metal. The experimental setup can be seen in Figure 33.

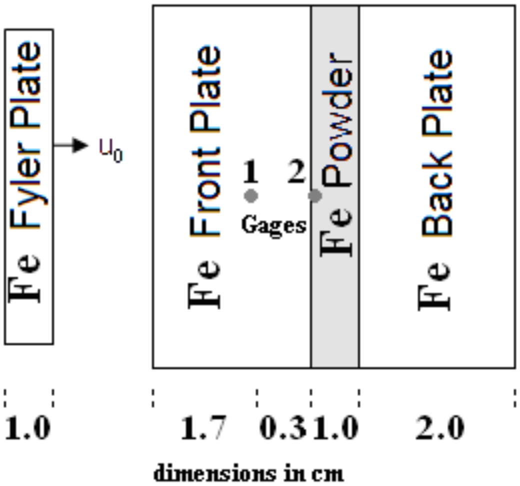

Figure 33. Experimental setup for Fe on Fe powder

The gages are located at 1.7 cm and 2.1 cm in from the front plate. This setup shown in Figure 33 is only a representative experiment, and not the real experiment. Since the purpose here is only to recreate the Hugoniot curve for Fe on Fe powder, the setup can be arbitrary as long as each plate has enough length to allow one-dimensional pressure readings without rarefaction or reflected wave interference during relevant times.

The Fe powder experiments were conducted for three initial powder densities: 3.30, 4.78, and 6.98 g/cc, or α_e = 2.37, 1.63, and 1.12. The experimental Hugoniot data was obtained from Butcher et al. [12]. The equation of state constants for CTH and KO are shown in Table 3 from Bell et al [36].

Table 3. P-α Equation state constants for Fe and Fe powder [36]

	Herrmann Data			
KO and CTH input values	**Fe**	**Porous Fe**		
Density, ρ [g/cc]	7.81	3.30	4.78	6.98
Specific Density v, [cc/g]	0.128	0.303	0.209	0.143
Porosity	0.00%	57.75%	38.80%	10.63%
Specific Heat, c_v [ergs/g/eV]	5.18e10	5.18e10	5.18e10	5.18e10
Slope, s	1.73	1.73	1.73	1.73
Bulk sound speed, c_0 [cm/μs]	0.463	0.463	0.463	0.463
Grüneisen parameter, Γ_0	1.67	1.67	1.67	1.67
k_1 [Mbar]	1.674222	7.074E-01	1.025E+00	1.496E+00
k_2 [Mbar]	4.394832	1.857E+00	2.690E+00	3.928E+00
k_3 [Mbar]	1.020E+01	4.308E+00	6.240E+00	9.112E+00
Poisson, μ	0.291	0.291	0.291	0.291
Pfrac [Mbar]	5.40E-03	5.40E-03	5.40E-03	5.40E-03
Yield, Y [Mbar]	5.00E-04	5.00E-04	5.00E-04	5.00E-04
Shear Modulus, G [Mbar]	7.75E-01	7.75E-01	7.75E-01	7.75E-01
α_p	1	2.37	1.63	1.09
α_e	1	2.37	1.63	1.12
P_e [Mbar]	0	0	0.00155	0.006
P_s [Mbar]	0	0.005	0.012	0.03
Initial elastic wave c_e [cm/μs]	-	0	0.3	0.53

Table 4 shows the pressure and particle velocity, P-u_p, data from the experiment, and Tables 5 (a) and (b) show the P-u_p data for the KO and CTH simulations, respectively.

Table 4. P-u_p Hugoniot data from Fe powder experiment [12]

6.98 cc/g		**4.78 cc/g**		**3.30 cc/g**	
$\alpha_e = 1.12$		$\alpha_e = 1.63$		$\alpha_e = 2.37$	
u_p	P	u_p	P	u_p	P
mm/μs	*kbar*	*mm/μs*	*kbar*	*mm/μs*	*kbar*
0.270	44.000	0.570	37.000	0.560	19.000
0.200	29.000	0.360	17.000	0.350	7.600
0.130	17.000	0.240	9.000	0.270	5.000
0.060	9.000	0.120	4.000	0.120	1.400
0.020	6.000	0.010	1.000	-	-

Table 5 (a). *P*-u_p data from KO for Fe – Fe powder

	6.98 g/cc		**4.78 g/cc**		**3.30 g/cc**	
	α_e = 1.1		**α_e = 1.63**		**α_e = 2.37 KO**	
Flyer velocity	u_p	*P*	u_p	*P*	u_p	*P*
mm/μs	*mm/μs*	*kbar*	*mm/μs*	*kbar*	*mm/μs*	*kbar*
10	0.08	8.9	0.09	4.1	-	-
20	0.15	18.7	0.18	6.5	0.19	2.6
30	0.22	30	0.27	10	0.29	4.4
35	0.24	42.5	-	-	-	-
40	-	-	0.36	15.7	0.38	9.3
50	-	-	0.44	24	0.43	9.9
60	-	-	0.51	30	0.55	20

Table 5 (b). *P*-u_p data from CTH for Fe – Fe powder

	6.98 g/cc		**4.78 g/cc**		**3.30 g/cc**	
	α_e = 1.12		**αe = 1.63**		**α_e = 2.37**	
Flyer velocity	u_p	*P*	u_p	*P*	u_p	*P*
mm/μs	*mm/μs*	*kbar*	*mm/μs*	*kbar*	*mm/μs*	*kbar*
10	0.09	11.1	0.08	4.3	-	-
20	0.15	20	0.17	7.1	0.13	1.9
30	0.22	30.5	0.27	9.7	0.23	3.3
35	-	-	-	-	-	-
40	0.28	45	0.35	15.4	0.37	7.7
50	-	-	0.43	23.3	0.45	12
60	-	-	0.57	32.2	0.55	17.2

Figure 34 is a series of *P*-u_p plots resulting from the setup from Figure 33 at given initial flyer velocities of Tables 5 (a) and (b) and also compares experimental, computational, and analytical data simultaneously.

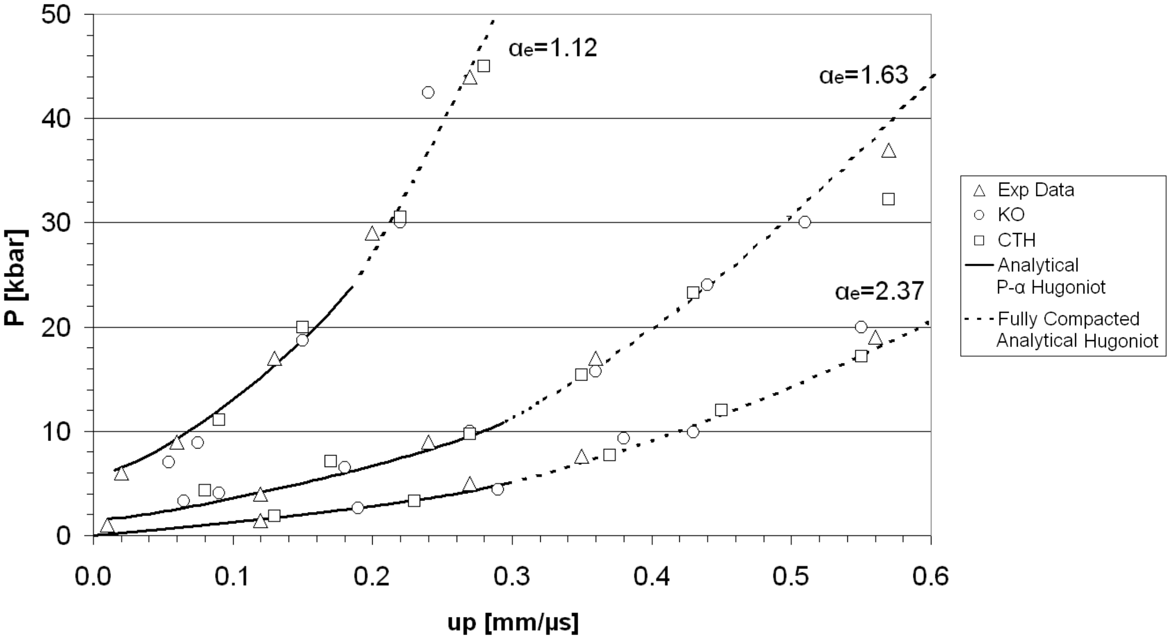

Figure 34. Fe on Fe powder comparison of the experimental data, analytical *P-α* Hugoniot, and CTH and KO computational data in P-u_p space for each initial powder density.

The solid curves are the analytical *P-α* Hugoniot curves as derived by Hermann in section 2.3. The dotted curves are the fully compacted analytical Hugoniot curves as derived by Meyers in section 2.4. These two curves meet continuously at $\alpha = 1$, see Figure 8 (b). There are three continuous curves for each initial powder density. The computational data from CTH and KO represent a specific experiment or simulation of a known flyer velocity. The experimental data is shown as the large triangles, and the square and circular points are CTH and KO simulations, respectively. For all three values of α_e, the experimental data and analytical Hugoniot curves are in agreement. The Hugoniot curves are calculated using the plastic portion of the P-α model for particle velocities corresponding to $\alpha > 1$. For $\alpha < 1$, the pressure and particle velocity are calculated using equations 13 and 14 from section 2.4.

KO and CTH implemented the *P*-*α* model at the arbitrarily picked initial flyer velocities listed in Tables 5 (a) and (b). The pressure was calculated from the release wave on the front gage, and the particle velocity was calculated form the peak wave on the back gage. After each experiment was simulated in CTH and KO, u_p-t graphs were used to check if the data retained a square wave in order to calculate the Hugoniot particle velocity in the powder. If the data retained the square wave as in Figure 35, then the Hugoniot particle velocity was easily obtained; however if the data resembled Figure 36, then the Hugoniot particle velocity was calculated by averaging the data from peak to peak.

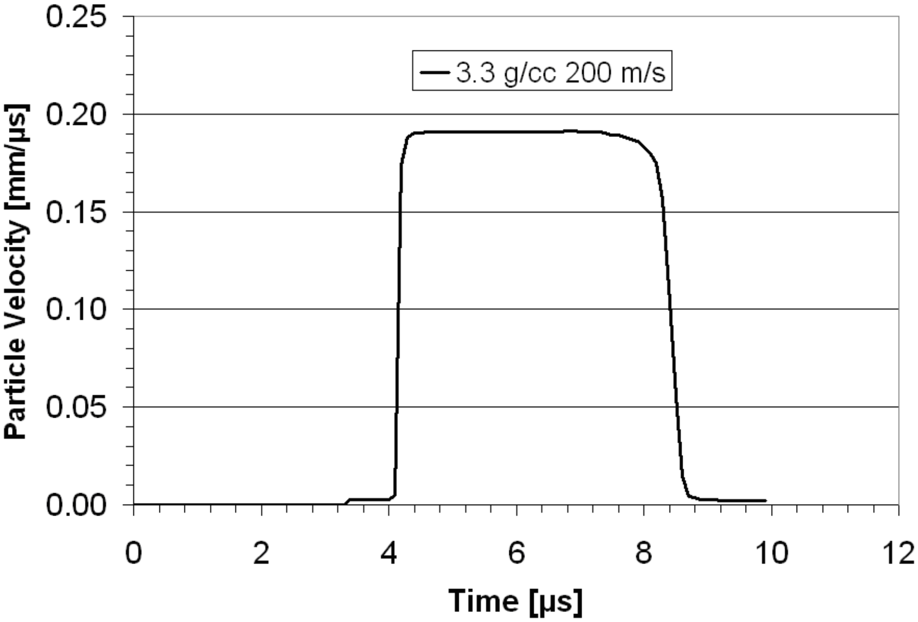

Figure 35. Example of KO u_p-t trace for the release pressure on the front gage for 3.3 g/cc 200 m/s

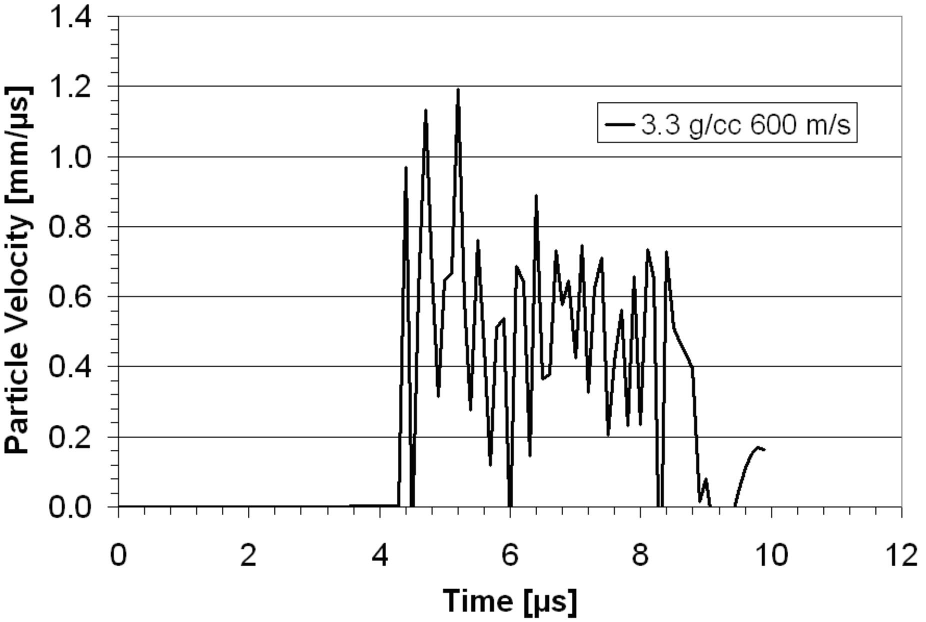

Figure 36. Example u_p-t trace for the release pressure on the front gage for 3.3 g/cc 600 m/s

The front gage release pressure data followed a square wave better than did the back gage particle velocity data, this is expected because the powder hasn't been shocked yet. Also as the initial flyer velocity increased, the data tended to get noisier. This is expected, because as the shock speeds increase, so will the shock interactions in the powder. The pressure was determined from the data and P-t graphs on the front gage in the same fashion as the Hugoniot particle velocity on the back gage was determined. Using this procedure KO and CTH produce the relatively similar results for each of the powder densities of interest across all the experiments. Therefore, KO, and the implementation of P-α, has been verified as working as well as CTH for the dynamic compaction of porous Fe powder for an $\alpha_e < 2$.

With these experimental versus numerical results it is concluded that the P-α model within both CTH and KO has been validated.

6.4. Solid on Porous Compaction – PMMA on Porous Silica

This experiment was conducted at Cambridge University with a PMMA flyer hitting porous amorphous Degussa Sipernat 50 µm silica powder that is packed in between PMMA plates as seen in Figure 2 (a). There are 3 initial densities for the silica: 0.1, 0.25, and 0.7 g/cc, and there are 5 particle velocities for each density ranging from about 220 to 1100 m/s. Figure 37 shows the U_s-u_p Hugoniot for porous silica against extrapolated experimental data found from Figure 3.

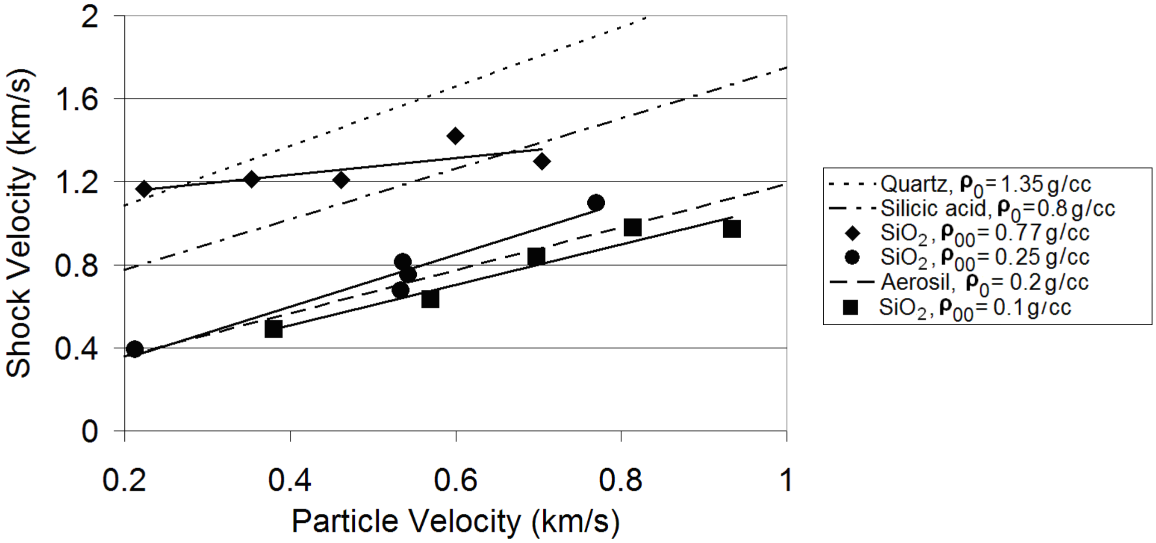

Figure 37. U_s-u_p Hugoniot for porous silica compared with extrapolated data from Figure 3.

The extrapolated aerosil data has a slope and bulk sound speed (y-intercept) that fits well to the 0.25 g/cc and 0.1 g/cc silica powder slopes as seen in Figure 37. Neither the quartz nor the silicic acid have a slope or bulk sound speed that fits well to the 0.77 g/cc powder. In general a change in slope of the U_s-u_p Hugoniot indicates that the material is undergoing a phase change. Since the experimental data is being extrapolated, there isn't any guarantee that the powder has changed phase.

Table 6 shows the dimensions and particle velocities for the 15 experiments with last 5 columns referring to Figure 2 (a).

Table 6. Flyer plate experimental setup, refer to Figure 2 (a).

Specific Volume [cc/g]	Density [g/cc]	Shot Velocity [m/s]	Front plate t_a [mm]	Front plate t_b [mm]	Powder Thickness [mm]	Back plate t_c [mm]	Back plate t_d [mm]
10	0.10	405	5	3	3	0	20
10	0.10	603	5	3	3	3	20
10	0.10	758	5	3	3	0	20
10	0.10	900	5	3	3	3	20
10	0.10	1100	5	3	3	3	20
4	0.25	220	2	2	3	0	10
4	0.25	599	2	2	3	0	10
4	0.25	600	2	2	1	0	10
4	0.25	603	2	2	5	0	10
4	0.25	900	2	2	3	0	10
1.30	0.77	280	2	2	3	0	10
1.30	0.77	455	2	2	3	0	10
1.30	0.77	603	2	2	3	0	10
1.30	0.77	800	2	2	3	0	10
1.30	0.77	979	2	2	3	0	10

The equation of state constants for the CTH and KO calculations can be found in Table 7.

Table 7. KO and CTH equation of state constants for PMMA on Silica[10, 35]

	Cambridge Data				
CTH and KO input values	**Silica powder**			**Silica**	**PMMA**
Density, ρ [g/cc]	0.77	0.25	0.10	2.2	1.182
Specific volume v [cc/g]	1.299	4.000	10.000	0.455	0.846
Porosity	65.00%	88.64%	95.45%	0.00%	0.00%
Specific Heat, c_v [ergs/g/eV]	1.0e10	1.0e10	1.0e10	1.0e10	1.11e10
Slope, s	0.41	1.28	1.15	0.1048	1.23
Bulk sound speed, c_0 [cm/μs]	0.1071	0.0121	0.0035	0.5124	0.273
Grüneisen parameter, Γ	0.9	KO 2.8 CTH 0.9	0.3	0.9	0.85
k_1 [Mbar]	8.831E-03	3.660E-05	1.225E-06	5.776E-01	8.809E-02
k_2 [Mbar]	3.267E-03	4.246E-05	2.634E-06	-1.389E-01	1.793E-01
k_3 [Mbar]	1.195E-03	4.873E-05	4.438E-06	-3.545E-02	3.077E-01
Poisson, μ	0.333	0.333	0.333	0.333	0.3
Pfrac [Mbar]	1.00E-09	1.00E-09	1.00E-09	1.00E-09	1.00E-03
Yield, Y [Mbar]	1.00E-09	1.00E-09	1.00E-09	1.00E-09	6.80E-05
Shear Modulus, G [Mbar]	2.80E-02	2.80E-02	2.80E-02	2.80E-02	2.50E-02
α_p	2.86	8.80	22.00	-	-
α_e	2.86	8.80	22.00	-	-
P_e [Mbar]	0	0	0	-	-

P_s	[Mbar]	0.0285	0.005	0.002	-	-

In order to determine the proper resolution for each experiment, the mesh was converged for both CTH and KO. The variability in the *P-t* results for both CTH and KO as a function of mesh resolution is presented in Figures 38 and 39 respectively.

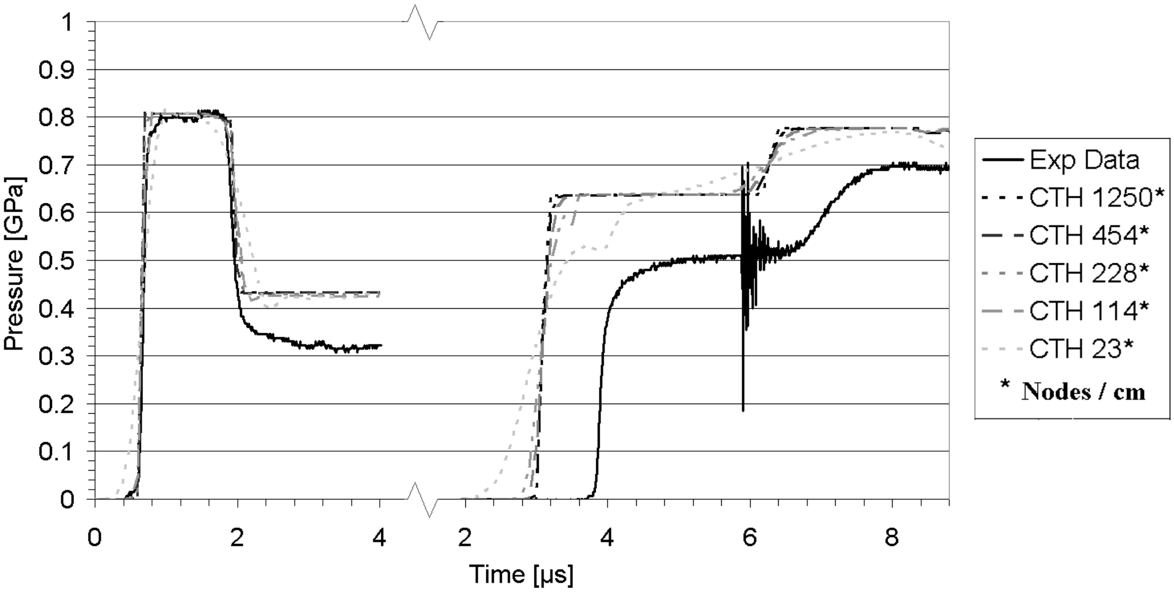

Figure 38. CTH mesh convergence for 0.77 g/cc 455 m/s *P-α* model

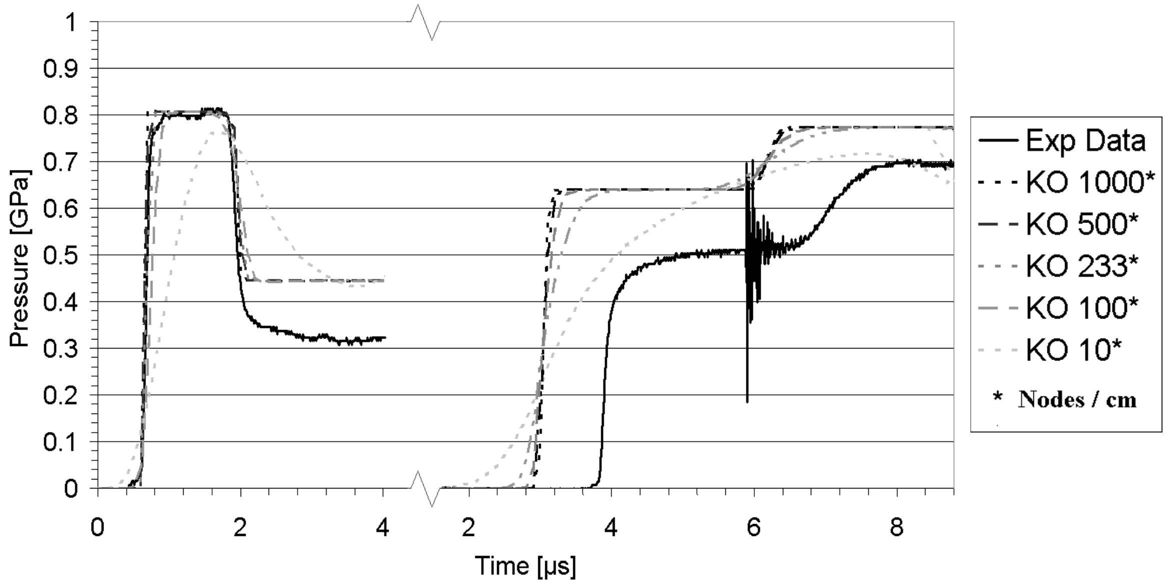

Figure 39. KO mesh convergence for 0.77 g/cc 455 m/s *P-α* model

The large variability reported by the back gage at approximately 6 μs is due to noise generated when the front gage failed. The results of Figures 38 and 39 indicate that the mesh converges at 1000 nodes /cm for KO and 1250 nodes / cm for CTH where the difference on the time of arrival on the back gage between 1000 and 1250 nodes / cm was 0.03 % . Over all the 15 experiments listed in Table 6, CTH computed the dynamic compaction to a time of 16.8 μs after impact in fewer than 20,000 iterations with a wall clock time under 20 minutes on a Linux 1 GHz Xeon processor.

KO for the 0.77 g/cc silica powder experiments computed the dynamic compaction to 16.8 μs in fewer than 4000 iterations and under a wall clock time of 5 minutes on a 2.8 GHz Pentium 4 processor. For the 0.25 and 0.1 g/cc silica powder experiments, the most computationally expensive experiment to simulate was the 0.1 g/cc powder MG at an initial flyer velocity of 1100 m/s. This is a direct result of the Courant stability criteria which requires that the time step be a function of the cell size divided by the shock speed. The powder with the smallest initial density, i.e. 0.1 g/cc, will crush the most and result in the smallest cell size. The experiment with the highest impact velocity will result in the fastest shock wave. Thus the combination of ρ_{00} = 0.1 g/cc with a1100 m/s impact velocity increases the shock speed, and reduces the time step. On the same P-3 processor, the wall clock time was about 30 hrs, and 10 million iterations at a resolution of 500 nodes / cm. The resolution of the intermediate 0.1 g/cc shots required a lower resolution, because those simulations failed to yield results at higher resolutions to be discussed in section 5.2.4.3. The resolution for each simulation is shown in Table 8.

Table 8. KO and CTH simulation parameters

Density, ρ_{00} (g/cc)	Shot Velocity (m/s)	KO Nominal Resolution (nodes/cm)		CTH Nominal Resolution (nodes/cm)	KO Sound speed divisor	
		MG	*P-α*		MG	*P-α*
0.10	405	1000	1000	1250	2	4
	603	100	1000		5	2
	758	100	1000		2	5
	900	100	1000		2	5
	1100	500	1000		2.1	1.9
0.25	220	1000	1000		2	3
	599				5	5
	600				5	5
	603				5	5
	900				5	4
0.77	280				5	5
	455				5	5
	603				5	5
	800				5	5
	979				5	5

6.4.1. 0.77 g/cc silica powder results

The results for the 0.77 g/cc silica powder can be seen in Figures 40-44.

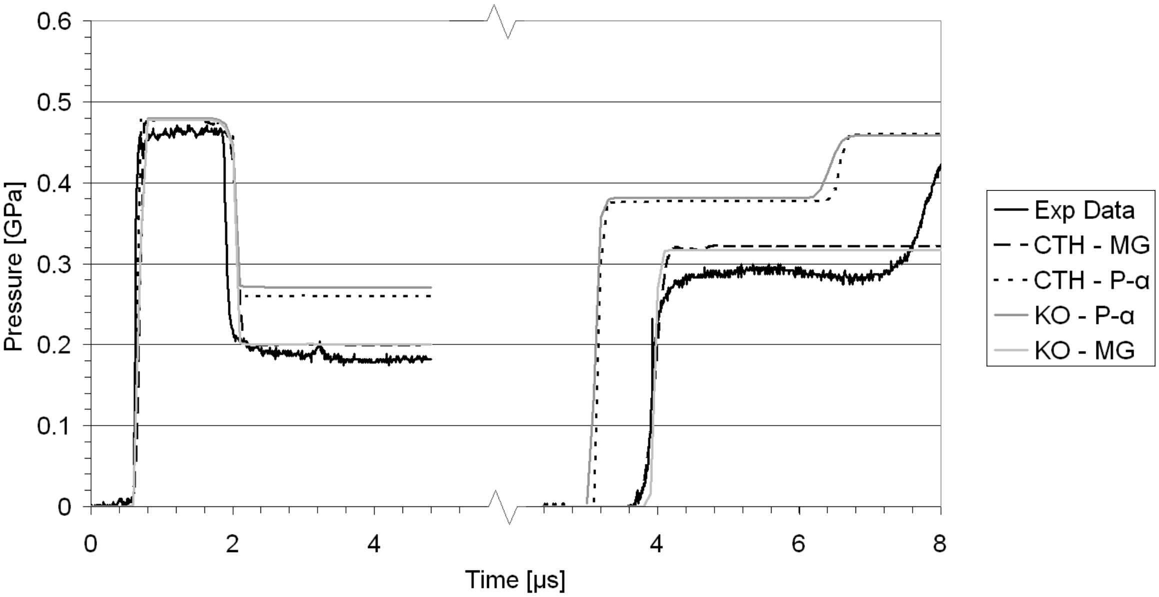

Figure 40. *P-t* diagram for 0.77 g/cc with initial flyer velocity of 280 m/s.

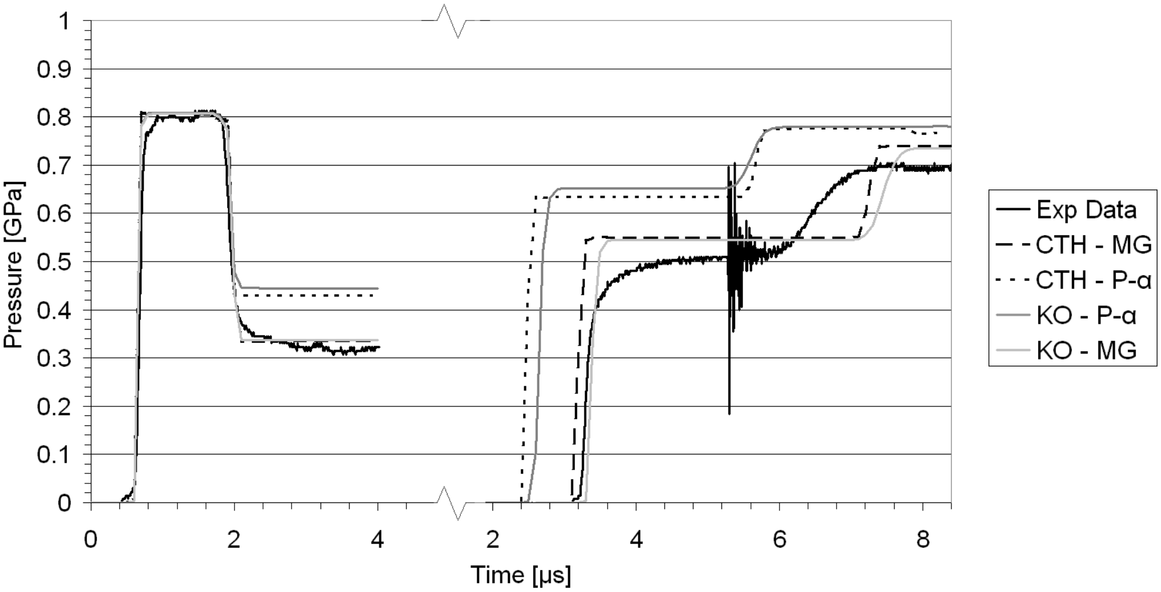

Figure 41. *P-t* diagram for 0.77 g/cc with initial flyer velocity of 455 m/s.

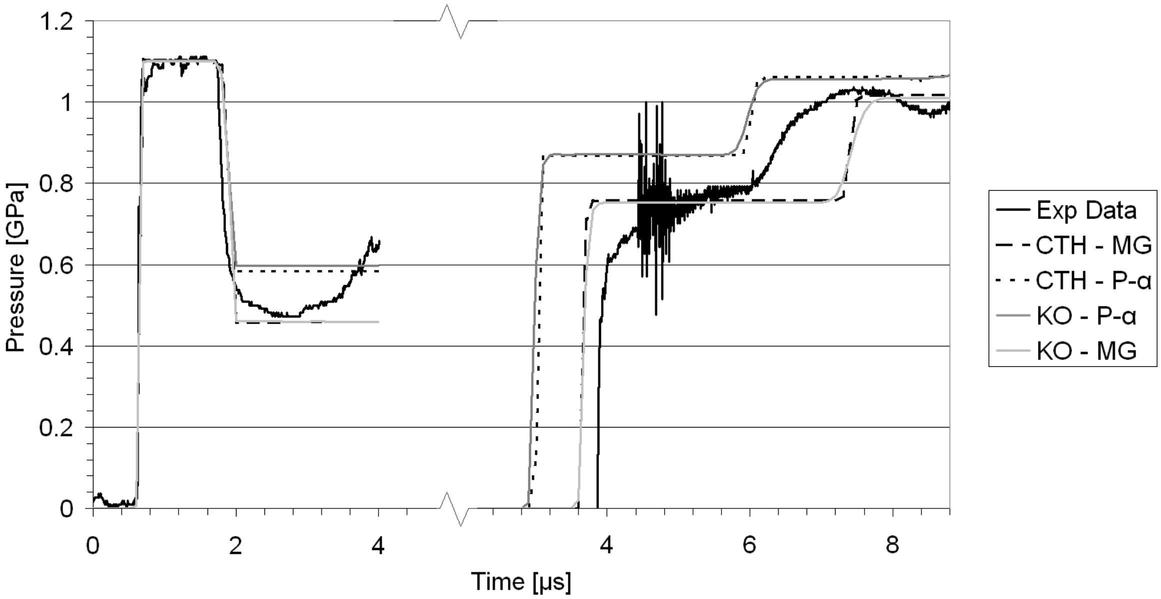

Figure 42. *P-t* diagram for 0.77 g/cc with initial flyer velocity of 603 m/s.

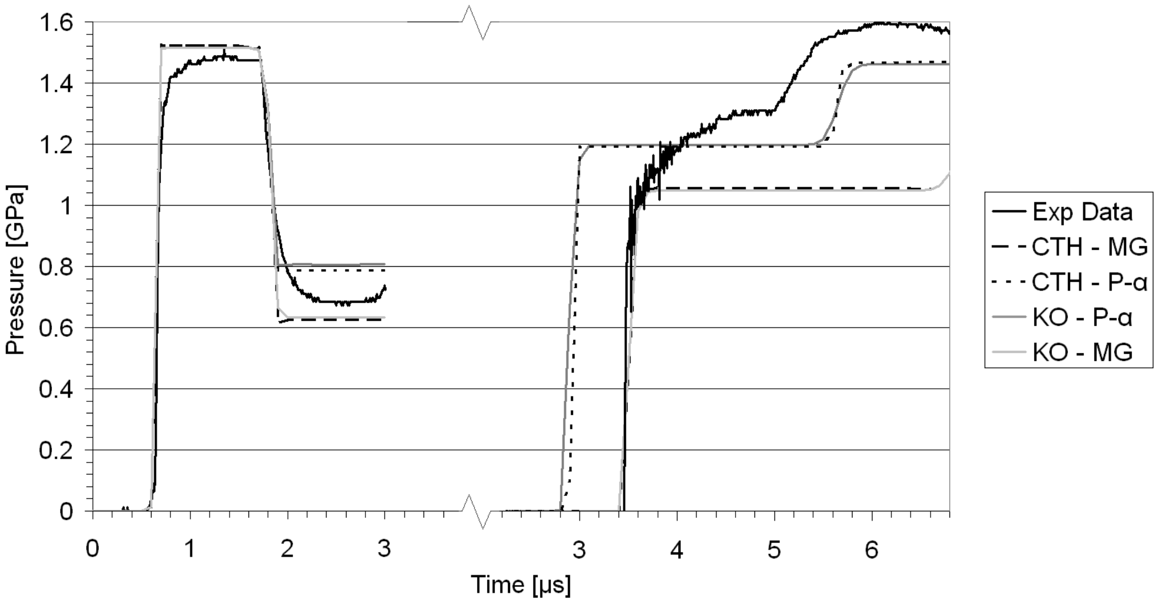

Figure 43. *P-t* diagram for 0.77 g/cc with initial flyer velocity of 800 m/s.

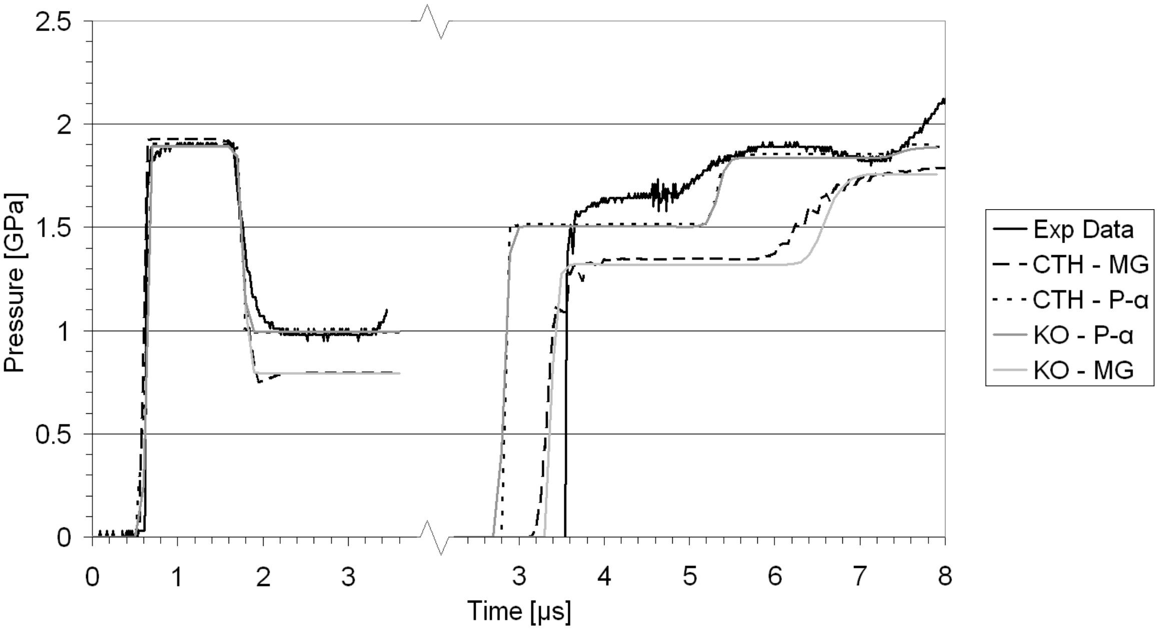

Figure 44. *P-t* diagram for 0.77 g/cc with initial flyer velocity of 970 m/s.

Each of the previous 6 figures represent a different experiment by flyer velocity only, and have the front and back gage data with a time frame adjustment shown. The first peak wave represents the Hugoniot peak pressure within the PMMA as the shock traverses the front gage. The rounding of the experimental data at the top of the initial rise and fall of the peak pressure is a result of the PMMA flow at release. The release pressure on the front gage represents the shock interaction between the PMMA and the silica powder. The back gage should have a pressure rise equivalent to the front gage release pressure, and then ideally should become a series of stepped square waves that represent the reflected and rarefaction waves interacting towards the end of the experiment in the silica. However, the experimental data shows a gradual rise in pressure that resembles square wave behavior. One theory holds that the silica powder gives weak compaction waves instead of instantaneous shock waves. Also, Yaziv et al.[36] showed that manganin, work hardens as it is being strained, and developed a model that can calibrate manganin at unloading. If the manganin on the front gage is plastically deforming as the initial shock wave passes, the gage will not return to the original length. Therefore, when the reflected shock passes by the manganin gage on the front the release pressure will always retain residual stress that will be added onto the release pressure. This can explain why experimentally the front gage release pressure is not equivalent to the back gage peak pressure, however computationally the release pressure on the front and back does equal to the peak pressure on the back gage. Future work could integrate computationally any of the manganin models referenced here.

For Figures 40-44, the computational codes do not exactly match the experimental data; however, each produces similar results. CTH and KO compare favorably for the initial rise time and peak pressure for the front gage across all initial flyer velocities. This is to be expected since the shock Hugoniot for PMMA is well known [1]. Both MG and *P-α* for either CTH or KO give nearly identical results for the front gage and compare well with the experimental data. Therefore as expected PMMA is well characterized by these models in both hydrocodes. In terms of the release pressure, the MG EOS tends to model the experimental data better for initial flyer velocities less than or equal to 603 m/s, neither reproduces the experimental data well at 800 m/s, and *P-α* tends to model the experimental data better at 970 m/s. *P-α* has a release pressure that is consistently higher than MG for all the experiments.

For the back gage the MG EOS consistently predicts the initial rise time, and does an adequate job of predicting the peak pressure for the experimental data for the initial flyer velocities below 800 m/s. *P-α* predicts the initial rise time to be earlier for all experimental runs, and also has a higher peak pressures than MG. Also for the 970 m/s run, *P-α* does a better job of predicting the peak pressure. This is expected, because the front gage release pressures for the experiments under 800 m/s were predicted better with MG, and for the 970 m/s run *P-α* predicted the experimental data better. The “steps” that are shown at the latest time for the back gage are wave interactions that occur when reflected waves and/or rarefaction waves collide. These rarefaction waves are generated when the shock waves reach the free surface and propagate back into the target. In terms of the experiment, the simulations are generally considered validated before those interactions reach the gages.

Also, the computational models are consistent with each other for all initial flyer velocities. The front and back gages are relatively the same for MG and *P-α*, respectively. This indicates that for the 0.77 g/cc powder, KO predicts the dynamic compaction characteristics of the silica powder as well as CTH for the *P-α* and MG models.

Furthermore, Figure 45 shows in P-v space the computational, experimental, and analytical Hugoniot curves for CTH and KO implementing the MG and P-α equations of state for 0.77 g/cc silica powder.

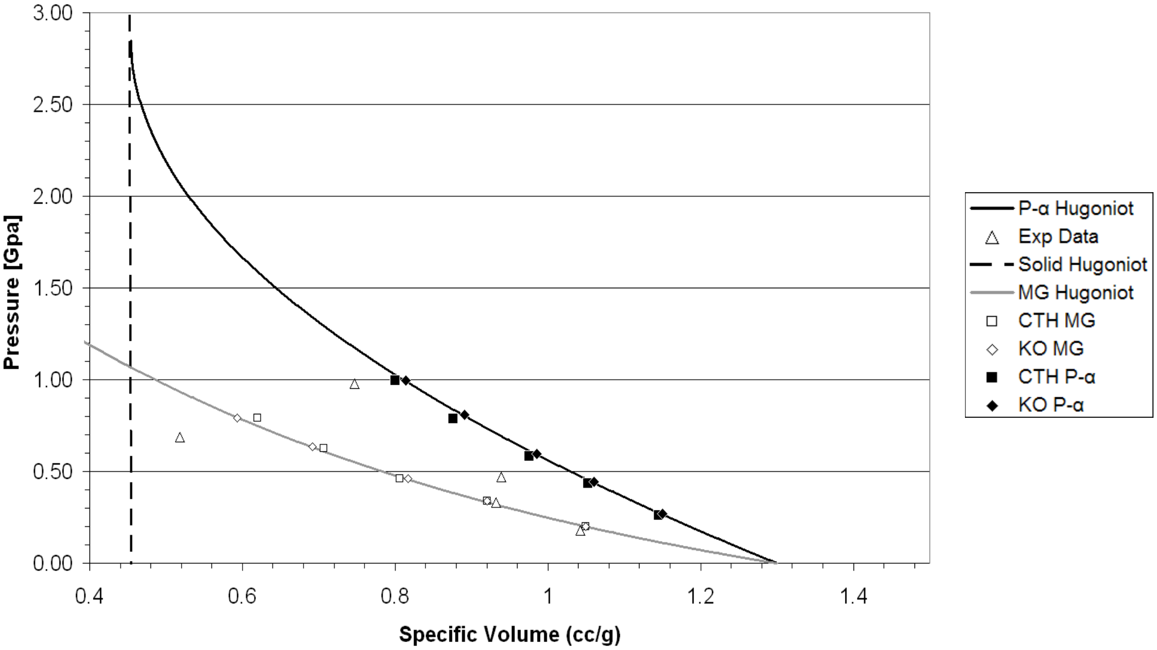

Figure 45. P-v diagram showing the computational, experimental, and analytical Hugoniot curves for 0.77 g/cc silica powder

CTH and KO reproduce the analytical Hugoniot curves for MG and P-α, respectively. The experimental data closely follows the MG and P-α theoretical Hugoniot curves. The dotted Hugoniot curve is the solid silica Hugoniot, which meets the P-α Hugoniot at the given value of P_s = 2.85 GPa. Figure 45 explains the variability in the calculations with respect to the data as seen in Figures 40-44. The solid grey line in Figure 45 is a linear curve fit to the data in U_s-u_p space, transformed via the jump equations to P-v space. There is a large amount of variability between the data and the linear Mie-Grüneisen Hugoniot curve fit. The computations faithfully follow the curve fit MG Hugoniot, which is the input equation of state. As a result there is variably in the calculations with respect to the data. The *P-α* Hugoniot represents a best guess to the actual MG Hugoniot in the absence of data. Although the computations utilizing the *P-α* EOS, as would be expected, follow the *P-α* Hugoniot, it is obvious from the Figure 45 that the best guess does not accurately represent the data.

6.4.2. 0.25 g/cc silica powder results

The EOS constants for the silica powder with an initial density of 0.25 g/cc for CTH and KO are listed in Table 7. These constants differ only in Grüneisen coefficient. For all of the experiments, the simulated back gage initial rise time utilizing the MG EOS significantly differed from the experiment, especially when simulating the experiment with an impact velocity of 220 m/s. However, for KO it was found that by increasing the Grüneisen coefficient the back gage initial rise time would also increase as seen in Figure 46.

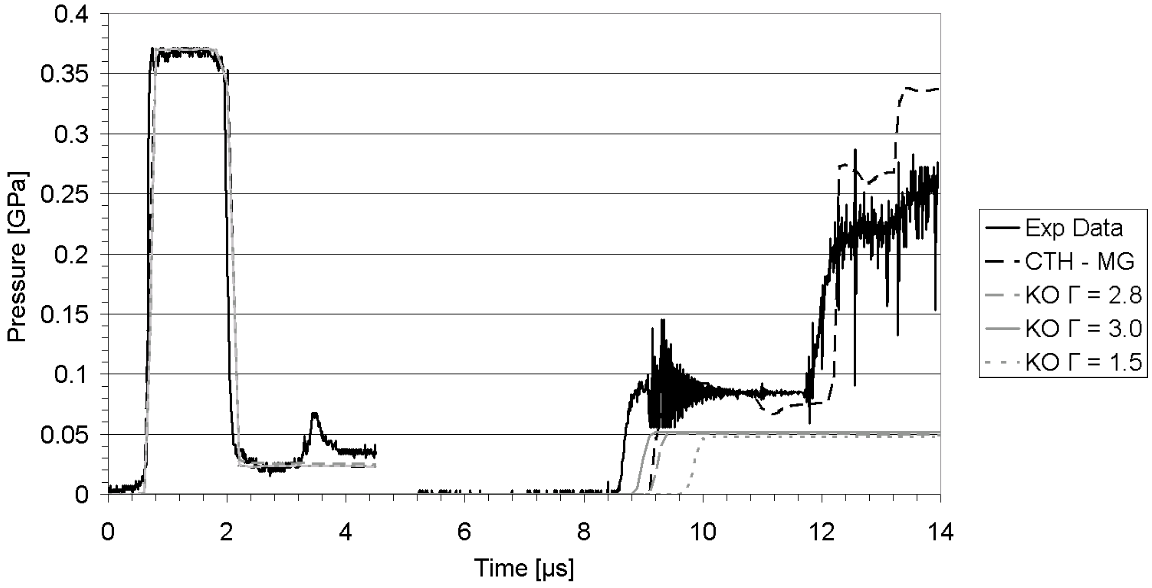

Figure 46. *P-t* diagram for 0.25 g/cc with initial flyer velocity of 220 m/s with *Γ* variation.

The Grüneisen coefficient's effect on the rise time of the silica powder stems from the equation of pressure in the MG EOS. Pressure is the summation of the volumetric and energetic nature of the medium. Each of these terms is a function of Γ. In terms of the volumetric pressure term, Γ is only found in the higher order x terms, i.e. k_2 and k_3. Equation 103 shows how Γ affects the energy portion of the pressure. As the energy or volume inside the powder increases, the pressure will to rise. If the energy is being multiplied by a larger number the pressure will start to rise sooner, and vice versa. Therefore from Figure 46, iterating for Γ on the 220 m/s case shows that 2.8 generates the best result to achieve the same rise time as CTH. The reason why CTH was chosen as the reference point and not the experimental data is only because KO to CTH verification is the main focus here.

As a check, Γ was increased in the same fashion for MG in CTH with no effect in the initial rise time or the peak pressure for the front or back gages. It is suspected that the cause for this is that CTH only uses the Grüneisen coefficient as a means for calculating temperature. Thus, this coefficient is not a function of pressure for CTH. The Grüneisen coefficient was set to 2.8 for all the MG simulations in KO for the silica powder with an initial density of 0.25 g/cc.

The schematic for each experiment is shown in Figure 2 (a) with the dimensions listed in Table 6. The powder thicknesses for the flyer plate velocities of 599, 600, and 603 m/s experiments are 3, 1, and 5 mm, respectively. The pressure - time traces for the silica powder with an initial density of 0.25 g/cc are shown in Figures 47-51.

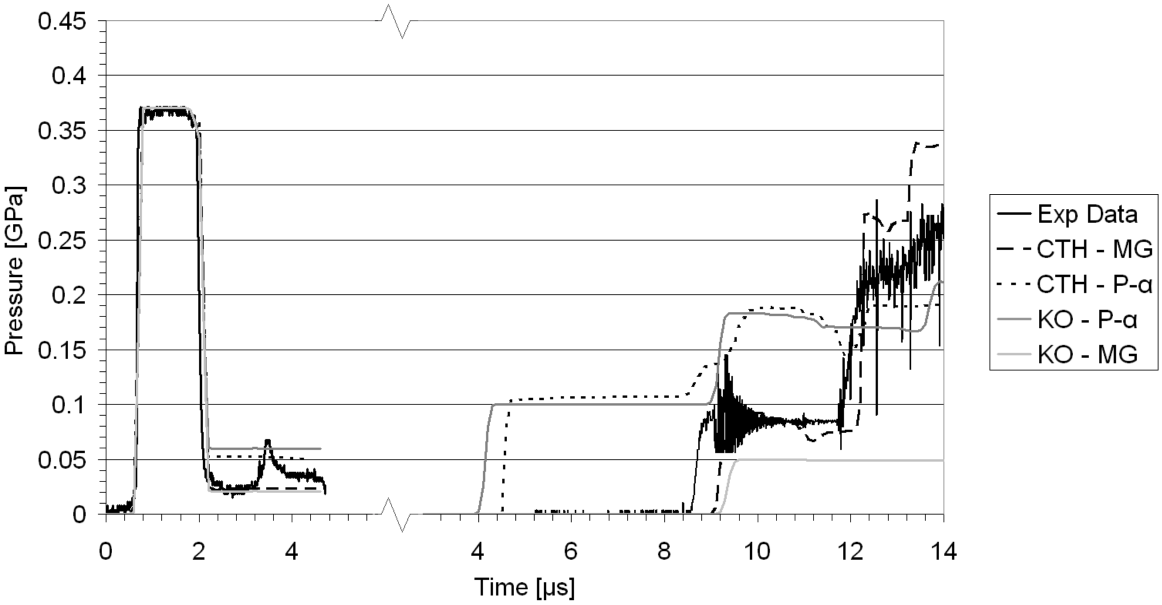

Figure 47. *P-t* diagram for 0.25 g/cc with initial flyer velocity of 220 m/s.

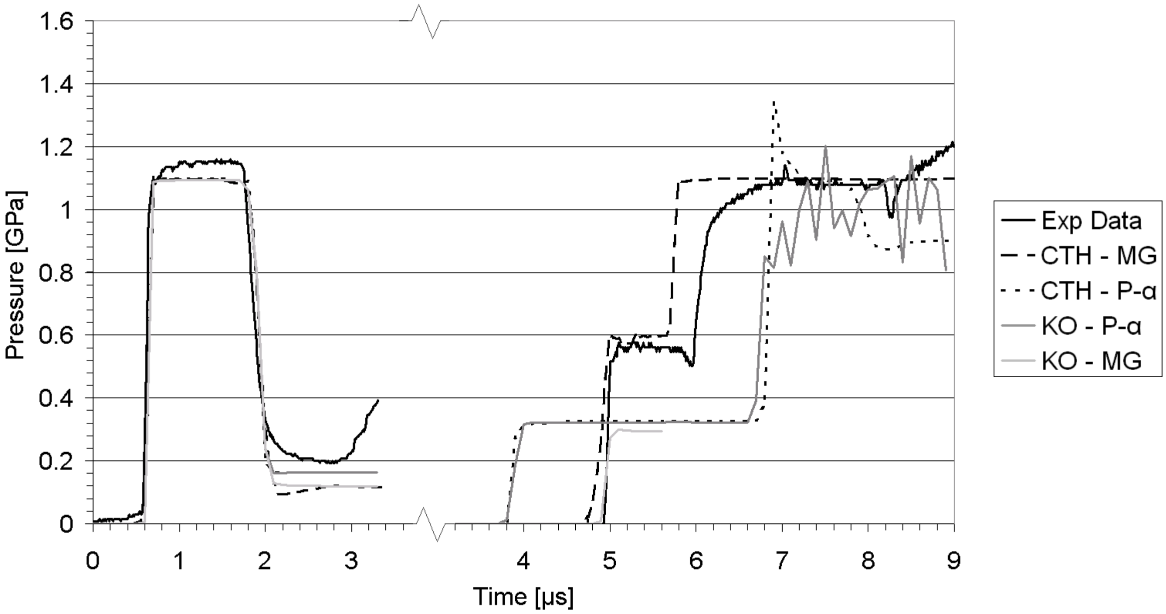

Figure 48. *P-t* diagram for 0.25 g/cc with initial flyer velocity of 599 m/s.

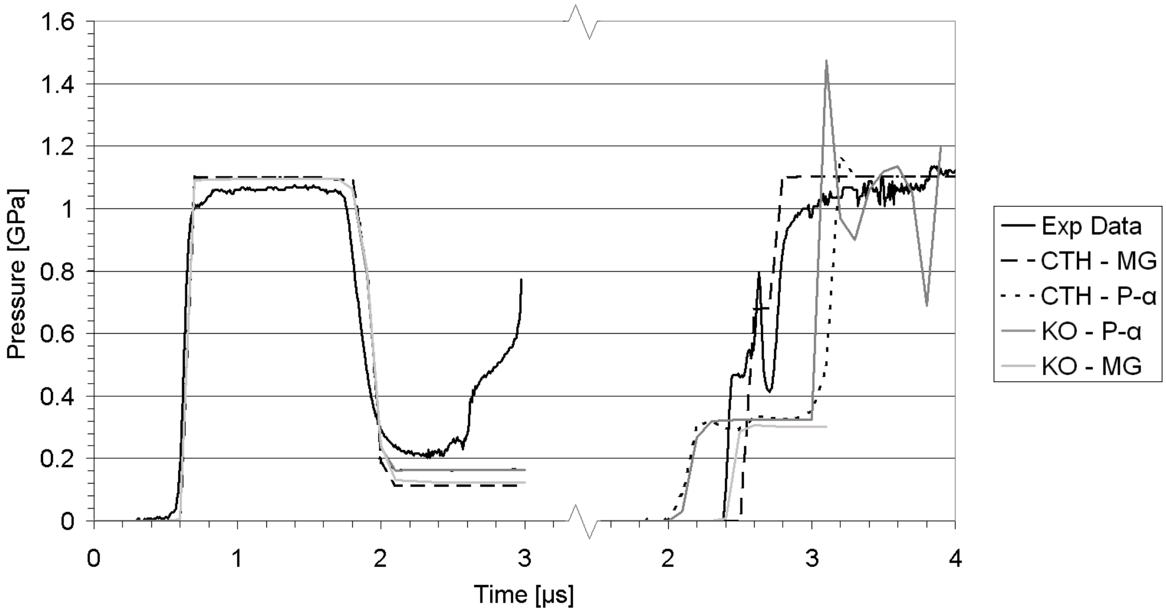

Figure 49. *P*-*t* diagram for 0.25 g/cc with initial flyer velocity of 600 m/s.

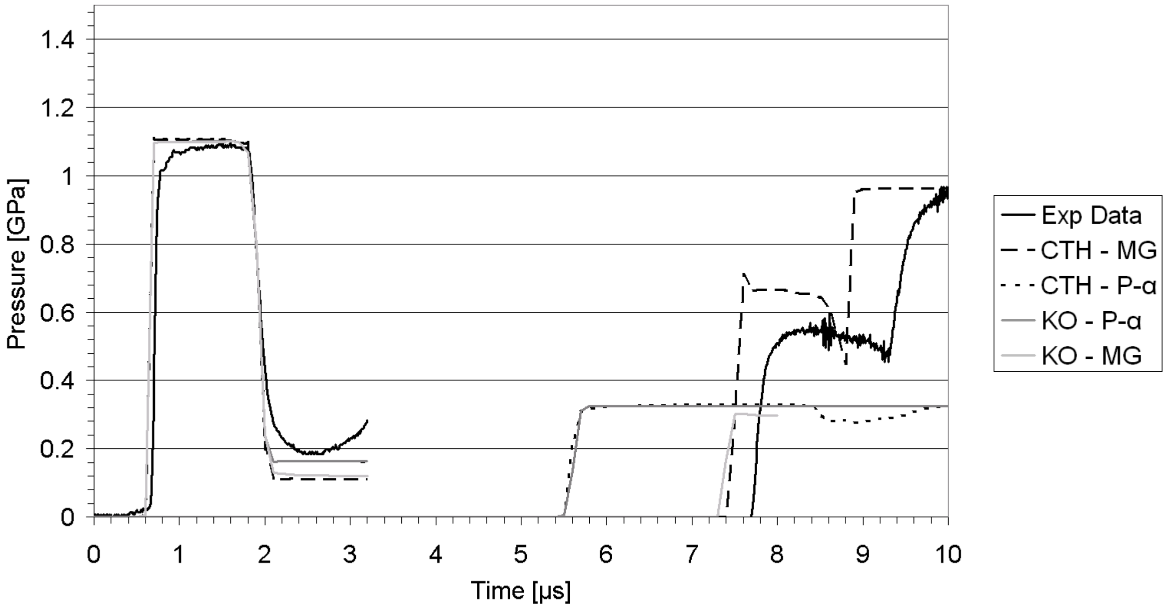

Figure 50. *P*-*t* diagram for 0.25 g/cc with initial flyer velocity of 603 m/s.

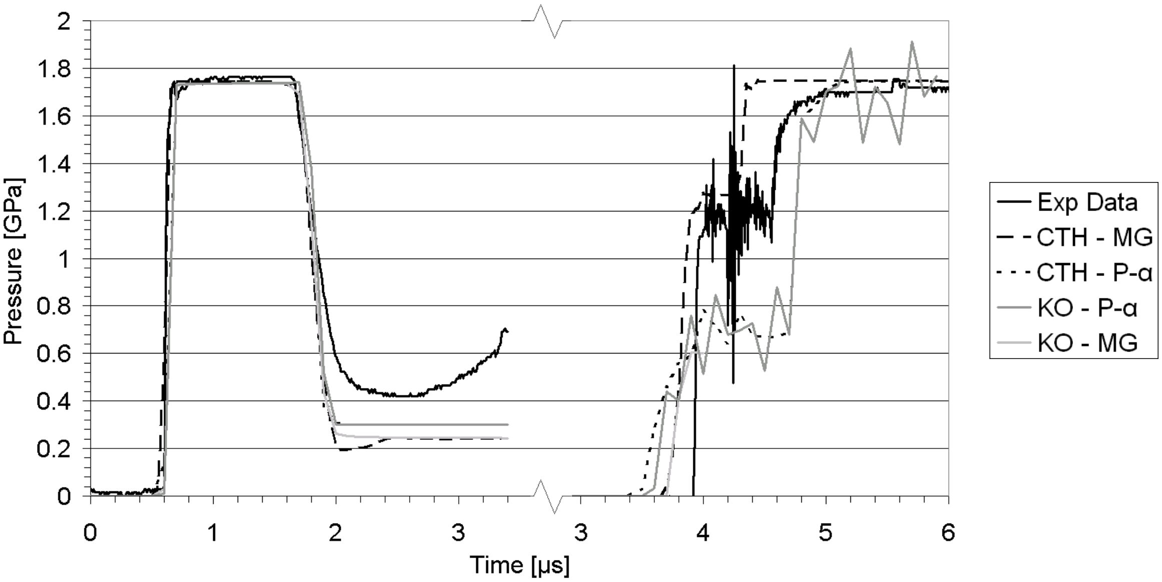

Figure 51. *P-t* diagram for 0.25 g/cc with initial flyer velocity of 900 m/s.

The above Figures 47-51 show that the experimental results obtained from the front gage embedded in the PMMA is well characterized by both the MG and *P-α* equations of state in both CTH and KO across all initial flyer velocities. Unlike the silica powder with an initial density of 0.77 g/cc, the simulations utilizing the *P-α* EOS better predict the experimental release pressure on the front gage than MG. As the initial flyer velocities decrease from 900 m/s the release pressure prediction by *P-α* approaches the experimental release pressure. KO and CTH have almost identical traces on the front gage for MG and *P-α*, respectively.

In terms of the back gage pressure, KO and CTH both predict the *P-α* model to have an initial rise time earlier than the experimental and MG data for the back gage for each initial flyer velocity. The powder thickness in Figure 50 is 5 mm, and the *P-α* model under predicts the peak pressure on the back gage significantly. KO and CTH show fair agreement with respect to the *P-α* model for each of the initial flyer velocities. The ringing effect that is shown in Figures 48 and 51 at the tail end of the back gage on the

KO P-α model can be reduced by forcing KO take shorter time step advances as will be shown in section 5.2.4.3, however this also causes the program to run significantly longer.

The initial rise time of back gage pressure predicted by CTH provides fair agreement with the experimental data implementing MG. In Figure 47, the KO and CTH simulations of the back gage are almost identical. Figures 48-51 illustrate that for the KO simulations utilizing the MG EOS each rise to a peak pressure much lower than the experimental data and CTH.

KO wasn't able to predict the back gage data fully for all but Figure 47 at a resolution of 1000 nodes / cm, because the computational distance between nodes within the silica powder would approach 0, which in turn forces the volume to infinity. The KO program predicts that the density exceeds 10^10 g/cc. Since these densities are non-physical the simulations were terminated where the back gage data stops in time for MG in KO in Figures 48-51. Also, KO under predicts the peak pressure reported by the back gage for each of the cases in Figures 48-51.

In terms of the back gage, CTH utilizing the MG equation of state, see Figure 48 predicts the experimental data the best. The worst back gage prediction for CTH with the MG equation of state is Figure 50 with a 5 mm powder thickness. All in all the MG equation of state in CTH on the back gage most accurately predicts the experimental data. Furthermore, Figure 52 presents the computational, experimental, and analytical P-v Hugoniot space for CTH and KO implementing the MG and P-α equations of state for 0.25 g/cc silica powder.

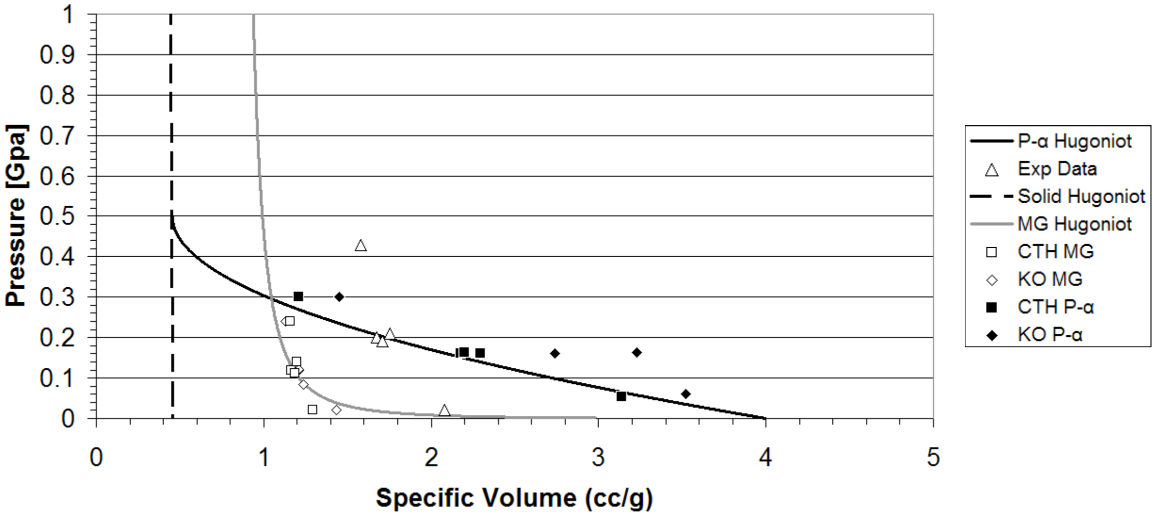

Figure 52. *P-v* diagram showing the computational, experimental, and analytical Hugoniot curves for 0.25 g/cc silica powder

As can be seen in Figure 52, the computational data for CTH and KO reproduce the MG theoretical Hugoniot curve fairly well. CTH adequately reproduces the theoretical *P-α* Hugoniot curve, but KO over predicts the pressure and specific volume. Also, the experimental data follows the MG Hugoniot curvature accurately.

The MG EOS can only be utilized knowing the experimentally determined Hugoniot; the Hugoniot is directly fit to the experimental data. Thus it is no surprise that the numerical simulations which utilize the MG EOS follow the MG Hugoniot. However, for a different material or a silica powder with a different initial density the experimental data may not be known. The *P-α* equation of state could be fitted to this data. However, the purpose of this model is to predict the unknown dynamic compaction of the powder. Thus the *P-α* EOS can be utilized as a theoretical approximation to the experimentally determined Hugoniot, and can be employed within a hydrocode without a prior knowledge of the Hugoniot.

Overall neither model in either hydrocode accurately predicts the experimental Hugoniot data very well. KO reproduces the CTH data better for MG than *P-α*, but the *P-α* model does show fair agreement from the time traces in Figures 47-51. Thus CTH verifies the *P-α* model in KO for silica powder at 0.25 g/cc, and MG model remains unverified in KO.

6.4.3. 0.1 g/cc silica powder results

Dimensions for the 0.1 g/cc silica powder experiment are presented in Table 6. At this highly distended initial powder density, KO was not able to complete the simulations at a resolution of 1000 nodes / cm. Therefore the resolution was reduced as presented in Table 8 above for each simulation. The *P-t* dynamic compaction results for the silica powder with an initial density of 0.1 g/cc are shown in Figures 53-57.

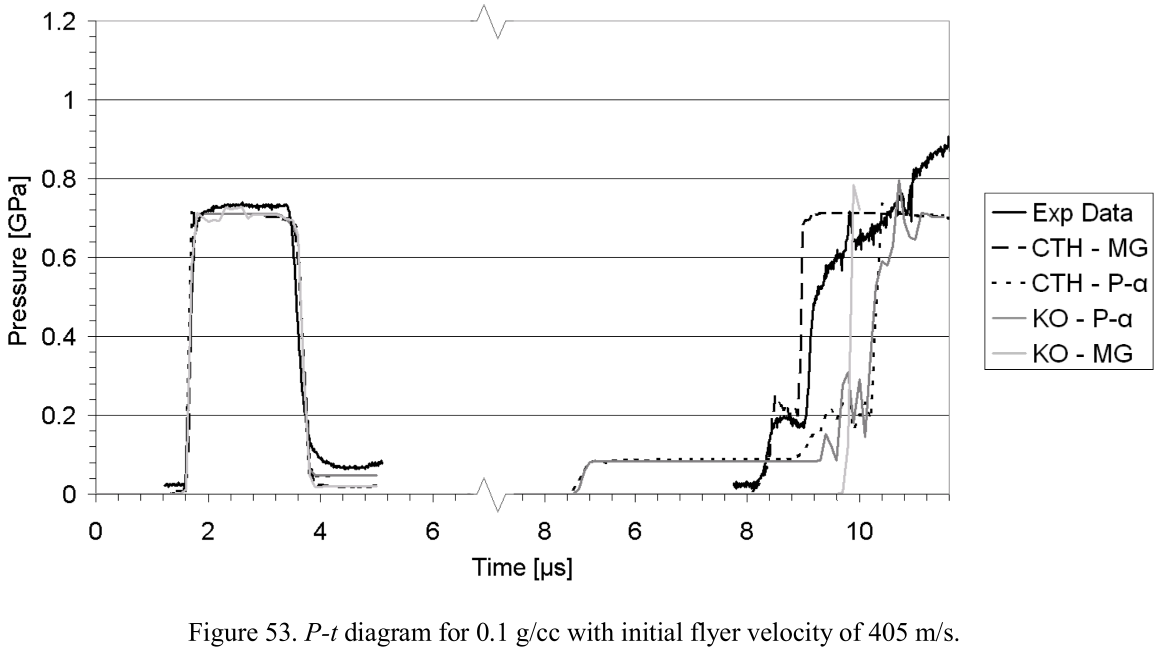

Figure 53. *P-t* diagram for 0.1 g/cc with initial flyer velocity of 405 m/s.

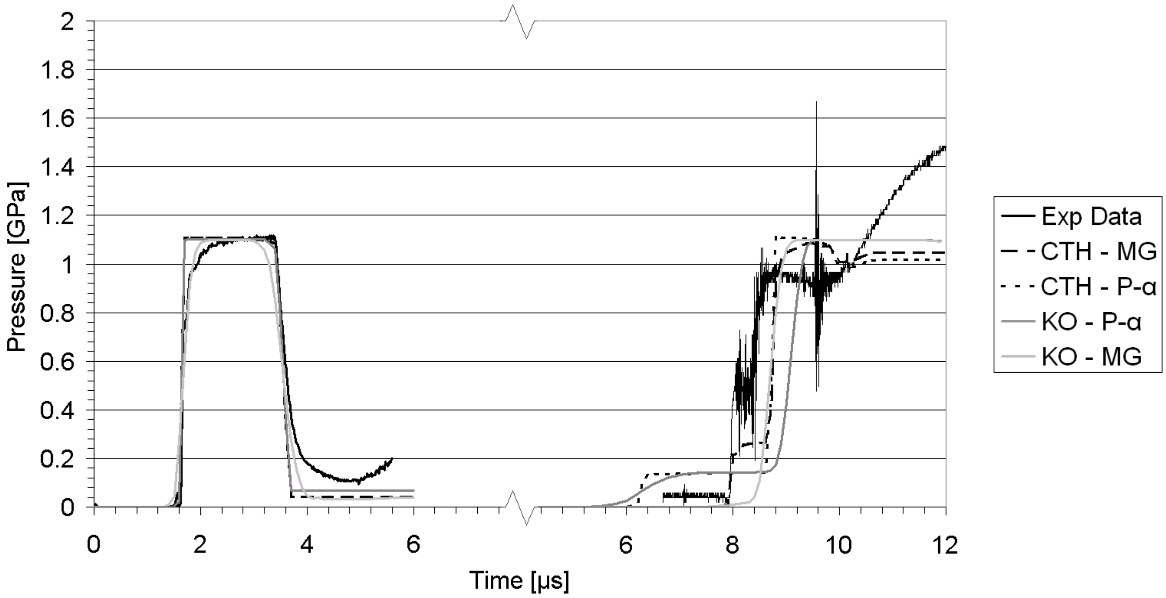

Figure 54. *P*-*t* diagram for 0.1 g/cc with initial flyer velocity of 603 m/s.

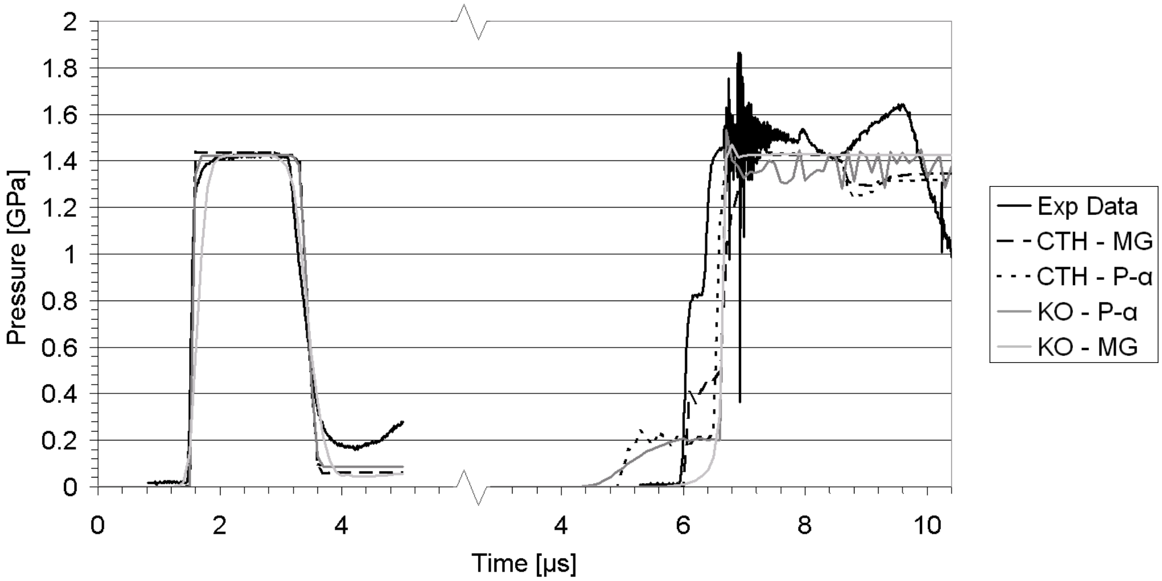

Figure 55. *P*-*t* diagram for 0.1 g/cc with initial flyer velocity of 758 m/s.

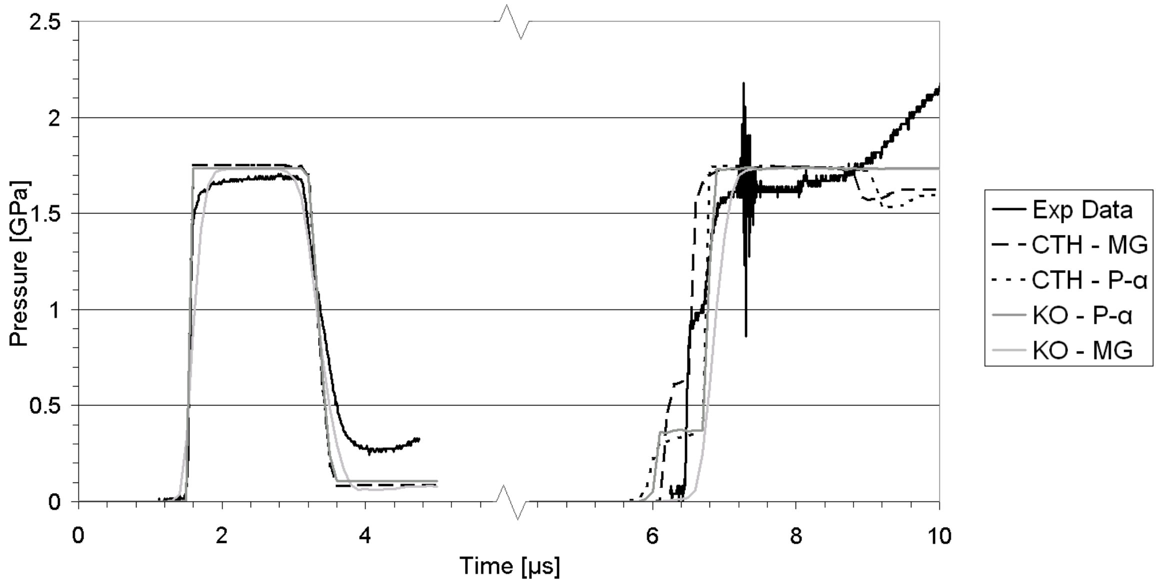

Figure 56. *P-t* diagram for 0.1 g/cc with initial flyer velocity of 900 m/s.

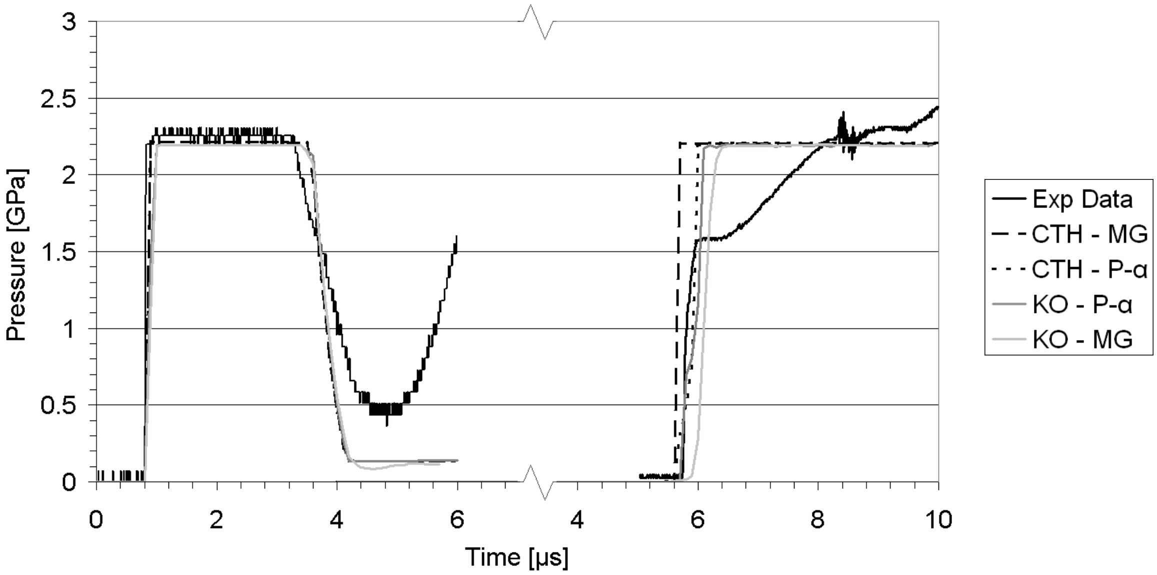

Figure 57. *P-t* diagram for 0.1 g/cc with initial flyer velocity of 1100 m/s.

As in the case of the previous two experiments with different initial densities, the front gage initial rise time and peak pressures are well characterized by both CTH and KO as compared to the experimental data utilizing either the MG or *P-α* EOS, see Figures 53-

57. The release pressures for CTH and KO are all lower than the experimental data as predicted from the manganin gage work hardening.

The KO *P-α* model has a higher resolution than the KO MG model according to Table 8. Figure 57 is an example showing that KO does allow the PMMA to be well described before the density would approach infinity, and ultimately end the simulation. The time trace in KO was simulated twice, once at the 1000 node / cm resolution to achieve the front gage data, and then at 500 nodes / cm to achieve the back gage data. The same could have been followed to obtain the results in Figures 54-56; however, this was unnecessary for this discussion.

For Figure 53, the MG equation of state poorly predicts the back gage rise time, however reaches the peak pressure. Attempts to change the Grüneisen coefficient failed to give a tuned value for the back gage rise of the experimental data. This is due to low resolution as seen in Figure 58 with the best attempt to model the back gage rise time for CTH with a Grüneisen coefficient of 2.1.

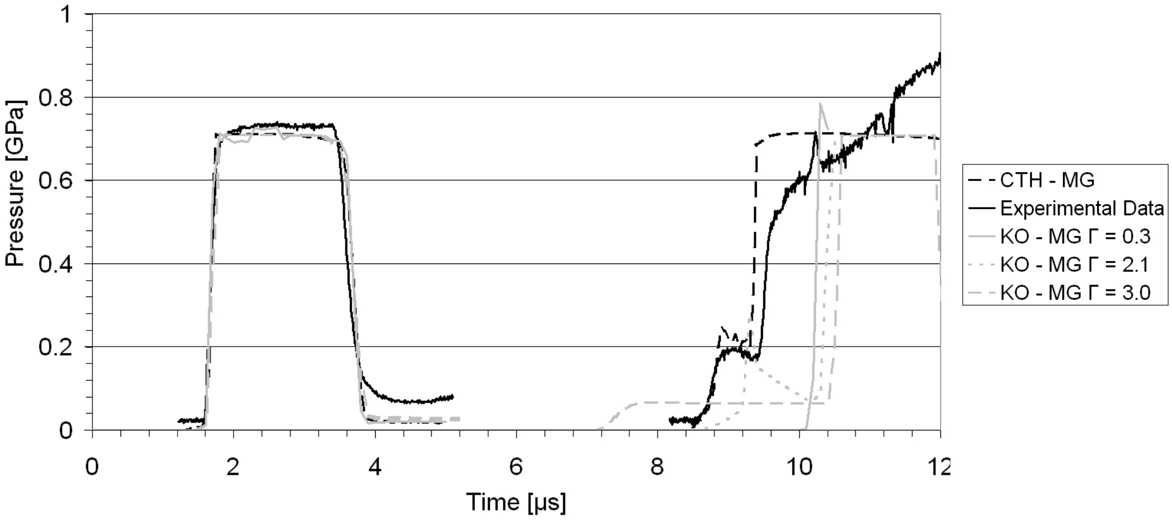

Figure 58. *P-t* trace of the experiment in Figure 53 with the Grüneisen coefficient varied

The resolution for Figure 58 is 100 nodes / cm, because this was determined to be the highest resolution the program could support for the back gage to start rising. Figure 58 also shows that there was no solution found to match the CTH back gage rise time. Therefore the initial Grüneisen coefficient of 0.3 was chosen for the remaining initial flyer velocities.

For Figures 54-57 MG in CTH predicts the initial rise times and peak pressures on the back gage with increasing accuracy with increasing initial flyer velocities. KO has a significantly lower resolution, which can account for the slight deviation from CTH on the initial rise times on the front and back gages, but the peak and release pressures are about the same.

In general, *P-α* predicts the an initial rise time on the back gage earlier than the experimental data as the initial flyer velocities decrease. The peak pressure for *P-α* is reasonable in comparison to the experimental data for KO and CTH. For Figures 52-56, the experimental data has a step in pressure before achieving the peak pressure due likely to reflected waves. The *P-α* EOS shows the same step, but since the PMMA is flowing with the impact pressure releases, and the manganin gages are work hardening, the step is skewed. KO and CTH compare to each other favorably for the *P-α* model in Figures 53-57.

There is a ringing effect that can be seen at the tail end of the back gage in Figures 53 and 55 for KO *P-α.* This is most likely numerical ringing, and does not represent any physical phenomenon. The amplitude of the ringing can be reduced by lowering the time step below the Courant stability criterion within KO. The numeric program can not advance in time any faster than the smallest tine calculated by cell length divided by shock velocity, i.e. the fastest wave in the scheme. This is known as the Courant condition. This condition prevents any information from being skipped over a node as waves traverse the numerical space. If a wave passes a node before the code has a chance to adjust the properties at that node, then non-physical phenomena can occur that can cause instabilities within the calculations and eventually lead to the program crashing. Therefore, to reduce this ringing effect, the minimum time step in the program is divided by an appropriate constant > 1, see table x for divisors used in this analysis. The program can then slow down enough to allow all information to be passed through the numerical scheme. However, increasing this divisor too high can cause the program to run significantly slower and increase error due to numerical round-off due to excessive calculations. Decreasing the divisor towards 1 can increase chances of numerical instability. An example of this procedure can be seen in Figure 59 for the 0.1 g/cc 405 m/s *P-t* diagram. These results should be compared with the results presented in Figure 53.

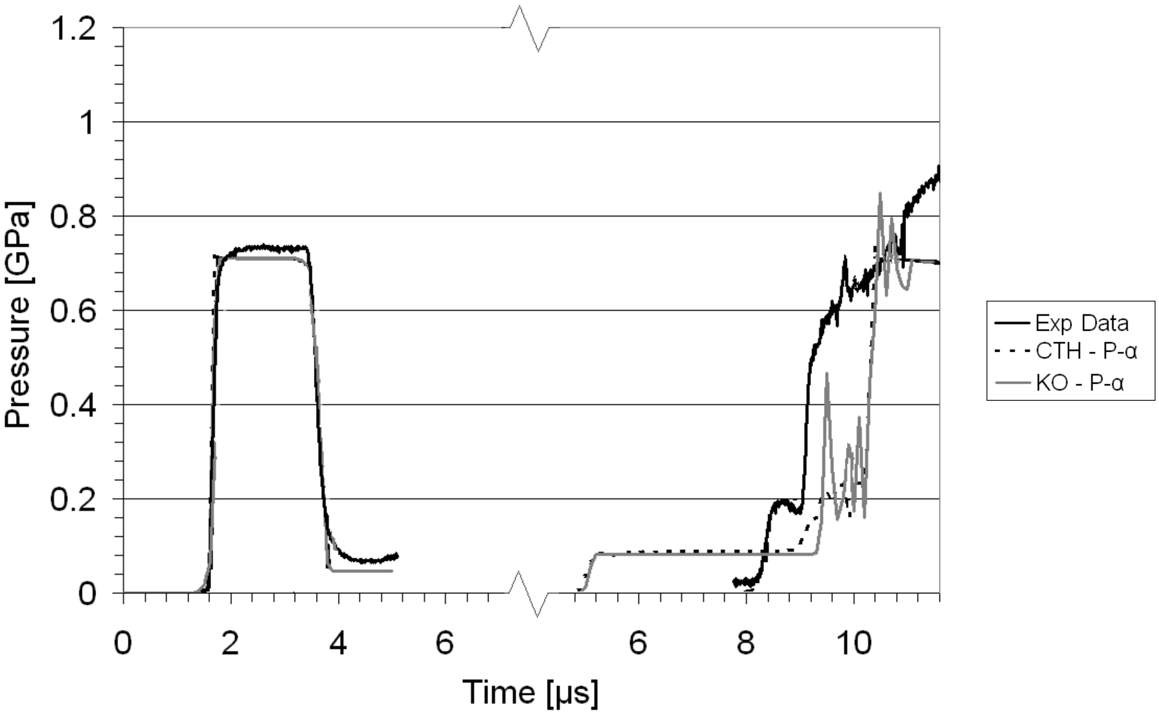

Figure 59. *P-α* model with KO time step divisor of 4 for 0.1 g/cc 405 m/s.

By comparing Figures 59 and 53, the data on the back gage of KO *P-α* has reduced ringing. The divisor in Figure 53 is 5, and the divisor is 4 in Figure 59. Divisors for all 15 experiments can be seen in Table 8.

Furthermore, Figure 60 shows in *P-v* space the computational, experimental, and analytical Hugoniot curves for CTH and KO implementing the MG and *P-α* equations of state for 0.1 g/cc silica powder.

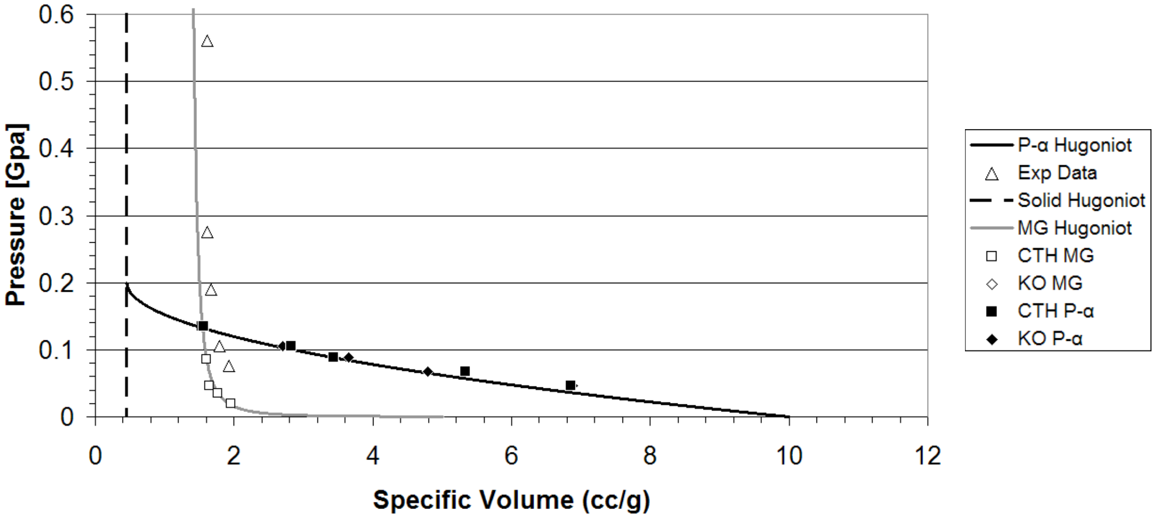

Figure 60. *P-v* diagram showing the computational, experimental, and analytical Hugoniot curves for 0.1 g/cc silica powder

Since the Hugoniot is formed by fitting experimental data it is no surprise that the experimental data as well as the computational data utilizing the MG EOS seem to follow the MG theoretical Hugoniot curve. Therefore it should be noted that the experimental data in Figures 45, 52, and 60 all follow the MG theoretical Hugoniot agreeably. The same can be said for the *P-α* Hugoniot curve and the computational data for Figures 45, 52, and 60, but not the experimental data. This is the key to the *P-α* model in that its success is based on how well the experimental data can be reproduced without prior knowledge. In this case with porous silica powder, the *P-α* model poorly reproduces the data for all the initial silica powder densities.

On the other hand, the CTH and KO computational data compare well with the MG and P-α theoretical Hugoniot curves, respectively. Thus KO is verified by CTH implementing the P-α model for 0.1 g/cc silica powder. The MG equation of state works well in CTH, but only adequately works in KO mostly due to resolution issues caused by a large density error.

*7. **Conclusions***

The static and dynamic compaction characteristics of porous silica powder have been investigated in this thesis. The static compaction experiment shows the surface area of the uncrushed powder is relatively the same as the surface area of the each compacted wafer. If the silica particles were welding together by atomic bonding, then the surface area would be decreasing per unit weight. Therefore, the results indicate that particles are not bonding together.

The distinguishing factor of this research is that the dynamic experiments investigated are in the relatively low shock velocity – particle velocity region. Also, the compaction of these highly distended powders has not been widely analyzed. There are two equations of state that have been implemented for the computational simulation of porous powders, with the main difference between the two models being that one requires experimental data fits to be useful, whereas the other does not. This is an important point, because many materials lack relevant experimental data, and experiments give the best results when the dimensions and gage locations have been thoroughly examined beforehand. The models have been programmed into two hydrocodes. One hydrocode has been extensively verified, but has been deemed export controlled. The other hydrocode can be freely distributed, but has yet to be thoroughly verified.

The dynamic results showed first that the Mie-Grüneisen equation of state in the KO hydrocode works as well as in the CTH hydrocode. Second, that the P-α porous equation of state in the KO hydrocode predicted the Hugoniot state of well characterized solid Fe impacting well characterized porous Fe as well as in the CTH hydrocode.

Each hydrocode then showed how each EOS simulated the dynamic compaction of porous silica being impacted by PMMA. The dynamic compaction characteristics of porous silica powder were compared computationally against both experimental data from Cambridge University. The results indicate that the PMMA is well characterized by both hydrocodes implementing each model for all 15 experiments as expected. The results also show that the silica powder is not well analyzed using either hydrocode implementing either model to the experimental data at any initial powder density. Ultimately we do not know enough about the silica powder to accurately characterize the Hugoniots. However, KO does reproduce the CTH results accurately for the 0.77 and 0.1 g/cc powders for both the MG and *P-α* models. For the 0.25 g/cc silica powder, the *P-α* model adequately reproduces the CTH computational data, and the MG model remains unverified in KO. Therefore KO is verified against CTH for the prediction of Degussa Sipernat 50 μm porous silica powders at relatively low densities in the low shock velocity – particle velocity regime.

8. Future Research

On a computational level, the dynamic compaction of porous silica powder at porosities greater than 50 % has had limited success. The KO program has been able to reproduce the CTH data for the P-α model across all initial powder densities. This model has a distinct advantage in that prior knowledge of experimental data in unnecessary. However, this model was unable to accurately predict the experimental data provided by Cambridge University. As a starting point, fitting the experimental data to the P-α model can be pursued. Any successes found here can help iterate at the unknown values of this model for each silica density, i.e. P_s, P_e, α_e, α_p. This model may have to be amended in or for the silica powder to have proper agreement to the experimental data.

Prior attempts at modeling the dynamic compaction of porous silica can be seen in reference [10], using the P-λ model from Section 3.7. Since there is air that is still trapped in between the agglomerated matrix, this model can account for such a matrix. Furthermore, the static compaction results from this research showed no direct relation from static to dynamic compaction for characterizing porous silica. Possibly by trying a pore size calculation by BET or mercury porosimetry could yield such a relation, which would be a starting point for a new equation of state for dynamic compaction.

Another starting point for a new EOS is found from the fact that the silica powder in the static compaction experiment never exceeded a density of 0.7 g/cc. This is puzzling, because the solid density of sand is 2.2 g/cc. Sintering the silica wafers might bond the individual particles together to achieve the 2.2 g/cc wafers. These wafers may give rise to a new model which takes into account the heating that may take place in the dynamic compaction process.

9. References

---

[1] M. L. Wilkins, *Computer Simulation of Dynamic Phenomena*. Springer-Verlag Berlin Heidelberg ISBN 3-540-63070-8, 1999

[2] M. F. A'Hearn et al., "Deep Impact: Excavating Comet Tempel 1", Science Vo. 310 number 5746 October 2005.

[3] C. H. Van der Bogert, P. H Schultz, & J. G. Spray, "Impact-induced frictional melting in ordinary chondrites" Meteoritics & Planetary Science, Vol. 38, number 10, October 2003.

[4] D. S. Stewart et. al. "Simplifed of transition to detonation in porous energetic materials" Physics of Fluids Vol. 6 issue 7 July, 1994.

[5] K. A. Gothier, & V. Jogi, "Multiscale Shock Heating Analysis of a Granular Explosive" Journal of Applied Mechanics – Transactions of the ASME Vol. 72 issue 4, July 2005.

[6] M. Meyers, D*ynamic behavior of materials*. Wiley Press, 1994.

[7] R. F. Trunin, G. V. Simakov, & M. A. Podurets, "Compression of porous quartz by strong shock waves" IZv. Acad. Sci. USSR Phys. Solid Earth (English Translation) No. 2 33-39, 1971.

[8] Y.B. Zeldovich, & Y.P. Raizer *Physics of Shock Waves and High-Temperature Hydrodynamic Phenomena*., Academic Press, New York, 1966.

[9] R. F. Trunin, *Shock compression of condensed materials*. Cambridge Press, ISBN 0-0521-58290-3, 1998.

[10] J. P. Borg et al., "Dynamic Compaction of Porous Silica Powder" J. Appl. Phys. Vol. 98 issue 7 October 2005.

[11] W. Herrmann, "Constitutive Equation for the Dynamic Compaction of Ductile Porous Materials" J. Appl. Phys. Vol. 40 number 6, May 1969.

[12] B. M. Butcher & C. H. Karnes. Sandia Labs Res. Rep. SC-RR-67-3040 April 1968.

[13] D. K. Dijken & J. Th. M. De Hosson, "Shock Wave Velocity and Shock Pressure for Low Density Powers: A Novel Approach" J. Appl. Phys. Lett. Vol. 75 number 7, February 1994.

[14] G. A. Simons & H. H. Legner, "An Analytic Model for the Shock Hugoniot in Porous Materials" J. Appl. Phys. Vol. 53 number 2, February 1982.

[15] K. H. Oh & P. A. Persson, "Equation of State for Extrapolation of High-Pressure Shock Hugoniot Data" J. Appl. Phys. Vol. 65 number 10, May 1989.

[16] Q. Wu & F. Jing, "Thermodynamic Equation State and Application to Hugoniot Predictions for Porous Materials" J. Appl. Phys. Vol. 80 number 8, October 1996.

[17] M. M. Carroll & A. C. Holt, "Static and Dynamic Relations for Ductile Porous Materials" J. Appl. Phys. Vol. 43, number 4, April 1972.

[18] J. S. Dugdale & D. K. C. Mac Donald, "Thermal Expansion of Solids" Phys. Rev. Vol. 89 number 4, February 1953

[19] L. Boshoff-Mostert & H. J. Viljoen, "Comparative Study of Analytical Methods for Hugoniot Curves of Porous Materials" J. Appl. Phys. Vol. 86 number 3, August 1999.

[20] V. G. Shchetinin, Combust., Explos. Shock Waves Vol. 64, 1991.

[21] J. C. Slater, *Introduction to Chemical Physics*. Mcgraw-Hill, New York, 1999

[22] Marsh, *LASL Shock Hugoniot Data*, University of California Press, ISBN 0-520-04007-4 (1980)

[23] A. D. Resnyansky, & N. K. Bourne, "Shock-Wave Compression of a Porous Material" J. Appl. Phys. Vol. 95 number 4, February 2004.

[24] D. E. Grady & N. A. Winfree, "A Computational Model for Polyurethane Foam" In: Staudhamer KP, Murr LE and Meyers MA., editors, *Fundamental Issues and Applications of Shock-Wave and High-Strain-Rate Phenomena.* Elservier-Science. 2001; 485-491.

[25] K. Wunnemann, G. S. Collins, & H. J. Melosh, "A Strain-Based Porosity Model for Use in Hydrocode Simulations of Impacts and Implications for Transient Crater Growth in Porous Targets", Icarus. Vol. 180, February 2006.

[26] D. Drucker, & W. Prager, "Soil mechanics and plastic analysis or limit design". Quarterly of applied mathematics volume 10, pages 157–165 1952.

[27] H. Chtourou, A. Gakwaya, & M. Guillot, "Modeling of the Metal Powder Compaction Process using the CAP Model. Part I. Experimental Material Chachterization and Validation" Int. J. Solids & Structures. Vol. 39 2002.

[28] J. Von Neumann, & R. D. Richtmeyer, "A method for the numerical calculation of hydrodynamic shocks" Journal of Applied Physics Vol. 21 March, 1950.

---

[29] M. L. Wilkins, “Use of Artificial viscosity in Multidimensional Fluid Dynamic Calculations” Journal of Computational Physics. Volume 36 issue 3, July 1980.

[30] E. S. Hertel Jr., & G. I. Kerley, “CTH EOS Package: Introductory Tutorial.” SAND98-9045 UC-705 Export Controlled Information, Sandia National Labs, Albuquerque, NM, April 1998.

[31] N. K. Bourne, & Z. Rosenberg, “On the Ringing Observed in Shock-Loaded Piezoresitive Stress Gauges” Meas. Sci. Technol. Vol. 8 1997.

[32] Z. Rosenberg, et al. “Calibration of Foil-like Manganin gage in Planar Shock Wave Experiments” J. Appl. Phys. Vol. 51, Issue 7. 1980.

[33] R. Menikoff, “Constitutive Model for PMMA at High Pressure” J. Appl. Phys, Vol. 96, issue 12, 2004.

[34] R. L. Bell et al., “CTH User’s Manual and Input Instructions, Version 4.0”, Sandia National Laboratories, Albuquerque, NM, 1998.

[35] J. P. Borg & A. N. Lloyd et al. “Dynamic Modeling Comparisons for Porous Silica Powder” 14th APS Topical Conference on Shock Compression of Condensed Matter, Baltimore, MD August, 2005.

[36] D. Yaziv, Z. Rosenberg, & Y. Partom, “Release Wave Calibration of Manganin Gauges” J. Appl. Phys. Vol. 51 , December 1980.